CHALMERS
UNIVERSITY OF TECHNOLOGY

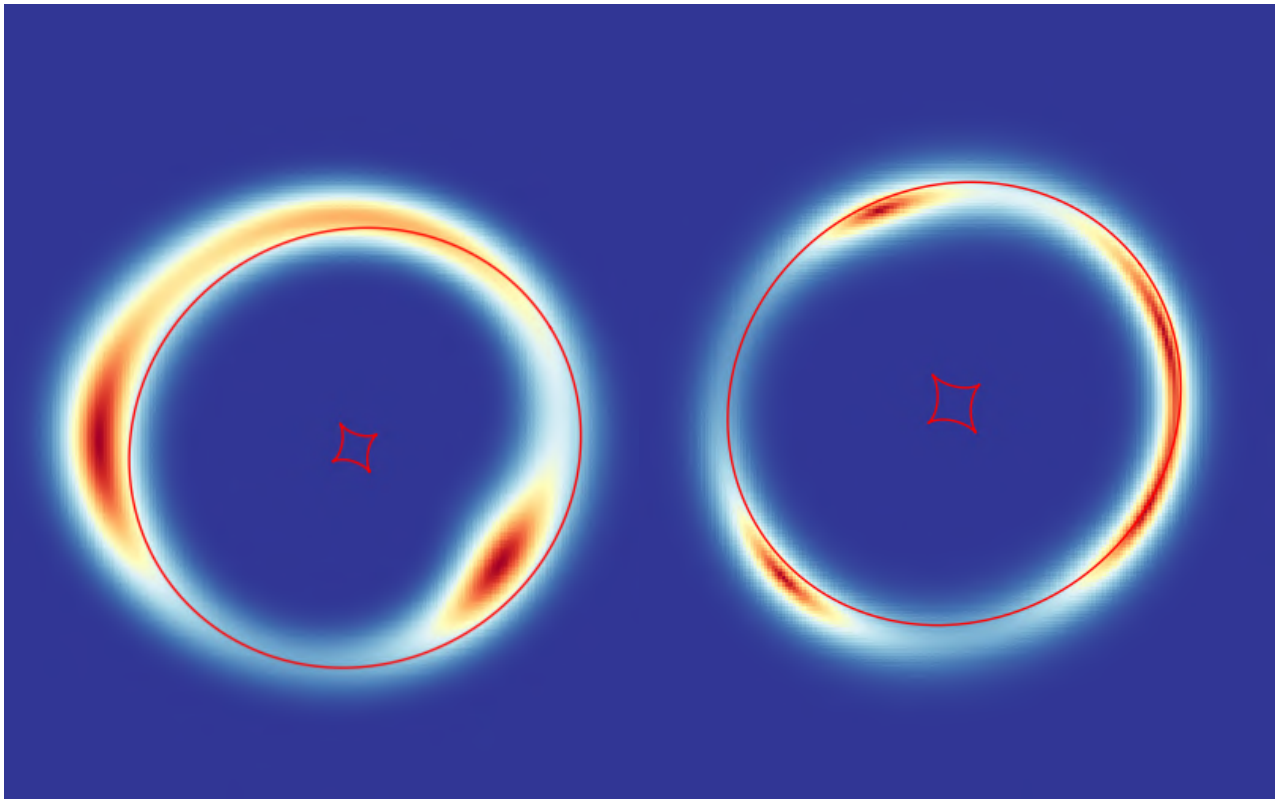

Gravitationally Lensed, High-Redshift Starburst Galaxies

and the CO(3-2) Transition for SPT0125-47 and SPT2134-50

Master's Thesis in Physics

MARKUS BREDBERG

DEPARTMENT OF SPACE, EARTH AND ENVIRONMENT

CHALMERS UNIVERSITY OF TECHNOLOGY
Gothenburg, Sweden 2022
www.chalmers.se

Master's thesis 2022

Gravitationally Lensed, High-Redshift Starburst Galaxies

and the CO(3-2) Transition for SPT0125-47 and SPT2134-50

MARKUS BREDBERG

CHALMERS
UNIVERSITY OF TECHNOLOGY

Department of Space, Earth and Environment
Division of Astronomy and Plasma Physics
Chalmers University of Technology
Gothenburg, Sweden 2022

Gravitationally Lensed, High-Redshift Starburst Galaxies
and the CO(3-2) Transition for SPT0125-47 and SPT2134-50
MARKUS BREDBERG

Supervisor:	Prof. Kirsten Kraiberg Knudsen, Department of Space, Earth and Environment
Co-supervisor:	Dr. Sabine König, Department of Space, Earth and Environment
Co-supervisor:	PhD student Kiana Kade
Examiner:	Assoc Prof. Magnus Thomasson, Department of Space, Earth and Environment

Master's Thesis 2022
Department of Space, Earth and Environment
Division of Astronomy and Plasma Physics
Chalmers University of Technology
SE-412 96 Gothenburg
Telephone +46 76 393 3085

Cover: High-resolution, image plane reconstructions of SPT0125-47 (left) and SPT2134-50 (right) produced by *Visilens*. Red areas show high intensity and blue areas low. Caustics are drawn in thin red lines.

Typeset in LaTeX
Printed by Chalmers Reproservice
Gothenburg, Sweden 2022

Gravitationally Lensed, High-Redshift Starburst Galaxies
and the CO(3-2) Transition for SPT0125-47 and SPT2134-50
MARKUS BREDBERG
Department of Space, Earth and Environment
Chalmers University of Technology

Abstract

Local, massive galaxies are seen to host very old stellar populations. This indicates that a significant fraction of the stellar mass was formed during early epochs. The discovery of intense starburst galaxies at high redshifts have suggested that such galaxies are part of an evolutionary sequence towards today's massive galaxies. This master's thesis provides an introductory theoretical background in the history and very basics of the study of galaxies, techniques and methods in observational radio astronomy, and evolution of distant, massive galaxies. After this summary, two redshift z=2.5-2.8 sources, discovered by the South Pole Telescope (SPT), are analysed through the visibility-based lens modeling tool `visilens`. Spectra and galaxy-galaxy gravitational lensing models are obtained from $\sim 0.1''$ resolution data from the Atacama Large Millimeter/submillimeter Array of the CO(3-2) line from SPT0125-47 and SPT2134-50. Results indicate magnifications of $\mu = 15.4 \pm 0.9$ for SPT0125-47 and $\mu = 20.2 \pm 2.9$ for SPT2134-50. The corresponding FWHMs are $(380 \pm 47)\,\mathrm{km\,s^{-1}}$ and $(550 \pm 87)\,\mathrm{km\,s^{-1}}$, which leads to intrinsic line luminosities $L'_{\mathrm{CO(3-2)}} = (5.1 \pm 0.84)10^{10}\,\mathrm{K\,km\,s^{-1}\,pc^2}$ and $L'_{\mathrm{CO(3-2)}} = (1.5 \pm 0.31)10^{10}\,\mathrm{K\,km\,s^{-1}\,pc^2}$, respectively. From previous derived relations, the gas masses are determined to $M_{\mathrm{gas}} = (3.4 \pm 1.1)10^{10}\,\mathrm{M_\odot}$ and $M_{\mathrm{gas}} = (1.6 \pm 0.49)10^{10}\,\mathrm{M_\odot}$ respectively. The molecular gas mass estimates are similar to dynamical estimates assuming rotation, which suggests that the inner region of these galaxies are gas-dominated. A skewed emission line and magnification for SPT0125-47 suggests that this source is either a rotating disc or a system of galaxy mergers.

Keywords: Galaxies: high-redshift — Gravitational lensing: strong — Techniques: interferometric — Telescopes: ALMA

Acknowledgements

It is with great appreciativeness that I hereby acknowledge the momentous help I have received throughout this thesis and the kind and skilful people behind it. My gratitude is firstly directed towards my supervisor Prof. Kirsten Kraiberg Knudsen for constantly feeding me ideas and inspiration, and supporting me in my work in every way I could ask for. I owe the project idea as well as much betterment to you.

Secondly, I would like to thank my two co-supervisors, Sabine König and Kiana Kade for diligently assisting me with the imaging and gravitational lensing, respectively. Sabine, in particular, endured and responded well to many of my silly and inexpert questions while introducing programs for calibration and imaging. Kiana repeatedly managed to help me with things that was beyond her expertise, dedicating much of her time and research skills for this aim. Without you my thesis would not have been.

As this thesis is the culmination of my five year long studies at Chalmers, I must praise the school for offering no shortage in interesting options, both for the purpose of education and everything circumambient. The most important components of this are my friends. I would like to include my twin brother Joakim in this thankfulness for reminding me of the approaching opportunities. Thank you all, whatever the future brings.

Markus Bredberg, Gothenburg, June 2022

We wish to pursue the truth no matter where it leads
— but to find the truth, we need imagination and skepticism both.
We will not be afraid to speculate,
but we will be careful to distinguish speculation from fact.
The cosmos is full beyond measure of elegant truths;
of exquisite interrelationships;
of the awesome machinery of nature.

CARL SAGAN

Contents

List of Abbreviations and Acronyms

Below is the list of acronyms that have been used throughout this thesis listed in nearly alphabetical order:

UV	Ultraviolet (100-300 nm)
NIR	Near-InfraRed (780-2000 nm)
MIR	Mid-InfraRed (2-15 µm)
FIR	Far-InfraRed (15-1000 µm)
AGN	Active Galactic Nucleus
ALMA	Atacama Large Millimeter/submillimeter Array
CASA	Common Astronomy Software Application
CMB	Cosmic Microwave Background
DSFG	Dusty Star-Forming Galaxy
FWHM	Full Width at Half Maximum
GMC	Giant Molecular Cloud
HPBW	Half Power Beam Width
IMF	Initial Mass Function
ISM	InterStellar Medium
LBG	Lyman Break Galaxy
PA	Position Angle
PWV	Precipitable Water Vapor
RMS	Root Mean Square (error)
SED	Spectral Energy Distribution
SFG	Star-Forming Galaxy
SFH	Star Formation History
SFE	Star Formation Efficiency
SFMS	Star Formation Main Sequence
SFR	Star Formation Rate
sSFR	specific Star Formation Rate
SMBH	SuperMassive Black Hole
SNR	Signal-to-Noise Ratio
SPT	South Pole Telescope
VLBI	Very Long Baseline Interferometry

Nomenclature

Below is the nomenclature of constants, parameters and observables that have been used throughout this thesis.

Constants

c	Speed of light
G	Newton's gravitational constant
$k_{\rm B}$	Boltzmann's constant
h	Planck's constant

Variables

ν	Frequency
λ	Wavelength
z	Redshift
E	Energy
W, K, U, $E_{\rm M}$	Gravitational, kinetic, internal and magnetic energy
P, P_ν	Power, power density
I, I_ν	Intensity, specific intensity
S, S_ν	Flux, flux density
T	Temperature
$T_{\rm b}$, $T_{\rm a}$, $T_{\rm d}$	Brightness, antenna, and dust temperature
L	Luminosity
$L_{\rm line}$, $L'_{\rm line}$	Line luminosity in $L_\odot$ and K km s^{-1} pc^2
m, M	Mass of a small region and large body respectively
ρ, Σ	Volume and surface mass density
μ	Magnification from gravitational lensing
r, R	Distance and radius
v, σ_v	Velocity and velocity dispersion
A	Area
Ω	Solid angle

e	Ellipticity
a, b	Major and minor axis
θ_{E}, α_{red}	Einstein angle and reduced deflection angle
D_{ij}, D_L	Angular diameter distance and luminosity distance
Z	Metallicity
J	Rotational level
$\Phi(L)\mathrm{d}L$	Number density of galaxies with luminosity between L and $L + \mathrm{d}L$
f_{gas}	Gas mass fraction
t_{ff}, t_{dep}	Free fall and depletion time scale

List of Figures

List of Tables

1
Introduction

If the history of the Universe was printed on a timeline stretching from the Moon to Earth, the first humans would appear around the tip of Mount Everest, the oldest astronomical records would soar some 150 meters above ground, and the introduction of galaxies would be within reach of a resilient jump. Today, with better and better telescopes, a increasingly clear view of this timeline is at our fingertips. Exciting times are ahead!

Galaxies are the astronomical cells of the Universe. Their evolution is a complex interplay with their surrounding. In simplicity, this is modelled as the baryon cycle. Outside gas is accreted, cooled and converted into stars. Inside gas is heated and ejected from supernovae and jets in the active galactic nuclei phase of the central supermassive black hole. But the Universe is vast and complex. No galaxy is identical. This thesis is an attempt at studying this complexity.

1.1 A Very Brief History of Galaxies in the Universe

Looking up at the night sky is enough of an explanation as to why astronomy is the oldest science on Earth. Mesopotamian records date 5000 years back. Yet, any stargazer in any era knows how much left there is to discover.

Grouping stars together in constellation has kept humans busy since the end of the Paleolithic Era. An early proposition of the nature of our galaxy was made by pre-Socratic philosopher Democritus, saying that the bright band on the night sky (see Figure 1.1) could consist of many distant stars (Plutarch, 2006). This was proven first when Galileo Galilei pointed his telescope to this band in 1610 (Galilei, 1610).

Our closest neighbouring galaxy, Andromeda, is actually several times the angular size of the moon. Therefore records of its detections date back to Persian astronomer Al-Sufi in the 10th century, describing it as a 'small cloud'. Ferdinand Magellan thought likewise when he, on a circumnavigation of the globe, found the Large and Small Megallanic clouds.

New horizons opened up when, Christiaan Huygens in the mid-seventeenth century used the recently invented telescope to find new, fuzzy and diffuse systems on the sky (as described in Cimatti et al., 2019). Due to this appearance, they were named nebulae after the Latin word for mist. Naturally, speculations on what these

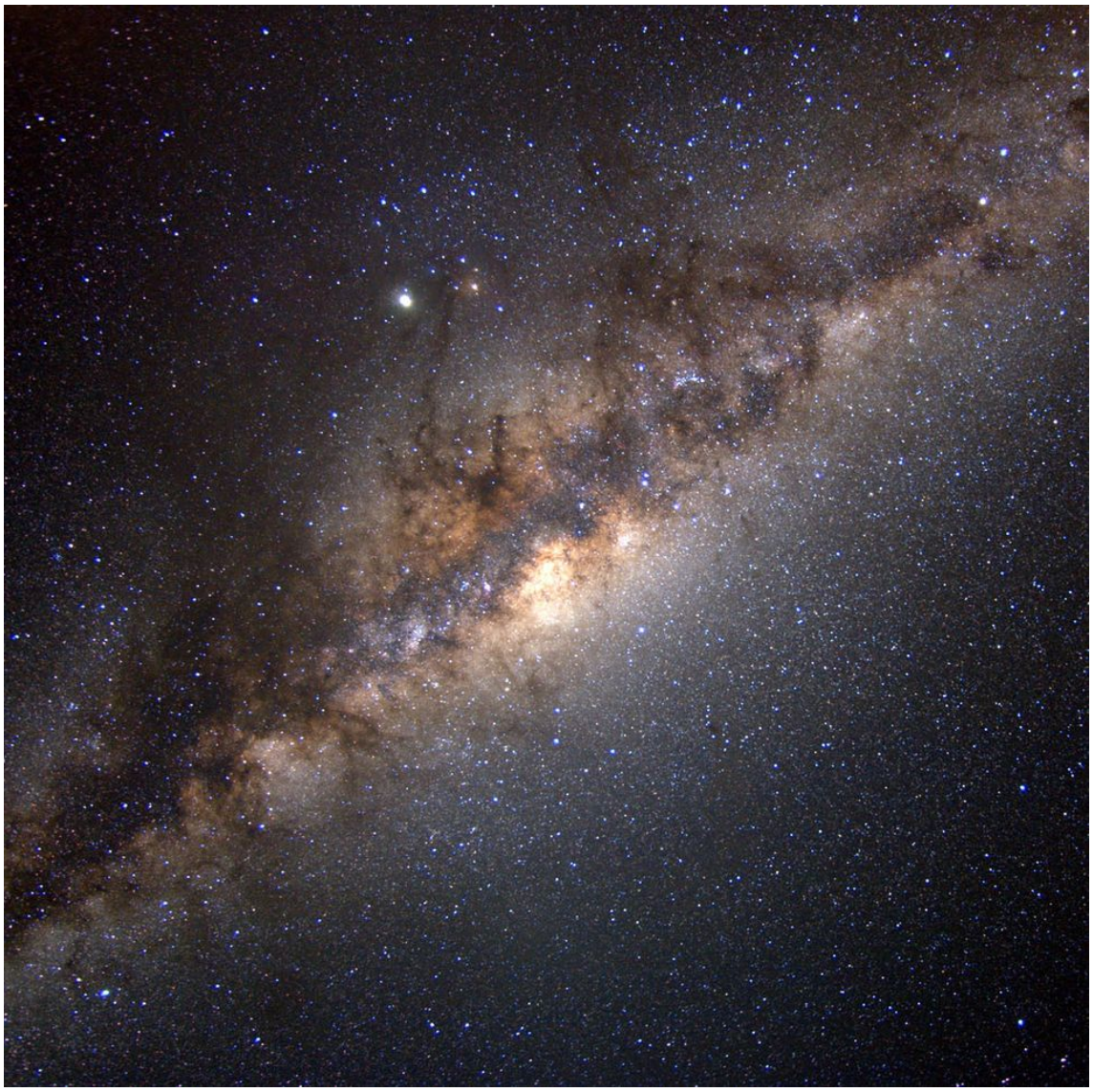

Figure 1.1: The bright, dusty band on the the night sky is actually the center of our Galaxy. Credit: NASA.

nebulae were followed. In 1750, Thomas Wright likened them with our Galaxy[1], suggesting that they were distant, flat, rotating layers of stars, held together by gravity. This idea of 'island universes' was expanded by philosopher Immanuel Kant, in his 1755 treatise.

As these mysterious objects accumulated in numbers in the second half of the 18th century, Charles Messier compiled a 109 objects long catalogue of what would later be called Messier objects. Some of these objects were galaxies, like Andromeda, M31, but others had a different nature, like the Orion Nebula M42. In 1888, John Louis Emil Dreyer created a new, extended catalogue, titled the new general catalogue (NGC) (Dreyer, 1888). Despite these attempts, no universal method of naming astronomical sources exists as of today.

[1]I write capital-G Galaxy when referring to the Milky Way.

Improved telescopes meant improved resolutions which resulted in the identification of spiral structures in some of these nebulae. In the so called 'Great Debate' between Harlow Shapley and Heber Curtis (see e.g. Smith, 1982), spectroscopic observations concluded that what is now known as the Andromeda galaxy is located outside our Galaxy. As a result, like so many times before in human history, the estimated size of the Universe[2] grew by several orders of magnitude. Current estimates predicts the existence of more than a hundred billion galaxies in our observable Universe. The term 'galaxy' is Greek for 'milk' adducing to the 'milky' appearance of our galaxy, the Milky Way. The original term 'nebula' is now used exclusively for other fuzzy systems, namely clouds of dust and gas within a galaxy.

The discovery that solved the 'Great Debate' led to one of the most important discoveries of our Universe. Edwin Hubble famously used pulsating, giant stars, Cepheids, as 'standard candles' to compare their observed luminosity with their intrinsic luminosity, given their flux period. In the late 1920s, Hubble and had measured enough sources to derive a law stating the expansion of the Universe. Independent of Hubble, Georges Lemaître theorised and proposed the same law. With this now-called Hubble-Lemaître law[3] history can be run backwards, leading to the Big Bang.

1.2 A Cosmological Timeline

Following Hubble and Lemaître's discovery, cosmology was introduced as the study of the evolution of the Universe. Modern cosmology accounts most importantly for the Hubble-Lemaître law, together with the cosmic microwave background (CMB) radiation discovered by Penzias and Wilson in 1964.

Modern observations of the CMB, distant objects, and gravitational waves has corroborated that the Universe abides by the cosmological principle, being large scale homogenous and isotropic, and that it appears flat.[4] In order to explain this, the theory of inflation was introduced by Starobinsky, Guth and Linde in the late 1970s.[5] The inflation was a short period of exponential acceleration of expansion that preceded the creation of matter and light.

The characteristic anisotropy scales of the CMB was matched to cosmological parameters, motivating the Lambda cold dark matter (ΛCDM). Due to its common usage, this is also known as the cosmological standard model. In it, the Universe is thought to be dominated by 68.5 % dark energy and 26.6 % cold dark matter, leaving only 4.9 % left for baryonic matter, that is the particles that we know of (McCarthy and Seidelmann, 2018; Planck Collaboration and Ade, 2016). In this cosmological standard model the 28.5 Gpc diameter of the Universe corresponds to an age of 13.8 Gyr (Bars and Terning, 2009).

Depending on the values of the cosmological parameters matter distributes and evolves differently. In general, the evolution of the Universe is governed by the

[2] Akin to Galaxy, capital-U Universe refers, in this thesis, to our observable Universe.
[3] Before 2018 this was officially called the Hubble law.
[4] "Flat" means that Euclidean geometry is applicable. It should be clarified that the flatness itself is not confirmed, but the appearance of it is consistent with measurements.
[5] Inflation also explains the scarcity of magnetic monopoles.

parameters of physics that can be extracted from studying the very early Universe. With time the Universe expanded and got colder creating different epochs in which particles and physical laws decoupled or formed. Current physics cannot explain anything during the Planck Epoch 10^{-43} s after the Big Bang, but after the first minutes atomic nuclei had formed in the Big Bang-nucleosynthesis. Similar combinations had preceded for quarks and leptons, including their antiparticles, while neutrinos had decoupled from other particles and the electromagnetic, weak, and strong interactions had become distinct forces (McCarthy and Seidelmann, 2018).

380 kyr after the Big Bang, in the epoch of recombination, the Universe grew to be sufficiently large for the temperature to decrease enough for electrons to combine[6] with nuclei. In this process, that is called the photon decoupling, photons with longer mean free path were released. Due to the continuing expansion of the Universe, the wavelengths of the CMB are stretched, or redshifted, $z + 1 \approx 1100$ times. Due to intense Thomson scattering making the younger Universe opaque, astronomers can detect photons travelling with the finite speed of light to see back in time, but only back to this epoch.

The recombination was followed by the cosmological dark ages. Hydrogen, helium and lithium together with dark matter filled the Universe, but not with light. The ΛCDM model suggests that primordial fluctuations caused dark matter density irregularities in the so-called large scale structure, that initiated accretion and merging between baryonic matter. Studying these early causes for gravitational attraction could disclose new insights in not just cosmology, but also particle physics.

One very important piece of the puzzle on early galaxy formation is the nature of dark matter halos. If CDM regions are dense enough, gravity can outcompete the expansion of the Universe (locally). However, for gravitational contraction to continue the internal pressure must not start to dominate. Baryonic gas avoids this through i.a. the free-free photon emission of Bremsstrahlung. Dark matter, on the other hand, are observed through gravitational lensing and rotation curves of galaxies to not form denser regions. It it therefore presumed that dark matter does not interact via the strong or the weak nuclear force; there are no evidence for 'atomic behaviour', or the electromagnetic force; it does not produce photons. So, dark matter only interacts via gravity.

The birth of stars and galaxies marked the beginning of the epoch of reionisation. That photon emission reionised hydrogen in the intergalactic medium, IGM, around $z \sim 6$ is motivated by Gunn-Peterson troughs - the absence of flux for Lyman-alpha and -beta lines that characterise neutral hydrogen (Gunn and Peterson, 1965; Fan et al., 2006). The general explanation is that as the first stars, also known as population III stars, began to emit UV-photons, nearby hydrogen was ionized, creating spheres of ionised medium. Other high energy photon sources, such as black hole accretion disks, stood for 30 % of this ionisation (Gnedin and Ostriker, 1997; Lu et al., 1998). This process began with the very first stars forming around $z \sim 30$ and had produced a completely ionised Universe at $z \sim 7$ (Barkana and Loeb, 2001; Wise et al., 2012).

Population III stars formed from gravitational contraction of the hydrogen, he-

[6]Since this was the origin of neutral atoms, a more correct name of the epoch would be 'epoch of combination'.

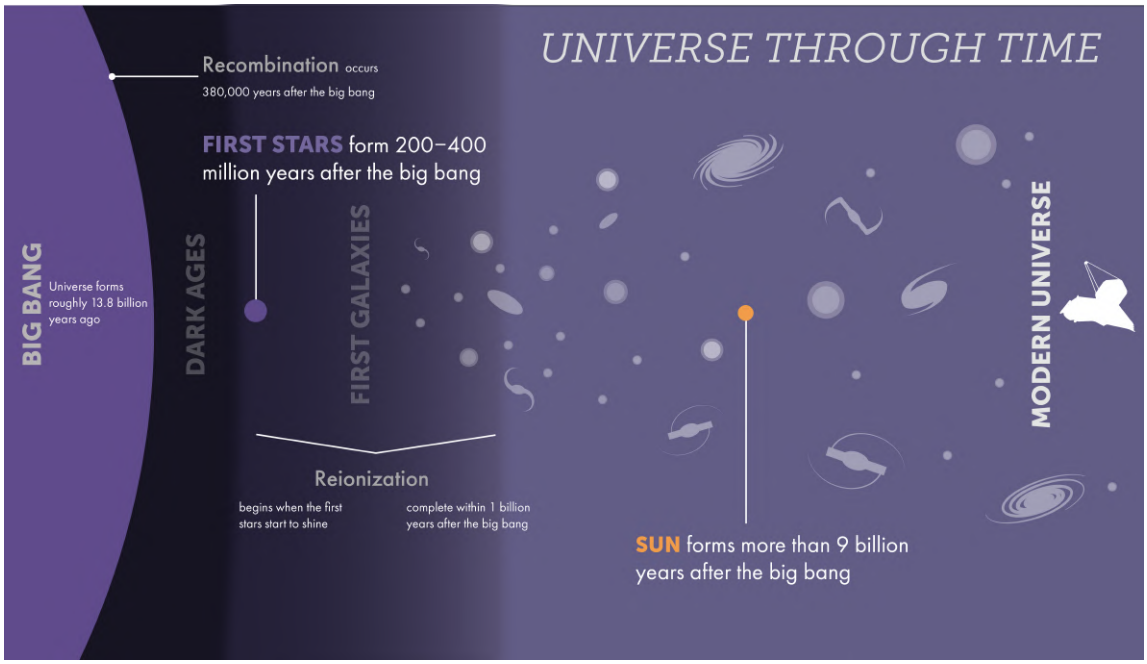

Figure 1.2: A schematic timeline of the Universe. The shades of the background represents the ionisation level. In white is the *James Webb Space Telescope*. Credit: STScI.

lium (and lithium) that was produced in the Big Bang nucleosynthesis. Metal-free star formation in the early Universe is theoretically different from the chemically enriched star formation in the local Universe. For instance, since H_2 forms on dust particles and is responsible for most of the cooling below $T \sim 10^4\,\mathrm{K}$, population III stars could only form in large clouds, becomming very massive (Schneider, 2006, subsection 10.3.1). One characteristic of these rare stars is that they are very massive. This means they have a typical lifetime of less than 10 Myr (Schaerer, 2003). Thus, in early galaxies, violent supernova explosions ousted out the remaining gas within the dark matter halo, reducing the chance for new stars to form within the same dark matter halo. Only at $z \sim 10$, when these dark matter halos had grown a hundred times to $10^8\,\mathrm{M}_\odot$, could enough gas withstand the supernova winds so that star formation could continue (Cimatti et al., 2019, section 9.6). Therefore, the population III star formation was roughly constant during the epoch of reionisation (Crosby et al., 2013).

In the last 13 Gyr there has been no fundamental change of the structure of the Universe. Figure 1.2 outlines the aforementioned points in the history of the Universe on a non-linear axis. After the still expanding Universe became fully ionised, as indicated by the light purple background to the right in the figure, new stars and galaxies continued to form, while the already existing galaxies continued to evolve. The large mass of a population III star causes its supernova to most likely result in a large black hole remnant. Possibly, these could accrete and grow to the supermassive black holes that local galaxies are observed to have (Dokuchaev et al., 2007).

Some 4.6 Gyr ago, the Sun formed, and with it, our solar system. On Earth,

humans have, in the last century, begun exploring extragalactic astronomy. This is done by computationally heavy hydrodynamic simulations, simplifying semi-analytic approaches or direct observations that produce faint and unresolved images of distant galaxies. For the benefit of combating the various challenges, these methods complement each other. Semi-analytic approaches are, for instance, better than simulations at studying global properties. Direct observations of some galaxies at distinct distances can be viewed as snapshots at different times. This thesis will focus on the observational approach.

1.3 Through the Telescope

Observing is detecting photons in different wavelengths. When an eye sees an object it measures the brightness and colour in different places in its environment. Likewise, when a telescope observes a source, it measures the intensity and wavelength on different locations on the sky. With some knowledge about the source and the path of photon propagation, additional information can be obtained.

The (spectral) intensity is the energy that is observed by the telescope (at a given wavelength). Our three dimensional space disperse photons on a two dimensional surface given some distance from the source. This inverse square dependence is the reason why, for example, standard candles (sources with known luminosity) are great measuring sticks for distance. Gas, dust and gravitational lensing can complicate this relation.

Interpretation of the measured intensity requires an understanding of the microscopic processes that constitute it. For instance, hot gas in accretion disks surrounding black holes generates ultraviolet (UV) and X-ray emission. Stars emit lights mostly in the UV—optical—infrared (IR) due to internal heating from fusion reactions in the stellar core. Mid-IR (MIR) and far-IR (FIR) raditation is dominated by the emission from interstellar dust.. When studying star formation it is crucial to note that only molecular gas is dense enough to form stars. Collisional excitations produce vibrational and rotational spectral lines in the IR to mm region, where starlight does not dominate. At low temperatures CO, the second most abundant molecule after H_2, dominates the molecular radiation (see e.g. Schneider, 2006; Cimatti et al., 2019).

Due to quantum mechanical restrictions, only certain excited states are allowed for the molecules. Transitions between such states produce emission at characteristic wavelengths. As CO is the second most abundant molecule and easy to observe, the rotational transition CO(J = 1-0) emission line can be used as a means for estimating the total molecular gas mass. Since different states have a relative population density as a function of temperature, the J-ladder, or spectral line energy distribution, is a great tool for estimating temperatures and obtaining i.a. column densities of molecular hydrogen (e.g Carilli and Walter, 2013; Cimatti et al., 2019).

The general appearance of a galaxy spectrum can also reveal some properties. Starburst galaxies, for instance, are undergoing an episode with elevated star formation rate. Due to expulsion of gas, from large supernova explosion, outside an inner disk of massive stars, and galaxy-galaxy interaction (sometimes as a fuse for rapid star formation), their morphological appearance can therefore be irregular.

Spectrally, they show strong emission lines and emit more in shorter wavelengths, due to the presence of high-mass stars (e.g. Sparke and Gallagher, 2007).

For ground-based telescopes the photons propagate through the molecularly filled atmosphere of the Earth. Only a few spectral ranges can pass through, these being in the optical, NIR and radio, but even for these, atmospheric attenuation often motivate a high altitude site. The 4200 m summit of Mauna Kea in Hawaii has therefore been a popular site for optical telescopes. The 10 m Keck 1 and Keck 2 telescopes and the 8.2 m Subaru Telescope are two examples (Schneider, 2006, section 1.3). At 2800 m altitude on the Antarctic Plateau, the South Pole Telescope (SPT) uses its 10 m parabola primarily to study the extragalactic Universe and the CMB through microwave and millimeter wave observations. The SPT0125-47 and SPT2147-50 galaxies that are studied in this thesis were discovered with the SPT.

Observations in other wavelengths are limited to space telescopes. Here, telescopes such as *Chandra X-ray Observatory* (X-ray), *Galaxy Evolution Explorer* (UV), *Hubble Space Telescope* (optical/NIR), *Spitzer Space Telescope* (MIR), and *Herschel Space Observatory* (FIR) have been the leading contributors to research in galaxy evolution (Cimatti et al., 2019). The new *James Webb Space Telescope* (IR) is the largest (6.6 m) space telescope today and with good IR imaging and spectroscopic capabilities it will enable us to study the epoch of reionisation among other topics (Gardner et al., 2006).

The resolution of a source depends on the instrument, the atmosphere, and the ratio of the wavelength to the observing diameter. Ground-based telescopes that view longer wavelengths, such as microwaves or radio waves, need very large observing diameters to resolve distant objects. This is obtained by connecting an array of telescopes in what is known as interferometry. By knowing the position, size and sensitivity of each antenna, a composite image can be produced through cross-correlation calculations.

The first interferometric measurements where done in the 1960s (Schneider, 2006, section 1.3.1). The Very Large Array[7] was introduce in the following decade covering frequencies between 1 and 50 GHz and baselines up to 36 km (National Radio Astronomy Observatory, 2012), leading to breakthroughs in the study of active galactic nuclei (AGNs). Atacama Large Millimeter/submillimeter Array (ALMA) has for the past decade been the leading interferometer for wavelengths around 0.3-3 mm. Data from ALMA will be used in this thesis.

Connecting telescopes across multiple observatories is known as very long baseline interferometry (VLBI). This is how the Event Horizon Telescope resolved the supermassive black hole (SMBH) of M87 in 2019 (Event Horizon Telescope Collaboration and Akiyama, 2019).

1.4 This Thesis

This master's thesis aims to improve the understanding of star formation and galaxy evolution in the early Universe. Research on galaxy evolution is primarily compli-

[7]This was 2012 renamed Karl G. Jansky Very Large Array after a major upgrade of i.a. the receivers.

cated by selection biases. To observe high-redshift galaxies, particular lines, sprectral breaks or frequency regions are adapted. On top of this mostly unobscured and luminous or magnified sources are visible. This causes very biased samples of galaxies from a Universe that is smaller, denser, warmer and different than today. Knowledge of galaxy evolution is therefore dependent on fitting models to the observables. Good models should be able to explain the observed (scaling) relations, e.g. the Schmidt-Kennicutt and Tully-Fisher relations. As is the case for most master's theses, a summary of relevant theory will introduce the subject. This introductory part continues into Chapter 3, which discusses how measurements of high-redshift galaxies are done. Chapter 2 presents the obtained information on galaxy evolution. Next, data from ALMA on the sources SPT2134-50 and SPT0125-47 is imaged, modelled through gravitational lensing, and presented in a more typically scientific manner of method (Chapter 4), results (Chapter 5), discussion (Chapter 6), and conclusion (Chapter 7).

2

Evolution of High-Redshift Galaxies

A galaxy is the modern term of what was originally called an island Universe (Shapley and Curtis, 1921). Since the 'Great Debate', the definition has particularised somewhat to a gravitationally bound system of gas, dust, stellar objects and dark matter (Sparke and Gallagher, 2007). A more specific definition would not incorporate the vast differences in size, shape and content that have been observed. Masses of galaxies range from $\sim 10^5\,\mathrm{M}_\odot$, for the smallest known galaxy Segue 2 (Kirby et al., 2013), to $\sim 10^{14}\,\mathrm{M}_\odot$, for the largest known galaxy IC 1101 (Fisher et al., 1995). The smallest galaxies are called *dwarf galaxies* and can measure down to $10^2\,\mathrm{pc}$ while the largest stretch $10^6\,\mathrm{pc}$ (e.g. Schneider, 2006; Sparke and Gallagher, 2007).

Since mass density varies depending on morphology and content, the size of a galaxy does not determine its mass. Instead, the Sloan Digital Sky Survey has shown that the size distribution, at a given luminosity and galaxy type, follow a log-normal function characterized by its median radius and velocity dispersion (Shen et al., 2003). For individual galaxies, the Tully-Fisher relation (Tully and Fisher, 1977) connects the luminosity with the maximum rotational velocity for spiral galaxies, and the Faber-Jackson relation (Faber and Jackson, 1976) describes a similar relation between luminosity and velocity dispersion for elliptical galaxies. Generally, a galaxy with high luminosity has an increased likelihood of being massive, radially large, red, having centralised luminosity, high metallicity and a clearer break in the spectrum near 4000 Å (Schneider, 2006, page 142). The number of galaxies per Mpc^3 with luminosity between L and $L+\mathrm{d}L$ was described by Schechter (1976) as the *Schechter function*

$$\Phi(L)\mathrm{d}L = \Phi^* \left(\frac{L}{L^*}\right)^{\alpha} \exp\left(-\frac{L}{L^*}\right)\mathrm{d}\frac{L}{L^*}. \tag{2.1}$$

Following up on the science of observations from the previous chapter, this chapter will summarise the resulting theory of the sources themselves. For this thesis, the relevant sources are high-redshift ($1 < z < 3$) galaxies. Section 2.1 introduces the most important ways of categorisation. Section 2.2 and 2.3.1 presents the formation of stars and galaxies. The latter subsection is part of the general topic of galaxy evolution of Section 2.3. This section, continues with unfolding some popular models and relations of how star formation, principally, regulates the evolution of galaxies.

2.1 Types of Galaxies

The diverge population of galaxies in the Universe complicates classification. Still, it has been useful to isolate qualities, such as morphology, colour, spectral appearance, and content of a galaxy and classify accordingly. Types of classification depend on the type of observation. Nevertheless, due to gravitational interactions and continuous evolution, many galaxies fit poorly within the given categories.

2.1.1 Hubble Classification

Historically, optical telescopes motivated classification according to shape. As soon as a large enough quantity of galaxies had been observed, Hubble presented his morphological classification. The corresponding tuning-fork diagram is called the *Hubble sequence* and consists of, from the left, *ellipticals* and (normal and barred) *spirals*. Because of this arrangement, galaxies to the left (right) are often called *early* (*late*) type galaxies despite no evolutionary motivation for this. Elliptical galaxies have only elliptical brightness contours as their only clearly defined structure. Consequently, the stars within have largely random motion. Ellipticals are specified with the letter 'b' ('d') for a boxy (disky) appearance and a number $n = 10\epsilon$, where $\epsilon = 1 - b/a$ describes the ellipticity of an ellipse with semi-major (-minor) axis a (b). Spiral galaxies have higher gas-to-stellar mass ratio than ellipticals. They are disk-shaped, and specified by a 'B' if barred, and a letter from 'a' to 'c'[1] to denote the relative brightness between the central bulge and the disk. Sometimes how tightly wrapped around the bulge the spiral arms are is included in the classification too. In the intersection of the three arms, *lenticular galaxies* mark the intermediate state between ellipticals and spirals. While the Hubble sequence can describe most bright galaxies, it is often complimented with *irregular galaxies* (sometimes called *peculiar galaxies*) that lack regular structure. Other structural changes are sometimes proposed to easier fit intermediate states (see e.g. Graham, 2019). Morphological classification is slow manual work for large sky surveys, but involvement of the public has made it feasible to continue (see *Galaxy Zoo* and Lintott et al., 2008).

2.1.2 Colour Bimodality and the Star-Forming Main Sequence

To combat the problem of projection effects, the optical light being redshifted out of the optical window and the difficulty of doing morphological classification at increased distance, and inapplicability for a large amount of galaxies, a bimodal colour distribution can be used instead. Since the apparent magnitude in any region of the electromagnetic spectrum follow the same distance dependence, the apparent magnitude difference in two wavelength bands, also called the *colour excess*, between two sources is distance independent. By plotting the number count as a function of colour excess, for any absolute magnitude, it was discovered that galaxies tend

[1] Combinations of letters indicate transitional states, and sometimes the scale is extended to the letter 'd'.

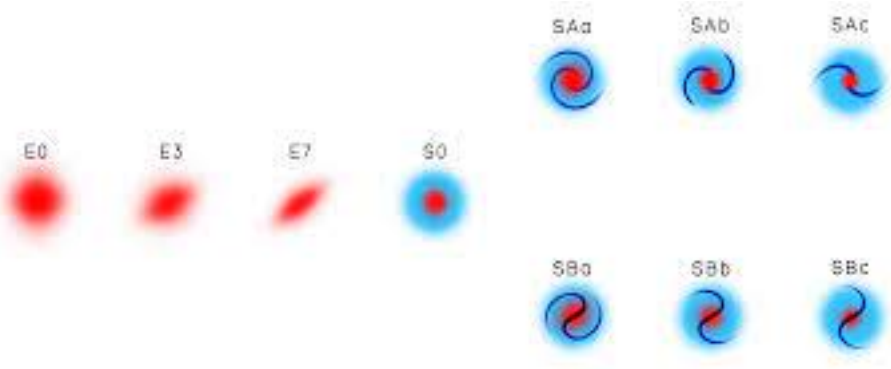

Figure 2.1: The Hubble sequence. Credit: (Graham, 2019).

to be either luminous and *red* or faint and *blue* (Baldry et al., 2004a,b). In fact, the distribution is well fitted by two Gaussian functions. Moreover, the types are separated by the characteristic stellar mass $M_\star \sim (2-3)10^{10}\,\mathrm{M}_\odot$ with red galaxies dominating the population that has a larger stellar mass than this. Red galaxies also have a larger mass-to-light ratio M/L.

In the last two decades the color bimodality has been coupled to the idea that, like stars, galaxies exist on a main sequence (Strateva et al., 2001). In this case, the axis of abscissas specify stellar mass and the axis of ordinates show the star forming rate, see Figure 2.2. The main sequence of star-formation galaxies, also called *star formation main sequence* (SFMS), form a slope. Above this slope, *starburst galaxies* can be found and below the *green valley* and the region of red and quenched galaxies are (Cano-Díaz et al., 2016, CALIFA survey). The green valley is less galaxy dense. Interestingly, it is where the Milky Way and Andromeda lie (Mutch et al., 2011). One common interpretation (see e.g. Mancuso et al., 2016; Sherman et al., 2021) is that galaxies form as star-forming galaxies to the left of the SFMS. When the stellar mass has grown, the galaxy enters the SFMS where it slowly moves up along the sequence. Eventually, either gas exhaustion slows down star formation so that the galaxy slowly moves into the green valley, or an AGN rapidly quenches the galaxy, transforming it into an early-type galaxy in the bottom region of the diagram. Indeed, the low gas-to-stellar mass for ellipticals is a reason for lower star formation and redder light.

Zooming in on the spectrum, and observing spectral lines instead of colour, different galaxy types again appear different. Connecting to the Hubble sequence, it is seen that early types have weaker emission lines, stronger absorption lines and a 'break' near 4000 Å (Kennicutt, 1992). This spectral break is the dominant feature for populations without a large star formation. Combining this dependence with the fact that the break is insensitive to metal abundance makes it a good tool for studying galaxy evolution over time (Dressler and Shectman, 1987). In the next section, it will be presented how spectral breaks produce colour selections that can locate galaxies at high redshift and name their types. Some examples of these are Lyman-break galaxies (LBGs), BzK galaxies, distant red galaxies (DRGs) and extremely red objects (EROs). More details on probing galaxies and their gas will be presented in Section 3.4.2.

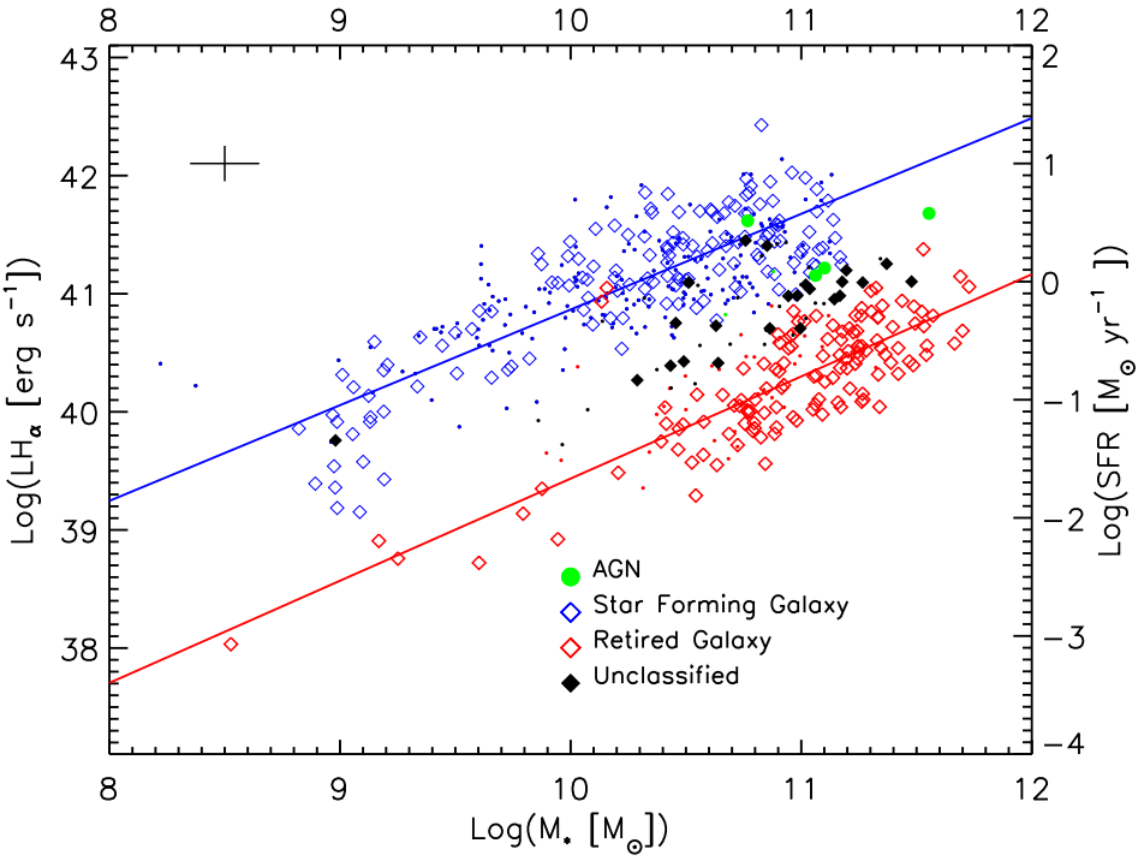

Figure 2.2: Main sequence for star-forming galaxies and the region for red and inactive galaxies, with data from the CALIFA survey. Green circles mark sources where AGN emission dominates the ionisation emission. Remaining colours are defined by their Hα equivalent width (>6 Å for blue, <3 Å for red, and black in between). The fitted lines are for galaxies with inclination $< 60°$. These are rhombus shaped in the diagram. Credit: (Cano-Díaz et al., 2016, Figure 1).

2.1.3 Starburst Galaxies

Starburst galaxies produce several hundred solar masses of stars per year. This can be compared with the $\sim 3\,\mathrm{M}_\odot\,\mathrm{yr}^{-1}$ for the Milky Way (e.g. Schneider, 2006). Starbursts are better thought of as galaxies in a phase of high star-formation than as a different type of galaxy (Karl et al., 2010; Heckman, 2000). Dusty, star-forming galaxies (DSFGs) can, if the star formation is high enough, be very luminous in the FIR. This is because the dust absorbs starlight and re-emits in FIR. The tens of thousands of galaxies discovered by a ten month long survey by the Infrared Astronomical Satellite (IRAS) in 1983 did therefore receive the name IRAS galaxies or, if $L > 10^{11}\,\mathrm{L}_\odot$, luminous infrared galaxies (LIRGs) (Soifer et al., 1984; Chester, 1988). Galaxies that are even more luminous in IR are called ultra luminous infrared galaxies (ULIRGs) if $L > 10^{12}\,\mathrm{L}_\odot$, hyper luminous infrared galaxies if $L > 10^{13}\,\mathrm{L}_\odot$ and extremely luminous infrared galaxies if $L > 10^{14}\,\mathrm{L}_\odot$.

One possible cause for periods of high star-formation is strong gravitational interaction with another galaxy. Such interactions can compress gas to form stars,

which can explode as supernovae and consequently compress even more gas, starting chain events of star formation (Sanders, 1997; Hopkins et al., 2006). If this interaction ends in a galaxy collision, the event is called a *galaxy merger*. Galaxy mergers are divided into *wet* (gas-rich) and *dry* (gas-poor) merges. They can also be divided into *major mergers*, which have a small mass ratio ($\lesssim 4:1$) and *minor mergers*, which have a large mass ratio of $4:1 \lesssim R \lesssim 10:1$. Major mergers has involved one third of all massive galaxies, while minor mergers has included the remaining galaxies. The motion of stars can be disorder by major mergers, which can create large random velocities of the stars, possibly transforming a disk galaxy into an elliptical. Additionally, local compressions of gas can spark a period of rapid star formation which exhausts the gas, as seen in for instance the Antennae galaxy. Minor mergers only result in the smaller galaxy being absorbed by the larger, like the dwarf galaxy Sagittarius is currently being disintegrated by the Milky Way. It should be added that most mergers do not produce a significantly increased star formation rate (SFR), but those that do tend to lie above the SFMS (Pearson et al., 2019). Only around 25 % of star formation at $z < 2$ comes from mergers (Kaviraj et al., 2015).

Other possible causes for star formation are disk instabilities and other secular processes (Kennicutt, 1998). Some studies show that for $z > 1$, gas accretion is considerably more important than mergers for the SFR (Dekel et al., 2009; Kaviraj et al., 2015; Lofthouse et al., 2017).

As the closest example of a starburst galaxy, M82 has revealed much information in star-forming regions. Images at the 21 cm line show atomic hydrogen scattering several Mpc away, indicating that M82 has for the past hundreds of Myr been interacting with the neighbouring galaxy M81. Observations by the Advanced Camera for Surveys on board the *Hubble Space Telescope* has detected ~ 150 star clusters with an average mass of $\sim 2 \times 10^5\,\mathrm{M}_\odot$ within a few 100 pc from the galactic core (Barker et al., 2008). The galaxy also show a bipolar outflow,[2] which is likely driven by the supernovae occuring around every ten years in two of the four high surface density regions (Barker et al., 2008).

When studying the SFR in a galaxy, several quantities of that galaxy has proved important. To name a few, observations of the CO line and dust continuum has found that the gas mass fraction ($f_{\mathrm{gas}} = M_{\mathrm{gas}}/(M_{\mathrm{gas}} + M_\star)$) strongly correlates with the specific star forming rate ($\mathrm{sSFR} \equiv \mathrm{SFR}/M_\star$), the gas mass fraction increases with redshift and the gas depletion timescale ($t_{\mathrm{dep}} = M_{\mathrm{gas}}/\mathrm{SFR}$) (Tacconi et al., 2018; Scoville et al., 2017; Solimano et al., 2021). With these definitions, a useful relation can be derived:

$$f_{\mathrm{gas}} = \frac{1}{1 + M_\star/(t_{\mathrm{dep}}\dot{M}_\star)}. \tag{2.2}$$

The gas in a star forming galaxy (SFG) is governed by *gas inflow* and *gas outflow* with its surrounding circumgalactic medium as well as formation of stars and return of gas from stellar interiors. Gas inflow, sometimes called gas accretion, is believed to be highly ionised and have a column density considerably lower than $10^{20}\,\mathrm{cm}^{-2}$, which is what is probed by HI-emission (Cimatti et al., 2019, subsection

[2]The shape of this peculiar galactic wind has given M82 the nickname 'the Cigar galaxy'.

8.7.4). Gas outflow, can take the form of e.g. *galactic fountains* or *galactic winds*. The previous example usually follow from *self-regulated star formation*, which is how the phenomenon of supernova shells compress the interstellar medium (ISM) and consequently starts a chain reaction of star formation. Around clusters of massive stars, superbubbles can then expand over a few hundred pc, which pushes gas out of the disc. Galactic winds are created from intense star formation in a small region and short period of time. They can help estimate the initial mass function for stars, the SFR, average supernova energy and velocity of the wind (Cimatti et al., 2019, subsection 8.7.4). From the movement of the gas outflow, the gas inflow can be estimated. Due to gravity, if the gas travels with a velocity lower than the escape velocity it will return to the galaxy.

Two parameters that are helpful when comparing star formation over the varying sizes of SFGs are the SFR surface density, Σ_{SFR}, and SFR volume density, ρ_{SFR}. A central relation for star formation in galaxies that uses these is the *Schmidt-Kennicutt law* (Schmidt, 1959; Kennicutt, 1998). The equation can be heuristically derived under the assumption that stars form when interstellar gas collapses due to gravitational forces. The SFR density should then be proportional to the gas density and inversely proportional to the free fall timescale of Equation 2.10, such that $\rho_{\mathrm{SFR}} \propto \rho_{\mathrm{gas}}/t_{\mathrm{ff}} \propto \rho_{\mathrm{gas}}^{3/2}$. The Schmidt-Kennicutt law is a generalised equivalence for column densities where the helium fraction $B \sim 10^{-4}$ is included as a factor,

$$\Sigma_{\mathrm{SFR}} = B \left(\frac{\Sigma_{\mathrm{gas}}}{\mathrm{M}_{\odot}\mathrm{pc}^{-2}} \right)^{\alpha} \mathrm{M}_{\odot}\mathrm{yr}^{-1}\mathrm{kpc}^{-2}. \tag{2.3}$$

Here, the exponent $\alpha \approx 1.4$.

Larger galaxies have larger star-formation efficiency for two reasons. First, galactic gas is more protected against background radiation. Second, the gas density is likely higher. This means that molecular gas in large galaxies have a higher recombination rate and is more difficult to ionise. Thus, their cooling is more efficient and a larger fraction of baryons can be turned into stars (see e.g. Schneider, 2006, page 524). To prevent all the gas from forming stars in a very short time, the first supernovae starts heating the surrounding gas, which makes it more dilute. But the supernovae explosions also enriches the ISM with metals and pushes the gas away, creating gravitational instabilities that, in turn, creates subsequent star formation in a chain reaction.

2.1.4 High-redshift Galaxies

Distant galaxies exist in a younger and smaller Universe. At $z \approx 2.5$ the Universe was a mere 2.6 Gyr old and had $1/(1+z) \approx 29\,\%$ the diameter of today. Changes in density and matter distribution affects the properties of the galaxies, which also has had much shorter time to evolve and change. For instance, the Hubble sequence describes the morphology of $z > 2$ poorly because low-mass galaxies have not had time to evolve, and the optical emission becomes redshifted out of the receiving optical window (see e.g. Schneider, 2006, section 9.4). Moreover, the distance to the galaxies create a need for special observational techniques that makes different galaxies difficult to compare.

Observations of galaxies at high-redshift began in the final decade of the 20th century. One early optical survey was the famous *Hubble Deep Field* from 1995, which hinted at the abundance and peculiarities of distant galaxies. However, the Hubble Deep Field covered only the U_{300}, B_{450}, V_{606} and I_{814} filters (Williams et al., 1996). Galaxies not emitting as strongly in these wavelengths were therefore excluded. In this way, troubles resolving and detecting small and redshifted sources created a need for special detection criteria that only observed some properties of galaxies. The most common observational methods are the Lyman-break method, narrow band photometry, and MIR and FIR selection (see Section 3.4.2).

With these methods, some demographical conclusions can still be drawn. As a first example, distant galaxies have a denser ISM. The gas mass fractions for $z \sim 1.2$ and $z \sim 2.2$ are ~ 0.33 and ~ 0.47 respectively, to compare with 0.08 for SFGs at $z = 0$ (Tacconi et al., 2013). Compact dusty cores, higher turbulence and deviations from the Schmidt-Kennicutt law (see Equation 2.3) are also more pertinent at higher redshift (see e.g. Messias et al., 2014; Cañameras et al., 2017; Rybak et al., 2020). Naturally, metallicity drops with redshift. Specifically, at $z = 2$ and $z = 3.5$ the metallicity of galaxies is, respectivelt, about half and one fourth of the metallicity of present day galaxies. At $z \sim 6$ galaxies appear very dust-poor (Capak et al., 2015). This affects the star formation. With metal free molecular clouds the fine-structure lines of metals are absent, and the cooling becomes efficient only above $T \geq 10^4\,\mathrm{K}$ (Baugh, 2006). It should however be added that some distant galaxies do in fact show solar-like metallicities. These galaxies have most frequently an AGN (see e.g. Schneider, 2006, subsection 9.6.3). Finally, it should be mentioned that the dust temperature vary around $25\,\mathrm{K} \lesssim T_\mathrm{d} \lesssim 65\,\mathrm{K}$ in dusty galaxies (see e.g. Kovács et al., 2006; Magnelli et al., 2010; Manning and Spinrad, 2001).

In connection with denser and more active ISMs, the SFR and luminosity depend on redshift too. SFR densities are higher for galaxies up to $z \sim 6$ than today, and the SFR density peak is around $z \sim 2.5$. This affects the luminosity function. At $z \sim 0$ the exponent of the Schechter function (see Equation 2.1) in the UV region is fitted to $\alpha \approx -1.25$ (see e.g. Galaxy formation, 1998). For $z \sim 2.5$ the faint end slope has $\alpha \approx -1.6$, and for $z \sim 4$ the slope steepens even more with $\alpha \approx -1.8$ (Cassata et al., 2011). This difference can be explained by the observed SFR peak: the SFR was considerably higher at $2 \lesssim z \lesssim 4$ than today, and young and massive stars are the main UV emitters (Bouwens et al., 2011). The number count function is highly dependent on luminosity and for longer wavelengths the comoving number density starts decreasing much earlier. In K-band light, $z \sim 2$ the characteristic density of galaxies ϕ^* is less than 30 % of today. On the other hand, the characteristic luminosity L^* is about one magnitude larger at the same redshift and waveband (Cirasuolo et al., 2010). In the sub-mm range, the comoving density of galaxies is two orders of magnitude larger than in the local Universe (Hughes et al., 1998). Considering the colour bimodality, red galaxies exist up to at least $z \sim 3$, suggesting that many galaxies formed their stars very quickly (see e.g. Schneider, 2006, section 9.4). In conclusion, high-redshift galaxies are more luminous but less numerous.

As previously stated, high-redshift galaxies do not fit the Hubble classification. Instead, most $z > 3$ galaxies are irregularly shaped due to high SFRs. At that

same redshift, the stellar mass inside quiescent galaxies is only 1/45 of today's (see e.g. Schneider, 2006, subsection 9.4.3). In regards to size, the previous paragraph suggested that the earlier Universe was more dominated by luminous and massive galaxies. The phenomenon that the relative frequency of smaller galaxies increases with cosmic time is often called *downsizing*.

2.2 First Stages in Star Formation

Stars form in dense ($n \gtrsim 10^2\,\mathrm{cm}^{-3}$) regions of giant molecular clouds (GMCs) from very cold ($T \lesssim 30\,\mathrm{K}$) gas (Cimatti et al., 2019, section 8.3). That is not to say that only molecular gas can create stars. Most of the principles presented in this subsection would hold for both molecular and atomic gas, and from a global perspective, both molecular and atomic gas does indeed correlate with star formation (Catinella et al., 2018). Dense gas clouds are twofold important; both formation of molecules, that enable higher density and effective cooling, and gravitational contraction, that eventually creates stars, depend on it.

2.2.1 Molecular Clouds Formation

Before describing these two processes, I will start with the presentation of how GMCs form. Because clouds form from pieces of the gas disk that creates a galaxy, the central mechanisms at play are instability and fragmentation. To complicate the analysis the speed of sound, c_s, on which the gravitational contraction heavily depend, varies between $<1\,\mathrm{km\,s}^{-1}$ in the cold neutral medium and $8\,\mathrm{km\,s}^{-1}$ in the warm neutral medium (Cimatti et al., 2019, page 247). Additionally, the star-forming clouds are on average larger than the scaleheight of the galactic disk which causes uneven external pressure. Furthermore, there is turbulence in the protogalactic disc. Due to the large number of complex processes and their varying importance in different galaxies, no unique theory of the formation of GMCs exists as of today.

Analysis of instabilities in the galactic medium can be modelled with respect to the rotation of the galaxy and the movement of the spiral arms. The previous cause the self-gravity of any high-density region to be counteracted both by the internal pressure and conservation of angular momentum. To model instability the potential of a single particle is often written as $\exp(-i\omega t)$, where ω and t are the angular frequency of the density wave and time. By linearly perturbing the continuity, Euler and Poisson equations in a cylindrical coordinate system and assuming adiabatic gas in purely circular motion, Lin and Shu (1964) showed that the dispersion relation for gravitational instability of a volume of gas in a rotating disk reads:

$$(m\Omega - \omega)^2 = \kappa^2 - 2\pi G\Sigma_\mathrm{gas}|k| + c_\mathrm{s}^2 k^2, \tag{2.4}$$

where m is the number of spiral arms in the galaxy, Ω and κ are the angular and *epicycle frequencies*, and $k = 2\pi/\lambda$ is the wavenumber of the fluid disk. The epicyclic frequency is defined as the angular frequency of the radial oscillations occuring from small pertubation in a closed orbit. Considering axisymmetric perturbations ($m = 0$) Toomre (1964) showed that the instability criterion ($\omega^2 < 0$) can be

simplified to

$$Q_{\text{gas}} \equiv \frac{c_{\text{s}}\kappa}{\pi G \Sigma_{\text{gas}}} < 1. \tag{2.5}$$

This criterion is called the *Toomre criterion* and Q_{gas} is known as the *Toomre parameter*. A similar analysis for star-dominated disks produces the analogous criterion

$$Q_\star \equiv \frac{\sigma_R \kappa}{3.36 G \Sigma_\star} < 1, \tag{2.6}$$

where σ_R is the radial velocity dispersion for the stars (Cimatti et al., 2019, subsection 8.3.3).

Spiral arms compresses the interstellar medium (ISM). This is due to the angular velocity of the spirals, also called *spiral pattern speed*, is constant while most disk galaxies show flat rotation curves, meaning the angular velocity of the gas decreases with distance (Cimatti et al., 2019; Sellwood and Wilkinson, 1993; Minchev and Famaey, 2010). When the gas enters the spiral arms, their high relative velocity can produce shocks which facilitates formation of dense clouds. In these clouds, molecules and, eventually, stars can form.

2.2.2 Molecular Gas Formation

The chemical processes that produce molecules involve several types of particles. Therefore, the formation rate depends strongly on the local environment. Hydrogen, for instance, form molecules on the surface of dust grains by first colliding with a dust grain in a process called *adsorption*, and subsequently colliding with another hydrogen atom on the surface before leaving the grain surface in the process of *desorption*. Primordial galaxies, with negligible metallicity, must therefore create molecular hydrogen very differently. Apart from the density of dust and hydrogen, the hydrogen formation rate is, among other factors, proportional to the cross section of the grain and the inverse of the thermal speed of the atoms. With molecular hydrogen, ionised carbon can form carbon monoxide, after additional reactions (see e.g. Cimatti et al., 2019, equation 8.31).

Molecular gas exists predominantly in GMCs that have sizes $\sim 50\,\text{pc}$, masses $\sim 10^6\,\text{M}_\odot$, temperatures $\sim 10\,\text{K}$ and number densities $\sim 500\,\text{cm}^{-3}$. Clouds contain parsec-sized clumps and 0.1 pc-sized dense cores. Stars are believed to form in clusters from clumps (Williams et al., 2000) and individually or binary from dense cores (Alves et al., 2007). The latter has densities hundreds of times that of the average in the GMC, masses $\sim 1\,\text{M}_\odot$, and are often studied from line emission of unique molecules such as OH, NH_3, CS, H_2CO and HCN (see e.g. Cimatti et al., 2019, page 121).

2.2.3 Gravitational Contraction and Thermal Pressure

According to the *Jeans analysis*, the self-gravity of a cloud of gas will dominate the internal pressure if the *Jeans criterion* is satisfied (Jeans, 1902). In essence, linearly perturbing the continuity, Euler and Poisson equations and using the superposition leads to the *dispersion relation* for the angular frequency ω:

$$\omega^2 = c_{\text{s}}^2 k^2 - 4\pi G \rho, \tag{2.7}$$

where c_s is the speed of sound in the medium with density ρ, and k is the wavenumber of the solution (see e.g. Cimatti et al., 2019, subsection 8.3.2) subsection 8.3.2).[3] The Jeans criterion, or condition for instability, is that the right hand side of Equation 2.7 is negative. This condition can be re-expressed after substituting k with the wavelength $\lambda = 2\pi/k$:

$$\lambda > \lambda_J \equiv \frac{\sqrt{\pi} c_\mathrm{s}}{\sqrt{G\rho}}, \tag{2.8}$$

where λ_J is the *Jeans length*. Assuming spherical geometry of a cloud with size λ, the analogous *Jeans mass* enables a third formulation of the Jeans criterion:

$$M > M_J \equiv \frac{\pi^{5/2} c_\mathrm{s}^3}{6 G^{3/2} \rho^{1/2}}. \tag{2.9}$$

A fourth way to express the Jeans criterion is in timescales. By defining the *sound crossing time* as $t_\mathrm{s} \equiv \lambda / c_\mathrm{s}$ the Jeans criterion reads

$$t_\mathrm{s} > t_\mathrm{ff} = \sqrt{\frac{3\pi}{32}} \frac{1}{\sqrt{G\rho}}, \tag{2.10}$$

where I have used Equation 2.8 to see that that the Jeans length is proportional to the *free fall timescale* t_ff. Clouds that do not satisfy these criteria are not held together by their own gravity and will disperse unless they are so-called *pressure-confined clouds*, that means they are stabilised by external pressure.

By plugging in values in Equation 2.8, 2.9 and 2.10 several conclusions can be drawn. To begin, the Jeans mass for cold diffuse clouds ($T \approx 80\,\mathrm{K}$, $n_\mathrm{H} \approx 10\,\mathrm{cm}^{-3}$) is $M_\mathrm{J} \approx 10^5\,\mathrm{M}_\odot$, while the same for dense molecular clouds ($T \approx 10\,\mathrm{K}$, $n_{\mathrm{H}_2} \approx 10^4\,\mathrm{cm}^{-3}$) is $M_\mathrm{J} \approx 10\,\mathrm{M}_\odot$. This means that only dense molecular clouds are prone to the fragmentation that forms individual stars; if a cold diffuse cloud exceeds the Jeans mass, a cluster of star can be formed. Further, the theoretical free fall timescale is around $10^6\,\mathrm{yr}$, one tenth of the typical lifetimes of GMCs (Murray, 2011). Thus, the thermal pressure is not the only thing stabilising the clouds.

The same conclusion can be drawn from the *Bonnor-Ebert theory* where a gaseous sphere is assumed to be isothermal and polytropic (Bonnor, 1956; Ebert, 1955; Stahler and Palla, 2004); this theory derives a mass for hydrostatic equilibrium, called *Bonnor-Ebert mass* that is $1 - 100\,\mathrm{M}_\odot$, which is proportional to the size of dense cores rather than total GMCs.

2.2.4 The Virial Theorem with Turbulence and Magnetic Fields

More important than thermal pressure are turbulence and magnetic fields, to counteract gravitational contraction in GMCs. This can be derived from the scalar virial theorem (Shu, 1992),

$$\frac{1}{2}\frac{\mathrm{d}^2 I}{\mathrm{d}t^2} = W + 2K + 2U + E_\mathrm{M}, \tag{2.11}$$

[3] The fact that analysis omits the unperturbed parts of the three equations despite these not being zero, is known as the *Jeans swindle*. However, the results for the perturbed parts still hold, fundamentally due to Hamilton's principle.

where $I = Mr^2$ is the moment of inertia of a spherical cloud with radius r and mass M, and $W = -GM^2/r$, K, $U = 3Nk_{\mathrm{B}}T$, and E_{M} are, respectively, the total gravitational, kinetic, internal and magnetic energies. The cloud radius will accelerate inwards if the right hands side of Equation 2.11 is negative. From typical GMC parameters it can be shown that $|W| \gg U$, which again shows the inadequacy of thermal pressure to withstand gravity.

The total kinetic energy from turbulence is simply the turbulent kinetic energy scaled with M:

$$K_{\mathrm{turb}} \approx M\frac{3\sigma_{\mathrm{gas}}^2}{2}, \tag{2.12}$$

where σ_{gas} is the line broadening in GMC. Observationally, $\sigma_{\mathrm{gas}} \sim 1\,\mathrm{km\,s^{-1}}$, which is around ten times the corresponding thermal line broadening (Cimatti et al., 2019, page 122-123). It is therefore evident that turbulence can sustain GMCs for $M \gtrsim 10^5\,\mathrm{M}_\odot$ — a conclusion that is known as the *second Larson law* (Larson, 1981).

The total magnetic energy is the magnetic energy density $B^2/(8\pi)$, where B is the magnetic field strength of the cloud, integrated over the volume of the cloud. By introducing the *magnetic critical mass* M_{M} the energy can be written as

$$E_{\mathrm{M}} \approx \frac{B^2r^3}{6} = \frac{G}{r}M_{\mathrm{M}}^2, \quad M_{\mathrm{M}} = \frac{Br^2}{\sqrt{6G}} \tag{2.13}$$

which, given $B \approx 10\,\mu\mathrm{G}$, means that the magnetic energy is on the same order of magnitude as the gravitational energy for $M \sim 10^5\,\mathrm{M}_\odot$.

2.2.5 The Equilibrium Model

One model of the location of baryonic matter, that has gained support over the last decade, is the so-called *equilibrium model* (Finlator, 2017; Davé et al., 2012). It follows from conservation of baryonic mass

$$\dot{M}_\star + \dot{M}_{\mathrm{gas}} = \dot{M}_{\mathrm{in}} - \dot{M}_{\mathrm{out}} + \dot{M}_{\star,\mathrm{in}}, \tag{2.14}$$

where the $\dot{M}_\star$, $\dot{M}_{\mathrm{gas}}$ are the time derivative of the mass of stars and gas in the galaxy, respectively, $\dot{M}_{\mathrm{in}}$, $\dot{M}_{\mathrm{out}}$ are the gas mass entering and leaving the galaxy, respectively, and $\dot{M}_{\star,\mathrm{in}}$ is the gas accreting into stars. Notice that $\dot{M}_\star = \mathrm{SFR}$. The *equilibrium condition* is obtained when assuming that the gas accretion into stars is negligible ($\dot{M}_{\star,\mathrm{in}} = 0$) and that gas accretion is balanced with outflows ($\dot{M}_{\mathrm{gas}} = 0$) (Bouché et al., 2010). After defining a slowly-varying *mass loading factor* $\eta = \dot{M}_{\mathrm{out}}/\dot{M}_\star$ the equilibrium condition reads

$$\dot{M}_\star = \frac{\dot{M}_{\mathrm{in}}}{1+\eta}. \tag{2.15}$$

The gas inflow can be divided into the baryonic inflow $\dot{M}_{\mathrm{grav}}$, the gas in the galactic halo that is prevented from reaching the ISM (per unit time) $\dot{M}_{\mathrm{prev}}$ and the gas that returns to the ISM from stars or previously ejected gas $\dot{M}_{\mathrm{recyc}}$. By including a *preventive feedback parameter* ζ this division can be summarised as

$$\dot{M}_{\mathrm{in}} = \dot{M}_{\mathrm{grav}} - \dot{M}_{\mathrm{prev}} + \dot{M}_{\mathrm{recyc}} = \zeta\dot{M}_{\mathrm{grav}} + \dot{M}_{\mathrm{recyc}}, \quad \zeta \equiv 1 - \frac{\dot{M}_{\mathrm{prev}}}{\dot{M}_{\mathrm{grav}}} \tag{2.16}$$

Furthermore, Finlator and Davé (2008) derives that the metallicity in the ISM is

$$Z_{\rm ISM} = y\frac{\dot{M}_\star}{\dot{M}_{\rm in}} = \frac{y}{(1+\eta)(1-\alpha_{\rm Z})}, \tag{2.17}$$

where y is the yield and $\alpha_{\rm Z} \equiv Z_{\rm in}/Z_{\rm ISM}$, where in turn $Z_{\rm in} = Z_{\rm recyc}\dot{M}_{\rm recyc}/\dot{M}_{\rm in}$ and $Z_{\rm recyc}$ is the metal mass from the recycled winds. This can be used to find an equilibrium metallicity $Z_{\rm eq} = \alpha_{\rm Z}Z + y/(1+\eta)$ (Finlator and Davé, 2008; Davé et al., 2012) but also, from Equation 2.16, an equation for the SFR

$$\dot{M}_\star = \frac{\zeta\dot{M}_{\rm grav}}{(1+\eta)(1-\alpha_{\rm Z})}. \tag{2.18}$$

The gas, metal and stellar evolution are described by Equation 2.2, 2.17 and 2.18 which together are called the *equilibrium relations*.

2.2.6 Cosmic Star Formation History

How stars are formed determines their distribution of masses at birth. This distribution function is called the *initial mass function* (IMF) and was initially described by Salpeter (1955) as

$$\Phi(m)dm = \Phi_0 m^{-2.35}{\rm d}m, \tag{2.19}$$

where $\phi(m)dm$ is the number of stars with solar mass between m and $m + {\rm d}m$, and Φ_0 is a normalisation factor, which — for a distribution between $m = 0.1$ and $m = 100$ — is assumed to be 0.17 (see e.g. Cimatti et al., 2019, subsection 8.3.9). Later versions by e.g. Scalo (1986), Kroupa (2002) and Chabrier (2003 and 2005) have attempted to correct the Salpeter IMF in the lower mass end for stars within the Galaxy. Other galaxies have produce different IMFs. In particular, population III stars are often described with the Larson IMF (Larson, 1998).

From the IMF, the SFR can be inferred from the luminosity in a specific wavelength. For instance, for the Salpeter IMF (equation 2.19) the SFR reads

$$\dot{M}_\star^{Salpeter} \sim 5\times10^{-7}L_{\lambda=1500\,\text{Å}}\ {\rm M_\odot yr^{-1}}, \tag{2.20}$$

where $L_{\lambda=1500\,\text{Å}}$ is the luminosity at $\lambda = 1500\,$Å in units of $\rm L_\odot Å^{-1}$ (Sparke and Gallagher, 2007, equation 9.24). This equation is only applicable to specific UV-luminous galaxies, but equivalent methods hold for other galaxies and star formation relations, see Section 3.4.3.

Reconstructed star formation histories (SFHs) are uncertain because they are based on several assumptions. If the luminosity-calculation-based method, mentioned above, is adapted, the IMF affects the SFR. If, for instance, the Chabrier IMF is adopted instead of the Salpeter IMF the SFR decreases by a factor of ~ 1.7 (Cimatti et al., 2019, page 429). In the method of fitting SEDs to the spectra of simple stellar population models the stellar population synthesis models are of great importance. Stellar population models are approximations of galactic spectra given a SFR and a metallicity distribution as a function of time and the stellar spectrum of an individual simple stellar population.

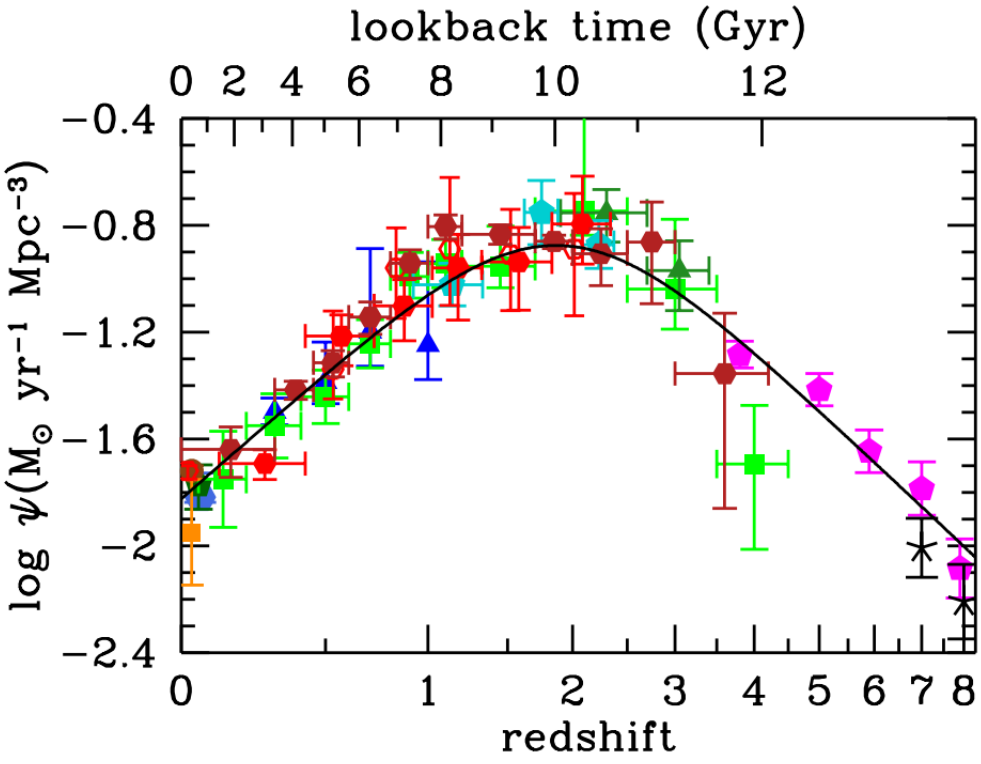

Figure 2.3: Cosmic star formation rate density as a function of redshift. Credit: (Madau and Dickinson, 2014).

By observing galaxies at various frequencies and reconstructing their individual SFH the accumulated cosmic SFH can be plotted. This is done in Figure 2.3. The figure is colour coded to represent the rest frequency and papers of presentation (Madau and Dickinson, 2014): red and brown points correspond to IR rest frame observations, and remaining symbols represent observation at FUV rest frame. Similar results have been confirmed from the *Spitzer*, *Herschel* and, more recently, *Hubble Space Telescope* (Bouwens et al., 2012). Due to the first estimate being made by Lilly et al. (1995) and Madau et al. (1996) this type of plot is known as the *Lilly-Madau diagram*.

It can be deduced from Figure 2.3 that the majority of stars formed before $z = 1$ and about 10 % formed before the SFR peak around $z \sim 2.5$. This means that high-redshift galaxies have significantly more star formation than local galaxies. Still, the most massive galaxies formed their stars early; even at $z = 2.5$, 50 % of galaxies could be quiescent. Interestingly, the cosmic star formation history follows molecular gas density history, which peaks around $z \sim 2 - 3$ (Walter et al., 2019). The slope of the star formation rate density ρ_{SFR} per redshift step is considerably steeper at current era than between $z \approx 2$ and $z \approx 8$. Indeed, at the current epoch the ρ_{SFR} is only 10 % the SFR at $z \approx 1$. Another important distinction is that the present-day SFR predominantly takes place in galaxies with relatively low dust, compared to galaxies at $z \gtrsim 0.7$.

2.3 Galaxy Evolution

The evolution of galaxies is a very active field of research that concerns a large variety of scales and processes. This section contains a brief summary of the most important ideas, with focus on more massive galaxies at redshift up to $z \approx 3$.

2.3.1 Galaxy Formation

With gravity as the dominant force acting on very large distances, primordial fluctuations would naturally cause spheres of gravitationally interacting matter to clump or — more correctly — to expand less slowly. Both baryonic matter and dark matter will, in these regions, gravitate towards high-density regions. Surprisingly, the large scale of the Universe looks less like a continuous soup of denser regions and more like clumpy web with very large voids between the filaments of matter. This hints about the complexity of the nature of physics and the initial density fluctuations (see e.g. Sparke and Gallagher, 2007, chapter 8). Given a large scale structure with primordial fluctuations, dark matter halos are believed to form as a consequence of gravitational instability, and galaxies can then form when baryonic matter contracts in these dark matter halos.

Conceptually, galaxy formation differs from star formation in two important ways: the gas is primordial, and the analysis needs to account for the expansion of the Universe. In the special case of the Einstein-de Sitter model, regions with densities at least 69 % more than the average will have collapsed before today (see e.g. Schneider, 2006, subsection 7.5.1). Similarly to the analysis in Section 2.2.3, a *cosmological Jeans mass* can be derived for the formation of dark matter halos. However, this assumes that the density perturbations are very small. Moreover, the cosmological Jeans mass changes significantly during the collapse. To estimate the mass threshold for gas collapse, a time-averaged version, called the *filtering mass*, is often used instead (Gnedin, 2000).

Galaxies form in dark matter halos. For high-mass halos, the thermal pressure dwarfs the gravitational attraction making baryons fall towards the centre of the halo, supersonically. This means that the infall speed exceeds the speed of sound. If the mass of the halo exceeds the theoretical *shock mass* ($M_{\text{shock}} \sim 5 \times 10^{11}\,\text{M}_\odot$), the infalling gas creates shock fronts. The kinetic energy of the shocks dissipates into heat. In the centre, an hydrostatic equilibrium already exist. The infalling shock wave heats the gas to the equilibrium temperature. This temperature, called the *virial temperature*, is the temperature when the thermal energy U equals the kinetic K energy which equals half the potential energy W. A typical order of magnitude approximation is $T_{\text{vir}} \sim 10^6\,\text{K}$.

Since the thermal pressure, which counteracts gravity, increases with gas temperature, stars can only form after the gas has cooled. The dominant way of cooling depends on the temperature, density and constituents of the gas. Examples of cooling processes are radiative Bremsstrahlung, recombination, de-excitation and collisional ionisation and excitation.

When weighing the importance of these process, one useful approximation for temperatures that ionise hydrogen ($T > 10^4\,\text{K}$) is the *collisional ionisation equilib-*

rium. In it, the photoionisation is neglected, ions and neutral atoms are assumed to immediately emit radiation when excited, and equilibrium is assumed to hold. After defining the *cooling rate* C as the energy radiated away per unit time and unit volume, it follows that it can be expressed as a temperature dependent cooling function $\Lambda(T)$ times the number density of hydrogen n_{H}, $C = \Lambda(T) n_{\mathrm{H}}^2$ (Baugh, 2006; Sutherland and Dopita, 1993). Because hydrogen lacks a permanent dipole moment (see Subsection 3.4.1) cooling is more efficient for higher metallicity and temperatures above $10^4\,\mathrm{K}$. This is also the reason why star formation takes place in clouds with molecules; the energy levels are much richer at the low temperatures that gravitational contraction presupposes.

Given cooling function, gas will contract unhindered if the corresponding *cooling timescale* t_{cool} is shorter than the free fall timescale (see Equation 2.10):

$$t_{\mathrm{cool}} = \frac{3 n k_{\mathrm{B}} T}{2C} \lesssim t_{\mathrm{ff}}, \tag{2.21}$$

where n is the number density, and T is the temperature of the gas. Halos cannot cool effectively if $M > 10^{13} \rho / \rho_{\mathrm{g}}\,\mathrm{M}_\odot$, where ρ and ρ_{g} are the total and gas density, respectively. This is the reason why groups or clusters of galaxies, having larger masses, cannot produce stars. It is also the reason why galaxies have $M \gtrsim 10^8\,\mathrm{M}_\odot$; smaller M yields smaller T and the cooling is very inefficient below $10^4\,\mathrm{K}$. Moreover, because of the expansion of the Universe, higher redshifts correspond to higher densities, which makes the cooling more effective. Therefore, if low-mass halos has formed stars, these are likely very old. Finally, as stated above, an increased metallicity improves the cooling efficiency (see e.g. Mo et al., 2010; Schneider, 2006; Cimatti et al., 2019).

Two corrections to this story of galaxy formation should be made. Firstly, it is likely that the gas density increases towards the centre of the halo. Cooling can then be efficient in the central regions and a galaxy can be formed in the dark matter halo that contains hot gas in its outermost regions. Secondly, since the large scale structure is more like a web than a soup, the halos are not completely spherical. Instead, they can be thought of as the 'knots' connecting the 'threads' on which dark and baryonic matter travels.

These two corrections lead to two general modes of gas accretion: the hot and the cold mode. Which mode that dominates depends on whether the mass of the galactic halo supersedes the shock mass. In more massive galaxies, the hot mode dominates and gas is heated to virial temperatures through shocks. In less massive galaxies, cold gas maintains low temperature until it reaches the centre of the halo (Sancisi et al., 2008). For $z \gtrsim 1.5$ a third mode of gas accretion exists: a more massive halo that would otherwise accrete via the hot mode can for a larger z accrete through gas filaments or streams leading down to the centre of the halo. In these streams, the density is higher and therefore the cooling time is shorter (Dekel et al., 2013).

The idea of galaxy formation is summarised in Figure 2.4. From primordial fluctuations a dark matter halo amasses and attracts baryons that heat through shocks to the virial temperature. If the inner regions are protected against radiation and also are dense enough, then cooling could be efficient and galaxy sized clouds

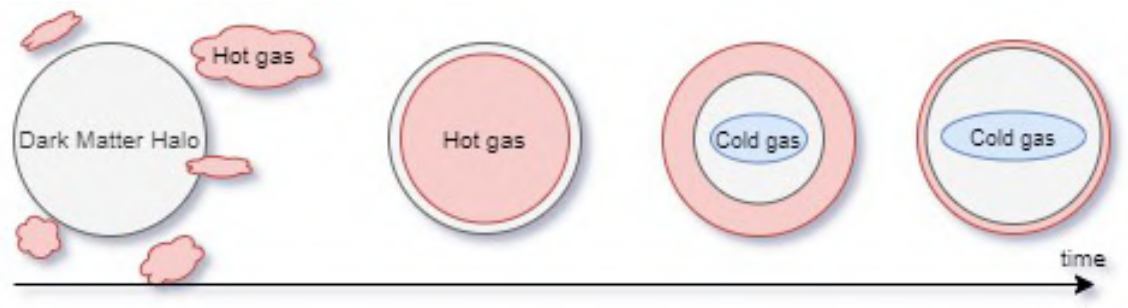

Figure 2.4: Schematic illustration of galaxy formation.

can form and eventually produce stars. The preservation of angular momentum creates rotational support for the protogalactic disk, which creates turbulence, which together with magnetic field counteracts gravitational collapse of GMCs. As the cooling precedes, the radius of the galactic disk grows to the *virial radius* $r_{\mathrm{vir}} = GM/v^2$, where v is the rotational velocity of the gas.

2.3.2 Simulations of Galaxy Evolution

It is tempting to assume that much of galaxy evolution is known simply by applying the previously mentioned relations between time (or redshift) and some other parameter. The theory of reionisation and galaxy formation suggests that the first galaxies formed around 1 Gyr after the Big Bang (or at $z \sim 10$). As gravitational attraction sparked merger events and gas accretion the cosmic SFR density increased to peak around $z \sim 2.5$. The vaster Universe after this peak allowed galaxies to restructure according to the Hubble sequence. On this path, galaxies moved diagonally upwards on the SFMS until the star formation was quenched. Then, the galaxies transformed from blue to red.

There is however a fundamental problem with this assumption: applying different selection criteria at different redshifts results in a difficulty inferring something about galaxy evolution. Observing different properties of galaxies at different distances makes it problematic to argue that they represent different stages on the same sequence of galaxy evolution. Telescopes enable us to, in some way, observe galaxies up to $z \sim 10$ and thereby studying 90 % of the cosmic history, but the selection biases leave gaps in the theory of galaxy evolution.

To combat this problem hydrodynamical cosmological simulations and semi-analytical models are often used. Of course, simulating the entire history of the Universe is unfeasible, but several simplifications can leave the large-scale results fairly reliable.

Hydrodynamical simulations have lower spatial resolution than N-body simulations. They can, however, account for more physical processes. These small-scale physical mechanisms, such as star formation, are in these simulations added on sub-grid scales. Many baryonic processes, such AGN and supernovae feedback, are nevertheless difficult to model. This the reason for many unknowns in galaxy evolution. Still, several conclusions of hydrodynamical simulations are reasonable and in line with observations. Comparisons between observations and such simulations

enables fitting of parameters that are unknown. In this way, information can be obtained (see e.g. Schneider, 2006, section 10.6).

An example of a comprehensive gas-dynamical, large-scale simulation is presented by Vogelsberger et al. (2013). By simulating a $25h^{-1}\,\mathrm{Mpc}$ large region with and without feedback processes it was shown that density, temperature and metallicity were spread greatly outside the filaments in the large-scale structure only when gas feedback was included. Gas feedback also regulates the star formation to levels comparable with the Lilly-Madau diagram (see Figure 2.3). If the galactic winds produced by supernovae are strong, much of the gas from galactic halos is removed initially, but gas that is reaccreted at later times stays within the galaxy. Fast winds, instead blows gas out from the galaxy at lower redshifts. For this reason, fast winds also produce a lower ratio between stellar mass and halo mass than what is observed. When it comes to the Schechter luminosity function both strong and fast winds predicts lower mass functions Φ while no feedback overestimates it. Having no AGN feedback would also overestimate the slope in the Tully-Fisher relation.

Semi-analytical models are less computationally expensive than hydrodynamical simulations. The idea behind these models is to start with the dark matter distribution obtained from N-body simulations. These simulations only account for gravitational interactions. Given the primordial overdensities extracted from the CMB, these simulations can produce the web-like large scale structure. When a dark matter halo has formed a homogeneous distribution, a baryon density equal to the cosmic mean is assumed in the region. With these conditions, analytical functions of galaxy formation and baryon processes are used to describe the baryon behaviour. For instance the surface SFR density is parameterised as the Schmidt-Kennicutt law 2.3.

In a semi-analytic model from 2008, Somerville et al. demonstrated the regulation of star formation from supernovae and AGN. Neglecting supernovae feedback resulted in a fraction of baryons, that was in the form of stars, that was considerably larger than 50 % for halo masses $M_{\mathrm{halo}} \lesssim 10^{12}\,\mathrm{M}_{\odot}$. Similarly, not including AGN feedback resulted in the baryon-in-stars fraction to be almost one order of magnitude higher than expected, for $M_{\mathrm{halo}} > 10^{12}\,\mathrm{M}_{\odot}$. This is clearly different from the observations that show that star formation is inefficient when the halo mass is far from $10^{12}\,\mathrm{M}_{\odot}$. The theoretical explanation for this is that supernovae and AGN feedback heats the ISM which slows down star formation.

Another semi-analytic model can explain why central cluster galaxies often have AGNs. Almost every massive galaxy at high redshift contains a SMBH (Kormendy and Ho, 2013). As these central black holes accrete gas they grow in size and produce an accretion disk of extremely hot and luminous particles — the AGN (Soltan, 1982). More massive galaxies are also more likely to attract more galaxies. Therefore, as shown in the Millennium simulation (Springel et al., 2005), the most luminous AGNs at high redshift ($z \sim 6$) will dominate as central galaxies in a cluster at $z \sim 0$.

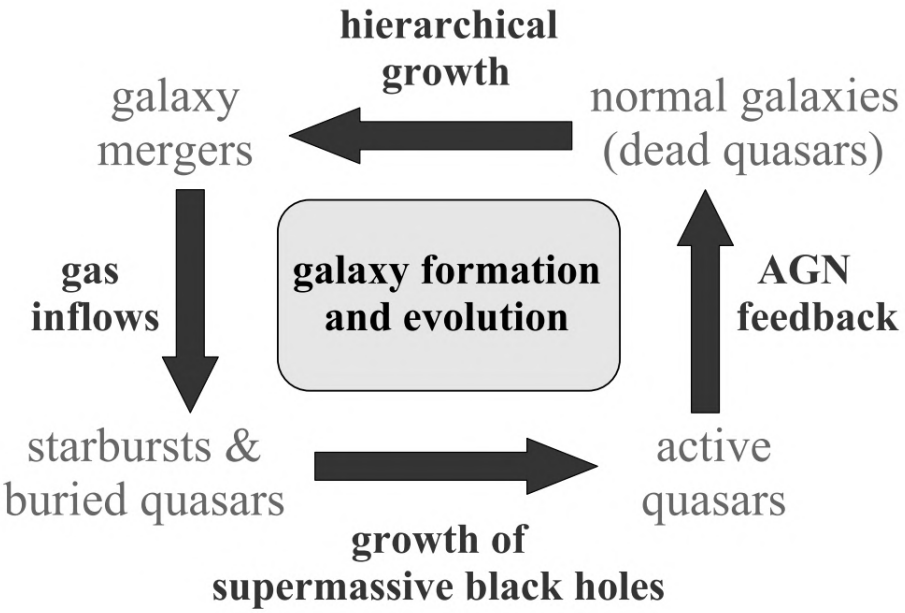

Figure 2.5: Schematic view of the cosmic cycle for massive galaxies. Credit: (Hopkins et al., 2006).

2.3.3 Summary of Galaxy Evolution

The evolution of massive galaxies is often simplified as the *cosmic cycle* — see Figure 2.5. Gas inflow from the formation of the galaxy starts a period of starburst activity. If the central SMBH will evolve to an optically unobscured AGN, known as an active quasar, or — originally — quasi-stellar object (QSO), the galactic core is referred to as a buried quasar. Gas accretion into the central regions feeds the SMBH which causes intense AGN feedback for a period of $\sim 100\,\mathrm{Myr}$ (Hopkins et al., 2006). Inside the produced normal galaxy, or dead quasar, steady star-formation proceeds as well as the growth of bars and pseudobulges. Gravitational attraction can eventually cause galaxies to merge. This event creates starburst periods which can be characteristic for e.g. ULIRGs. Subsequently, the galaxies coalesce in a violent relaxation in the galactic core, which possibly creates a new quasar as the cycle begins again. An important correction to this cyclic idea is that after the AGN feedback the galaxy is redder than before the merging. This is because the SFR has dropped and there are significantly more old red stars than young blue ones.

The quenching of star formation can occur in many ways. Two previously mentioned examples are feedback from supernovae and AGNs that keeps the ISM hot. Another example, *Mass quenching*, occurs when the dark matter halo, possibly through merging, exceeds the critical mass which is $M_{\mathrm{crit}} \sim M_{\mathrm{shock}} \sim 10^{12}\,\mathrm{M}_{\odot}$. In this case, the cold mode accretion becomes inefficient and the winds from the supernovae $v_{\mathrm{SN}} \sim 100\,\mathrm{km\,s^{-1}}$ dwarfs the escape velocity. While gas in the ISM can still cool and form stars, further accretion of cold gas is difficult if the virial temperature is high enough. If $M_{\mathrm{halo}} \gg M_{\mathrm{crit}}$ AGN feedback prevents star formation almost completely (see e.g. Gabor et al., 2010; Cimatti et al., 2019, subsection

10.6.1). Mass quenching explains why red galaxies are heavier.

Environmental quenching is due to the interaction of nearby galaxies. A gravitationally dominating galaxy can control the movement of the gas in the intracluster medium. The ISM of orbiting satellite galaxies can then be pushed out of the galaxy from the pressure of the intracluster medium. This process is called *ram-pressure stripping*. If the satellite galaxy moves closer to the central galaxy all gas is attracted to the central galaxy instead of the satellite due to the process of *strangulation*. At even shorter distances, the central galaxy can absorb the satellite. This has got the dramatic name '*cannibalism*'. These environmental effects explains the *Butcher-Oemler effect*, which is the hypothesis that cores of intermediate redshift galaxies have a larger fraction of blue cores (see e.g. Cimatti et al., 2019; Schneider, 2006).

The fraction of galaxies that merge increase with redshift. Selecting galaxies with a projected separation and velocity difference of $<5-30\,\mathrm{kpc}$ and $<200\,\mathrm{km\,s^{-1}}$ the merger fraction can be estimated as

$$f_{\mathrm{merger}} = f_{\mathrm{merger},0}(1+z)^{\alpha} \quad \text{for } 0<z<3, \tag{2.22}$$

where $f_{\mathrm{merger},0}$ is the merger fraction at $z=0$, and α depends on the stellar mass of the galaxy $M_\star$ (Khochfar and Burkert, 2001; Conselice et al., 2003; Man et al., 2016). For instance for $M_\star \gtrsim 10^{10}\,\mathrm{M}_\odot$, the exponent is around $\alpha \approx 1$. Alternatively, the number of mergers per comoving volume and time is stable for low redshifts and starts declining only after $z \sim 1.5$. However, this is under the assumption that merger timescale is constant with redshift. If instead it decreases with redshift, the merger rate might be a function that increases with redshift (see e.g. Cimatti et al., 2019, subsection 11.3.2). Finally, high-redshift mergers are less efficient at increasing the SFR than low-redshift mergers (Fensch et al., 2017).

Hubble morphologies have been observed up to $z \sim 4$, but start become significantly numerous around $z \sim 2$. At this redshift the combined fractions of disk galaxies and spheroids equals the fraction of peculiars. At higher redshift peculiars, or irregulars, are vastly more abundant, increasing from $\approx 5-10\,\%$ at $z \approx 0$ to $\approx 30\,\%$ at $z \approx 0.6$ and $\approx 60-70\,\%$ at $z \approx 2.7$ (Talia et al., 2014). For a given $M_\star$, spheroids grow quicker than disks . In detail, the effective radius at $0<z<3$ follows the dependence $R_\mathrm{e} \propto (1+z)^{\alpha}$ where $\alpha \approx -0.7$ for disks and $\alpha \approx -1.5$ for spheroids (Mundy et al., 2017).

Arguably the most important parameter in galaxy evolution is galaxy mass. Galaxies with $M_\star > 5\times10^{10}\,\mathrm{M}_\odot$ evolved to disks or spheroids earlier than lower-mass galaxies. Due to their gravitational attraction they are more prone to mass quenching and less dependent on their surrounding. Therefore, massive galaxies mature quicker and become red, retired galaxies. More massive galaxies have systematically lower gas mass fraction, lower sSFRs and higher metallicity at all redshift (see e.g. Cimatti et al., 2019).

The gas mass fraction in the ISM increases with redshift as $M_\mathrm{gas}/M_\star \propto (1+z)^{\alpha}$ where $\alpha \approx 3$ for $0<z<3$ (Genzel et al., 2015). The most important reason for this, and the fact that metallicity decreases with increasing z, is that star formation depletes the gas. At $0<z<3$ the depletion timescale has only a weak redshift dependence ($t_\mathrm{depl} \propto (1+z)^{-0.3}$) and is on the order of 1 Gyr (Genzel et al., 2015). SFGs that remain in the SFMS over several Gyr must therefore continuously accrete

gas.

The evolution of the SFR is closely related to the cosmic star-formation rate density which in turn follows the cosmic gas mass fraction history and peaks around $z \sim 2.5$ (Madau and Dickinson, 2014). This shows in the luminosity function. In the case of IR emission, L^*_{IR} increases by at least one order of magnitude between $z \sim 0$ and $z \sim 2-3$ (Gruppioni, 2013). Observations have confirmed that the sSFR increases considerably with redshift (Ilbert et al., 2015). At $z \approx 2$ galaxies on the SFMS typically double their stellar mass within 1 Gyr. The SFMS also evolves with redshift as $\mathrm{SFR_{MS}} \propto (1+z)^{\alpha}$ where $\alpha = a \log M_\star + b$, and $a \approx 0.2$ and $b \approx 0.6$ (see e.g. Cimatti et al., 2019, equation 11.20).

The theory of galaxy evolution is summarised in Figure 2.6, with one half focusing on the morphological evolution and the other on the star formation evolution. Inside a dark matter halo baryons could collapse into a dense medium with a virial temperature. Galaxies below the critical mass $M_{\mathrm{crit}} \approx 5 \times 10^{11}\,\mathrm{M}_\odot$ can accrete gas in the cold mode. More massive galaxies accrete gas in the hot mode or, at $z > 2.5$, possibly through cold streams. Supernova and AGN feedback together with higher virial temperatures complicates the process of cooling and collapsing the gas to a disk, although further gas accretion can, at least hypothetically, transform spheroids to S0 galaxies. Merger events increase the SFR and disorder the stellar motions more significantly at low redshift. Dry mergers result in less gravitational instabilities in dense molecular clouds, because these clouds are more rare. A SFG can become starburst through major wet mergers or star formation chain reactions of e.g. supernova shocks in its early history. Starbursts drop towards the SFMS after a few Myr due to less gas remaining or, if star formation chain reaction has nearly exhausted the galaxy of gas, it becomes quiescent galaxy. These galaxies have been observed out to $z \sim 3-4$ (Cimatti et al., 2019, see e.g.).

Many challenges remain in the understanding of galaxy evolution. Observations of distant galaxies up to the epoch of reionisation are only now becoming feasible. To study high-redshift galaxies, gravitational lensing and other selection biases need to be used. With a proper understanding of these, as well as simulations and astronomical models, the observations of distant epochs can be interpreted as the observable representations they are.

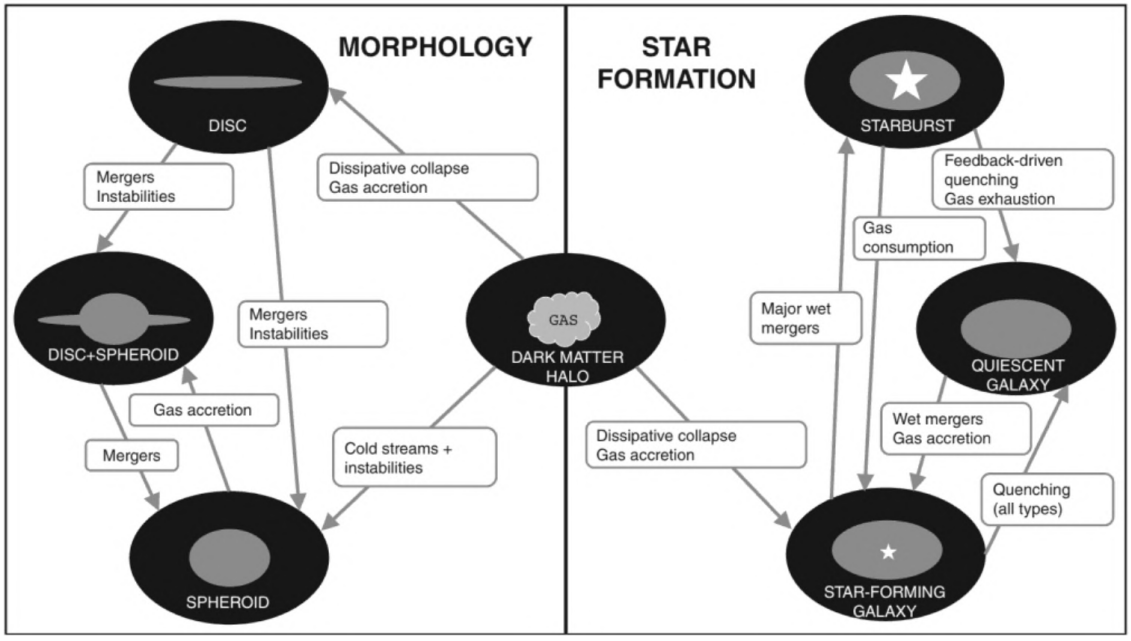

Figure 2.6: Galaxy evolution summarised. Credit: (Cimatti et al., 2019, Figure 10.18).

3

Observations of Galaxies and Radio Astronomy

Radio astronomy studies celestial objects and phenomena in radio frequencies, i.e. 3 kHz (λ =100 km) to 300 GHz (λ =1 mm). This includes almost all astronomical sources, but some especially important examples are the CMB, masers, radio galaxies, strongly gravitationally lensed sources, and thermal spectral lines from molecular clouds. The final two examples will be of special importance to this thesis.

In this chapter, the techniques and theory that enables observation of radio astronomical sources is presented. It is explained how these observations are antenna measurements of extraterrestrial photons that depend on the dimming or refraction from gas and dust, the antenna structure, the receiver circuit and the source target. Sources are often specific transitions of molecules, corresponding to specific processes. Some observatories, such as ALMA, use interferometric imaging to improve the resolution. This can also be achieved with the bending of light in gravitational lensing.

3.1 Observational Quantities

Astronomy measures extraterrestrial photons. For this aim, several quantities are important. *Intensity*, I, or *brightness*, quantifies the number of photons per unit area and solid angle. The *specific intensity*, I_ν, or *spectral brightness*, is the intensity measured at a given frequency ν. *Flux*, S, quantifies the number of photons per unit orthogonal area A of the observer, and *flux density*, S_ν, is the frequency specific equivalence. For radio sources it is conventional to use the flux density unit of Jansky, where 1 Jy=$10^{-26}\,\mathrm{Wm^{-2}\,Hz^{-1}}$.

Flux measurements depend on the absorption, scattering and emission along the line of propagation. In the ray-optics approximation this line of propagation is a straight for distances much larger than the wavelength. The equation of radiative transfer,

$$\mathrm{d}I_\nu = j_\nu \mathrm{d}s - \kappa_\nu I_\nu \mathrm{d}s \ , \tag{3.1}$$

where j_ν is the specific emission, and κ_ν is the specific absorption, and $\mathrm{d}s$ is an infinitesimal distance, explains that the differential specific intensity is the difference between the differential specific emissivity and specific absorptivity. This can be reformulated introducing the dimensionless quantity optical depth, or opacity, $\mathrm{d}\tau = -\kappa \mathrm{d}s$, that measures the amount of absorptive matter that is viewed.

Further, in local thermal equilibrium $\mathrm{d}I_\nu/\mathrm{d}s = 0$ and I_ν = blackbody radiation. In the Rayleigh-Jeans low frequency approximation, $h\nu \ll k_\mathrm{B}T$, the brightness temperature is defined as

$$T_b(\nu) = \frac{I_\nu c^2}{2k_B\nu^2}, \tag{3.2}$$

where c is the speed of light in vacuum and k_B is Boltzmann's constant. Similarly, the antenna temperature, T_a, is the imagined temperature the antenna would have if it were a blackbody source that emitted the measured noise. Antenna temperatures can therefore be calibrated with known-temperature resistors called 'loads'. Both the antenna and the brightness temperature are mathematical tools; they are not physical. With these new quantities, the radiative transfer equation becomes

$$T_\mathrm{a} = T_\mathrm{a}(0)e^{-\tau_\nu} + T_b(1 - e^{-\tau_\nu}). \tag{3.3}$$

The opacity is generally wavelength-dependent. One special feature of radio emission is that it is not affected by molecules and dust particles that are smaller than the wavelength of the emission. Thanks to this feature, Sagittarius A, in the center of the Milky Way, was discovered (Balick and Brown, 1974). In space, the term 'dust grains' denote all small solid particles. Dust generally scatters or absorbs photons, causing a dimming known as extinction. Elliptical galaxies have generally less dust than starburst and disk galaxies.

In the atmosphere of Earth, the wavelength-dependent opacity is a product of the molecules that constitute it. The abundant molecules, H_2O, CO_2 and O_2 in the troposphere allow for vibrational transitions with the same energy as MIR photons and rotational transitions with the same energy as longer radio photons (Condon and Ransom, 2018). This leaves a radio atmospheric window in between 10 MHz and 1 THz where photons are generally not absorbed. Thus, radio telescopes can be ground-based.

For wavelengths longer than ten times the particle size, electromagnetic dispersion obeys the rules of Rayleigh scattering: opacity $\propto \nu^2$ (Condon and Ransom, 2018). One important scattering source is small water droplets, known as hydrosols. To predict the opacity due to water, the precipitable water vapor (PWV) is introduced. It is the depth of the atmospheric water column, and is proportional to the water vapor spectral line at 22.235 GHz. At ALMA, the measured 50 % quartile is PWV= $1.1^{+1}_{-0.5}$mm[1]. The PWV is also proportional to the atmospheric phase change; more water increases the refraction angle according to Snell's law.

3.2 Antennas

According to The American Heritage dictionary, a telescope is an instrument for observing optical radiation from distant objects. Antennas are the equivalent for radio waves. More precisely, they are the interface between freely propagating electromagnetic waves and the current that travels in the receiver.[2] Antennas measure

[1] `https://slideplayer.com/slide/3860722/`.

[2] IEEE standard for definitions of terms for antennas.IEEE Std 145-2013(Revision of IEEE Std 145-1993), pages 1–50

the flux intensity

$$S_\nu = \frac{P}{A\delta\nu} = \frac{P_\nu}{A} = \frac{1}{2} I_\nu \Omega \tag{3.4}$$

given a electromagnetic power P, receiver area A and a frequency range $\delta\nu$ for the incoming photons (Cortes et al., 2020, Chapter 3). The received electromagnetic power P_ν per unit frequency is usually half the specific intensity I_ν times the solid angle Ω because receivers generally only detect one polarisation. ALMA, however, has two independent and simultaneously active receivers, which makes this coefficient one. Thus, the size of the antenna regulates its sensitivity by deciding how much power that can be detected.

The shape of an antenna determines its sensitivity in different directions, known as its power response. On a radial axis, this is usually a collection of Gaussians with decreasing amplitude. The central lobe is called the primary beam. A larger antenna diameter yields a more narrow primary beam, which means that angularly smaller sources can be observed.

Often antennas are parabolas because then each fraction of an transverse plane wave front will travel the same distance to the receiver regardless of where on the parabola it strikes. If an antenna points in a different direction than that of the source the resulting phase difference will produce destructive interference which decreases the received amplitude.

3.3 Confusion and Noise

Depending on which direction an antenna is pointing to, different background radiation and collection of sources is observed. In radio frequencies, the 2.726 K blackbody CMB radiation is the dominating background. Additionally, unresolved sources blend together creating the confusion limit that is only dependent on the ratio between the angular resolution of the observatory and the angular size of the source.

Noise is the unwanted data that follows wanted data. In receivers, noise is usually assumed to have the same probability for any specific amplitude in any frequency. It is completely random and thereby called stochastic or *white noise*. With Johnson–Nyquist's theorem, $P = kT\delta\nu$,[3] the noise power can be expressed as a temperature (Wilson et al., 2013, equation 1.42). Consequently, the noise from the receiver can be expressed as a temperature T_{rec} too. With the system temperature introduced as $T_{\text{sys}} = T_{\text{a}} + T_{\text{rec}}$, where T_{a} is the antenna temperature from Equation 3.3. The smallest detectable temperature resolution is now given by the ideal radiometer equation

$$\Delta T \propto \frac{T_{\text{sys}}}{\sqrt{\delta\nu\tau}}, \tag{3.5}$$

where τ is the integration time or the time of observation for the signal (Wilson et al., 2013, equation 4.41). In reality, ΔT is larger due to systematic errors, but

[3]Note that an infinite bandwidth $\delta\nu$ would produce an infinite power P. This is the famous ultraviolet catastrophe. The catastrophe is not physically true because Nyquist's theorem, or equivalently, the Rayleigh-Jeans approximation, is not applicable on infinite bandwidths.

the time dependence is generally on this form.[4] Specifically, for ALMA the noise can be expressed in mJy as

$$S_{\text{noise}} = \frac{k_B T_{\text{sys}}}{AN^2\sqrt{N_p \delta\nu\tau}}, \tag{3.6}$$

where A is the area for each of the N antennas and N_p is the number of polarisation directions observed.

A signal is intelligible if the signal-to-noise ratio (SNR) is large enough. The components are often distinguished with the root-mean-squared (RMS) error. Because of its definition, the RMS is inversely proportional to the square root of the channel width $\delta\nu_{\text{ch}}$. This leads to a useful result when resampling data in new bins:

$$\text{RMS}_{\text{new}} = \text{RMS}_{\text{old}}\sqrt{\frac{\delta\nu_{\text{ch}}^{\text{old}}}{\delta\nu_{\text{ch}}^{\text{new}}}}. \tag{3.7}$$

If the average value for a region without a signal is zero, the RMS coincide with the standard deviation, which is the typpical difference between a data point and the mean. Thus, the RMS proves decisive for the credibility of a result.

3.4 Selection Criteria

Among the many parameters an astronomer must specify before an observation of a source, the frequency band and resolution determine what parts of that source are studied. For a given redshift, lower frequencies correspond to less energetic photons according to the formula

$$E = h\nu, \tag{3.8}$$

where h is Planck's constant. Observed emission can be divided into two categories: continuum- and line emission. Studying any features in the spectral energy distribution (SED) can be a reason to have a good spectral resolution.

Typically, continuum emission has a higher SNR and is less dependent on sensitivity than line emission, because it is observed over a broader frequency range. Since any spectral features are hidden from summing all spectral channels to one channel, the emission profile is assumed to already be known. A first example of this is how measuring the emission of particular stars can be fitted to a blackbody curve (Suzuki and Fukugita, 2018).

A second, for this thesis more relevant, example is dust emission, whose SED can be approximated as a Rayleigh-Jeans distribution for $\nu < \nu_{\text{peak}}$ where ν_{peak} is the frequency of the peak luminosity (e.g. Nersesian et al., 2021; Boulanger, 1999). A property of this distribution is that ν_{peak} can identify the temperature of the dust. Since dust scatters and absorbs UV to NIR light from stars and re-emits thermal radiation, it is most easily seen in FIR and millimeter wavelengths. It is also an important catalyst for many species, including H_2, that are necessary for

[4] This is in essence the central limit theorem and is only applicable when, in this case, $\delta\nu\tau$ is large.

star formation (e.g. Minissale et al., 2016). Therefore FIR emission is a great tool for finding and observing star-forming galaxies (see e.g. Davies et al., 2013; Casey et al., 2014). In sum, dusty, star-forming galaxies (DSFGs) produce IR radiation with an energy density equal to, or exceeding, that of starlight in the optical and UV (e.g. Casey et al.,2014). It has been suggested that stars that we see today have predominantly formed in DSFGs since $z \sim 4$ (Zavala et al., 2021).

Line emission is, in many cases, a necessary tool for astronomical measurements. A first reason for this is that line emission is easily separated from continuum emission when the spectral resolution is higher than the line width, and the signal is brighter than background emission. Secondly, since given transitions yield emission at specific frequencies, the redshift and thus also the approximate distance can be calculated. Thirdly, and most importantly, line emission corresponds to specific processes. Therefore a galaxy has different appearances in different frequencies, not just on large scales, but also on small scales.

There are several well-known examples of astronomical lines. The most famous of these is the HI 21 cm line, produced when the spin in the electron and proton of a hydrogen atom changes from being parallel to anti-parallel. This is an example of hyperfine-splitting in the energy levels. The abundance of neutral atomic hydrogen together with it having low opacity makes it a good probe for mass calculations as well as kinematic surveys (Dickey and Lockman, 1990). Another example of frequently used lines are the far-infrared atomic fine-structure lines, in particular that of ionised carbon, [C II], which extended line structure correspond with increased star formation among others (Fujimoto et al., 2020). The [C II] at 158 µm line is typically the strongest line in star-forming galaxies (see e.g. Fujimoto et al., 2020; De Looze et al., 2014). It is an example of an atomic fine structure line. Other examples are [O I], [C I], [N II], and [O III]. Molecular and atomic fine structure lines has become an important probe for the cool interstellar medium (ISM) in star-forming galaxies (Carilli and Walter, 2013).

For completeness I might add that absorption lines are another important astronomical tool, but this requires strong continuum emission behind a region of gas, and since this thesis focuses on star formation in distant galaxies the following inspection will focus on molecular gas and particularly carbon monoxide.

3.4.1 Carbon Monoxide Probing

Line emission exists due to the quantum mechanical principle that energy is quantised. Consequently, atoms, ions and molecules can arrange their constituting particles in a ground state or a range of excited states. Interactions, i.a. with electromagnetic fields, can split these electronic states into vibrational levels which in turn give fine structure lines to the vibrational lines by splitting into rotational energy levels J with energy (Condon and Ransom, 2018, section 7.7):

$$E_{\text{rot}} = \frac{\hbar^2}{2I} J(J+1), \tag{3.9}$$

where $\hbar = h/2\pi$ is Planck's reduced constant and I is the moment of inertia. From conservation of angular momentum $\Delta J = \pm 1$ which means that the energy that is

released from energy level J is $\Delta E_{\rm rot} = \hbar^2 J/I$.[5]

Symmetric molecules lack permanent electric dipole moment and must therefore rely on the larger spacings corresponding to the quadrupole moment. The hydrogen, H_2, molecule, which is the most abundant molecule, is both symmetric and has a small I. Therefore, rotational excitations occur only when $T_{H_2} \geq 500\,\mathrm{K}$. Instead, rotational transitions for the more massive, polar carbon monoxide, CO, molecule are detectable radio emitters at low temperatures. In fact, they are the predominant cooling process for interstellar gas with temperatures between 10 and 50 K (Sparke and Gallagher, 2007, table 2.5).

Line luminosities are the integrated luminosity of a line. At high redshift, this is commonly approximated and expressed in two ways (Solomon et al., 1992)

$$L_{\rm line} = 1.04 \times 10^{-3} S_{\rm line}\Delta v D_L^2 \frac{\nu_{\rm rest}}{1+z}\ \mathrm{L}_\odot, \tag{3.10}$$

$$L'_{\rm line} = 3.25 \times 10^{7} S_{\rm line}\Delta v \frac{D_L^2}{(1+z)\nu_{\rm rest}^2}\ \mathrm{K\,km\,s^{-1}\,pc^2}, \tag{3.11}$$

where $S_{\rm line}\Delta v$ is the observed velocity integrated line intensity in $\mathrm{Jy\,km\,s^{-1}}$, D_L is the luminosity distance in Mpc, and $\nu_{\rm rest}$ is the rest frequency in GHz. While $L_{\rm line}$ is more convenient when studying cooling efficiency, $L'_{\rm line}$ is frequently used when estimating the H_2 mass from the CO emission.

When CO molecules are excited it is usually in collisions with other particles, and with an abundance ratio $H_2/\mathrm{CO} \sim 10^4$, CO emission, CO emission can trace effectively all molecular gas (Cimatti et al., 2019, section 4.2.5). In fact CO lines are, together with dust continuum, the dominating tracers of gas at high redshift (see e.g. Omont, 2007; Solimano et al., 2021). The ratio of CO velocity integrated surface brightness to H_2 column density, is called the X-factor and it depends on multiple factors. For example, $X_{\rm CO}$ often drops in star-forming galaxies and sometimes in central and bright regions in galaxies (Bolatto et al., 2013). For high-redshift, main sequence galaxies, Genzel et al. find a metallicity dependence $X_{\rm CO} \propto Z^{-1.3} - Z^{-1.8}$. For young, low-metallicity galaxies the conversion factor is likely higher but the [C II] line or dust continuum could be a better probe for the hydrogen abundance (Bolatto et al., 2013). The X-factor is important because while CO cools molecular gas, it is the hydrogen that stands for most of the mass and therefore also the star formation. More precisely, too account for helium a factor $\sim 1.3 - 1.4$ is often needed. For distant galaxies, clouds are not well resolved and the total mass to CO line luminosity is used instead. This quantity is called $\alpha_{\rm CO}$ and has units of $\mathrm{M_\odot\,(K\,km\,s^{-1}\,pc^2)^{-1}}$.

The intensity of different transitions lines trace gas at different temperatures. The line emission for the rotational transition of $J = 1$ to $J = 0$ of CO is best suited for tracing H_2 and, at high redshift, CO (Emonts et al., 2014). Excitation temperature increases from 5.5 K for CO(1-0) to 248.9 K for CO(9-8) and higher for even higher transitions according to Equation 3.9. It follows that the temperature of a gas region produces a unique set of transitions lines, known as the J-ladder or spectral line energy distribution, SLED. This is a useful tool for choosing the X-factor and determining other properties of the gas. Starburst galaxies such as

[5] In reality centrifugal forces will change the value of I creating a line width of 10 MHz.

Arp 220 and M82 have peak intensity in for $J_{\text{upper}} \approx 4 - 10$. For AGNs, such NGC 1068 and NGC 6240 the peak intensity is shifted a few levels to higher J-values, and the decline for even higher J_{upper} is less dramatic (Mashian et al., 2015).

In star-forming galaxies, most molecular gas exists in molecular clouds. Conveniently, star formation occurs when denser regions of these cold structures contract due to gravity. Their masses reach up to $10^7\,\mathrm{M}_\odot$. Much smaller structures cannot form stars because UV photons would be able to dissociate the molecules. Photodissociation for H_2 occurs when a photons with $h\nu > 11.2\,\mathrm{eV}$ excites the molecule which subsequently de-exites and produces two separate hydrogen atoms. The probably for a dissociation during the de-exitation is small, but non-negligible. Large enough clouds avoid photodissociation with self-shielding: outer molecules absorb close to all of the incoming UV photons, leaving the inner molecules unaffected.

The CO(3-2) line is considered a good tracer of star formation (see e.g. Greve et al., 2014). It was found by Iono et al. (2009) that the CO(3-2) luminosity correlated over five orders of magnitude with the total FIR luminosity. Moreover, galaxies of different types and epochs maintain a star formation efficiency that is constant up to a factor 2. This line corresponds to the cooling of slightly heated gas and could therefore be seen as a tracer for an early phase of star formation.

3.4.2 High-Redshift Galaxies

Galaxies are identified as distant when their emission is significantly red-shifted. The classical way to decide redshift is by observing a spectrum of lines, identifying the lines from their mutual separation and intensity, and then extrapolating the redshift from that. Problematically, this method of spectroscopic redshift struggles for very faint and angularly small sources. Instead, the photometric redshift was introduced, finding galaxies such as Lyman-break galaxies (LBGs), BzK galaxies and distant red galaxies (DRGs) as well as extremely red objects (EROs). The method is based on the comparison of the relative intensity in several narrow-band filters. Each such difference defines a colour, and they correlate with properties with the galaxy. If most stars in a galaxy formed during some time at some redshift, then these parameters can be used to estimate spectroscopic redshift and stellar population among others (Schneider, 2006, Chapter 9).

The Lyman-break method is based on the absorption of luminosity with frequencies below the Lyman-alpha transition. Photons with shorter wavelength than 912 Å have a larger energy than $E = hc/\lambda = 13.6\,\mathrm{eV}$, which is the ionisation energy of hydrogen atoms. Since the ionisation cross section for hydrogen is large, photons with a λ <912 Å are unlikely to escape galaxies. Equivalently, the energy difference between the ground state and the first excited state for an hydrogen atom is 10.2 eV corresponding to 1216 Å. Photons with 912 Å<λ<1216 Å are absorbed with a probability that is smaller for λ <912 Å, yet still large. Consequently, high-redshift galaxies show a break in the spectrum at $\lambda_{\text{rest}} = 912\,\text{Å}$, which shifts towards 1216 Å for $z > 4$ (Schneider, 2006, subsection 9.1.1). Needless to say, the break is only clearly visible if blue light exists, which means that star formation must be present. If a galaxy is visible in one broad band filter, but not in a filter with shorter wavelength, the break must lie somewhere between these filters. In this way,

the redshift to the galaxies can be found. The series of transitions to the ground state of the hydrogen atom is called the Lyman series (ranging from the Ly-α transition at 1216 Å to the Lyman limit at 912 Å), and therefore galaxies discovered through the Lyman-break method are called Lyman-break galaxies. Alternatively, since the source appears to vanish in low-wavelength filters, Lyman-break galaxies are sometimes called drop-out galaxies.

Three similar multi-band selections are done for the BzK galaxies, DRGs and EROs. The first uses a colour-colour diagram with $B - z$ and $z - K$ to separate old galaxies from star-forming galaxies at $z > 1.4$. Stars, X-ray sources and nearby galaxies are also grouped in this diagram (Daddi et al., 2004). The second technique relates to the previously mentioned 4000 Å break, and identify DRGs. The break is shifted to lie between the J and K filter for $2 \lesssim z \lesssim 4$. Thus, the selection criterion is $J - K > 2.3$. The name comes from the J-band at $z = 2$ corresponding to the B-band, selecting red wavelengths, at $z = 0$. The third type of object is selected from $R - K \gtrsim 5$ and $K \lesssim 20$ (Schneider, 2006; Smail et al., 2002).

From photometric studies, 60 % of LBGs where found to have very strong Ly-α emission (Schneider, 2006, page 470). This made it possible to detect distant galaxies through narrow-band selection. This method is based on the flux ratio being much larger between a Ly-α emitting galaxy and some background if they are observed with a narrow-band filter, as opposed to a wide-band filter, centered at the Ly-α line. Galaxies identified through this method are titled Ly-α emitters and they are usually much fainter than LBGs.

The very specific observational techniques create unfortunate biases. Dusty galaxies can be faint in the NIR and shorter wavelengths. The Lyα line is redshifted out of the optical window for $z \gtrsim 7$. This makes spectroscopic confirmation difficult. In general, since distant galaxies are increasingly faint only the brightest sources can be observed. This means that two selection criteria are broadly applied to very distant galaxies ($z \gtrsim 3$). First, observed galaxies are very luminous. Second, galaxies whose light has converged through the gravity of some object along the line of sight can appear magnified. This process is known as gravitational lensing and is the topic of Section 6.3.

3.4.3 Star Formation Rate

Star formation is studied mainly in five different wavelength regions: Lyman continuum, UV, NUV, U-band (~ 360 nm), and IR. The most massive stars are most visible in UV. IR wavelengths are better probes for DSFGs. In Lyman continuum emission recombination lines of ionised hydrogen in star-forming regions is shown. A simulation by Boquien et al. (2014 showed that while the Lyman continuum method estimates the star-forming well, the remaining methods overestimate the SFR with 25 to 65 %, with U-band measurements scoring the worst. One reason, accounting for a ~ 10 % error, for such overestimations is that many stars live longer than the assumed 100 Myr in the typical models. Therefore isolated galaxies should be modelled with significantly longer ages for stars than starburst galaxies. Another reason is that photons that ionise or heat could come from other sources, e.g. from an AGN, instead of the newly born stars, as assumed.

The principle behind these observations is simply that the SFR for a given galaxy type is proportional to the luminosity in a specific wavelength

$$\mathrm{SFR}_\lambda = C_\lambda L_\lambda \, \mathrm{M}_\odot \mathrm{yr}^{-1}. \tag{3.12}$$

The value and unit of the proportionality constant depend on the applicable frequency region. For instance, for radio emission $\nu = 1.4\,\mathrm{GHz}$ and $1/C_{1.4\,\mathrm{GHz}} \approx 8.4 \times 10^{27}\,\mathrm{M}_\odot\,\mathrm{yr}^{-1}\,\mathrm{erg\,s}^{-1}\,\mathrm{Hz}^{-1}$. This relation between the SFR and radio emission is a consequence of the correlation between the radio luminosity of a galaxy and its FIR luminosity. In the FIR, the relation assumes that all star formation is dust enshrouded, meaning that all energetic photons are absorbed by dust and re-radiated thermally (Madau and Dickinson, 2014; Schneider, 2006; Cimatti et al., 2019).

Without specifing any more constants (the interested reader may use e.g. section 9.6.1 in Schneider, 2006), three more relations, of the same type, should be mentioned. Firstly, Hα emission traces the HII regions around massive ($M \gtrsim 10\,\mathrm{M}_\odot$) hot, young stars. Since the recombination timescale is extremely short ($\sim 10^3\,\mathrm{yr}$), such emission is only present during star formation. Similarly to FIR, the SFR-relation for Hα assumes every local high-energy photon is produced by the stars and end up ionise hydrogen in their surroundings (to produce the HII region). These photons are have $\lambda < 912\,\text{Å}$ and are called *Lyman continuum photons*. Given an initial mass distribution of the stars, the SFR can be calculated from the Lyman continuum photons. Secondly, UV radiation produces a relation based on O/B stars that assumes that neither AGNs nor dust attenuation is present. Models of dust and the unobscured spectral shape of stellar emission suggests that SFR should actually be corrected by a factor of ~ 5, unless the FIR relation is added in the calculation of the SFR.[6] Thirdly, X-ray luminosity can relate emission from binaries and massive stars to the SFR.

Finally, the SFR can also be inferred from the $\lambda = 157.7\,\mu\mathrm{m}$ line and SEDs. The emission line comes fom ionised carbon. Therefore its detection signifies cooling of dense molecular clouds, which is an early step in star formation. Regarding SEDs, best-fits can give parameters in stellar population synthesis models that, given a star formation history, yields the SFR for the galaxy.

3.5 Gravitational Lensing

General references: (Sparke and Gallagher, 2007, section 7.4), (Schneider, 2006), (Cimatti et al., 2019, subsection 5.3.4)

The emission of distant galaxies are often attracted by the gravity of foreground galaxies, groups or clusters, causing the source to appear magnified and distorted. This process, known as gravitational lensing, is therefore an important tool for observers of distant galaxies.

How light is affected by gravity is thoroughly explained in Einstein's general theory of relativity. His famous $E = mc^2$ introduces a mass-energy duality which suggests that every chunk of energy interacts with gravity. By expressing time

[6] Of course, larger dust absorptions cause deviations form the proportionality between $\mathrm{SFR}_{\mathrm{FIR}}$ and $\mathrm{SFR}_{\mathrm{UV}}$.

as another dimension to add to the spatial dimensions, the principle of general covariance[7] represents gravity not as a force travelling on spacetime, but as the bending of spacetime itself. The straight light ray can now appear to bend when following a geodesic.[8]

Classically, the deflection angle for a particle with mass m interacting with an astronomical body of mass M is found by intergrating Newton's second law $F_\perp = M\frac{dv_\perp}{dt}$ over time and applying the small angle approximation

$$\Delta v_\perp = \frac{1}{M}\int_\infty^\infty F_\perp(t)\mathrm{d}t = \frac{1}{M}\int_\infty^\infty \frac{GmMb}{(b^2+v^2t^2)^{3/2}}\mathrm{d}t = \frac{2GM}{bv} \Rightarrow \alpha_{clas} = \frac{2GM}{bv^2}, \tag{3.13}$$

where G is Newton's constant and b is the closest approach to the astronomical body. Relativistic interpretations lead to a relativistic deflection angle, called Einstein's deflection angle that is twice the classical:

$$\alpha_{\mathrm{rel}} = \frac{4GM}{bc^2}. \tag{3.14}$$

For small angles and circularly symmetric, small lenses I can re-express this. The thin lens approximation models the lens on a lens plane. Similarly, thin sources can be considered lying on a source plane. With Figure 3.1, I introduce the reduced deflection angle $\alpha_{\mathrm{red}} = \alpha_{\mathrm{rel}} D_{LS}/D_{OS}$ together with the new angles $\beta \approx y/D_{OS}$ and $\theta \approx x/D_{OS}$, where D_{ij} are the angular diameter distances along the optical axis between object i and j. The lens equation is just the reformulation of Equation 3.14:

$$\alpha_{\mathrm{red}} = \theta - \beta = \frac{4GM}{c^2}\frac{D_{LS}}{D_{OS}D_{OL}}\frac{1}{\theta} = \frac{\theta_{\mathrm{E}}^2}{\theta}, \tag{3.15}$$

where the final step introduced the Einstein angle. Additionally, the Einstein radius, which is the characteristic radius for an Einstein ring, is the product between this angle and the distance to the lens $r_{\mathrm{E}} = \theta_{\mathrm{E}} D_{OL}$. The lens equation is quadratic[9], $\theta^2 - \beta\theta - \theta_{\mathrm{E}}^2 = 0$, with the Einstein angle being the characteristic angle. As a consequence, any source is, if the lensing is strong enough, imaged twice on opposite sides of the source. If the lens lies directly in front of the source merge into a circle known as an Einstein ring.

For lenses with a non-zero angular extension, Equation 3.15 should be updated with a surface density Σ instead of M:

$$\alpha_{\mathrm{red}} = \frac{4G}{bc^2}\int \Sigma(r) 2\pi r \mathrm{d}r, \tag{3.16}$$

where $\Sigma(r)\mathrm{d}r^2 = \mathrm{dM}$.

[7] This statement, that physical laws transform covariantly, is just the sum of the general principle of relativity (identical equations of motions in all coordinate systems), and the principle of equivalence (gravity is locally indistinguishable from inertial forces).

[8] This is the shortest line between two points on a surface.

[9] I can multiply with θ because the extension of lens is non-singular.

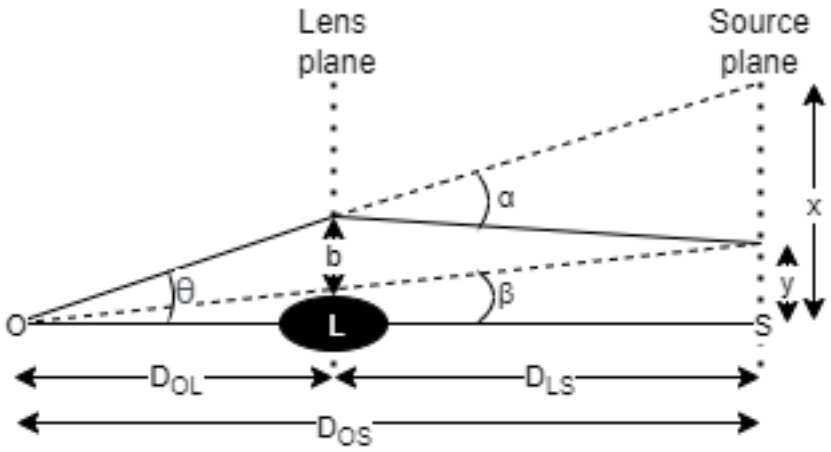

Figure 3.1: Schematic illustration of one light ray being subject to gravitational lensing. All lines in the figure are purely used as trigonometrical tools.

Under the assumption that the lens is axisymmetric, the projected mass $M(<b)$ should replace M. This is the mass that is projected within the circle with radius b equal to the distance of closest approach between the light ray and the lens. In this case, the lens Equation 3.15 can be rewritten as

$$\alpha_{\rm red} = \frac{M(<b)/(\pi b^2)}{\Sigma_{crit}} \frac{1}{\theta}. \tag{3.17}$$

in terms of the critical surface mass density

$$\Sigma_{\rm crit} \equiv \frac{c^2 D_{OS}}{4\pi G D_{OL} D_{LS}} = \frac{M(<r_{\rm E})}{\pi r_{\rm E}^2} = \frac{M(<\theta_{\rm E})}{\pi (D_{OL}\theta_{\rm E})^2}. \tag{3.18}$$

If the surface mass density exceeds Σ_{crit} anywhere on the lens, then the lensing is strong and multiple images are produced.

Einstein enclosed masses are determined from the lens Equation 3.15 when $\beta = 0$. In terms of the critical surface mass density this independent mass estimate can be derived to be

$$M(\theta_{\rm E}) = \pi \Sigma_{crit} (D_{OL}\theta_{\rm E})^2 = \frac{c^2 D_{OS} D_{OL} \theta_{\rm E}^2}{4 G D_{LS}} \tag{3.19}$$

This equation follows from the last part of Equation 3.18.

Gravitational lensing is divided into three categories. Strong lensing is described above and portrayed in Figure 3.2. Weak lensing produces only one image, that is somewhat distorted and relocated. Microlensing apparently only affects the observed brightness. The three strengths generally results from distant galaxies or black holes, cosmic shear due to the general mass distributions in the Universe, and studies of dark matter within the Galaxy, respectively.

The stronger the gravitational lensing is, the closer the observed arc is to a circle. This arc is light from different angles of the source. Since the surface brightness is left unchanged by gravitational lensing, the magnification equals the

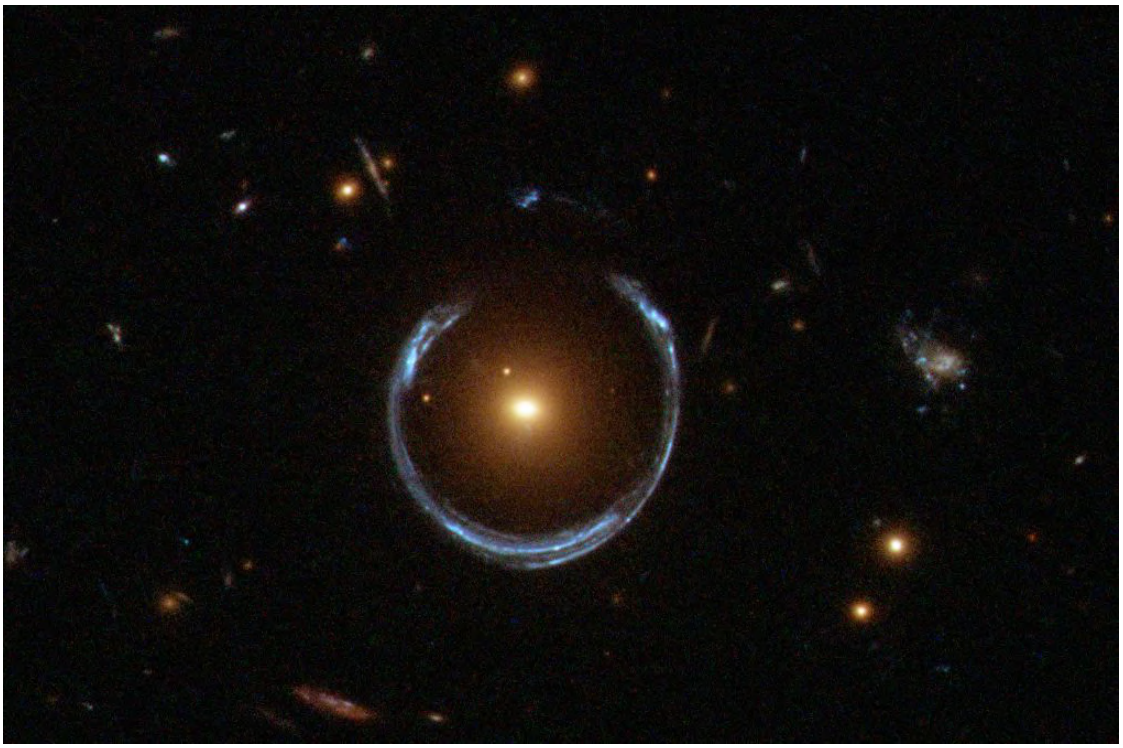

Figure 3.2: A distant blue galaxy that lies almost exactly behind a luminous red giant. Its light bends into the shape of a horseshoe. Credit: ESA/Hubble & NASA.

increase in apparent brightness which is

$$\mu = \left| \det \left(\frac{\partial \beta}{\partial \theta} \right) \right|^{-1} \approx \frac{\theta/\theta_{\mathrm{E}}}{\theta/\theta_{\mathrm{E}} - 1}. \tag{3.20}$$

This can be heuristically derivated with Figure 3.1 and the following identities: $\mu = x\mathrm{d}x/(y\mathrm{d}y) = \theta\mathrm{d}\theta/(\beta\mathrm{d}\beta) \approx \theta/\theta_{\mathrm{E}}/((\theta/\theta_{\mathrm{E}})-1)$. The plot showing the magnification at each position on the lens plane is called the *magnification map*. For emission nearly centered behind the lens $\beta \ll 1$, or equivalently $\theta \approx \theta_{\mathrm{E}}$, and the magnification is very large. The lines marking the positions of diverging magnification is called *critical lines*. Regions separated by critical lines show different parity: they either increase or decrease in apparent size. Tracing the critical lines back to the source plane produces lines called *caustics*. These lines separate regions that produce a different number of images. This number is typically three or five.

When operating as lenses, spiral galaxies have been shown to be modelled well as singular isothermal ellipsoids (SIEs) (Koopmans et al., 2006, 2009; Hezaveh et al., 2013). Analytical simplifactions are often done under the special case of the SIE being a singular isothermal sphere (SIS). These have density profiles and projected surface mass distributions

$$\rho_{\mathrm{SIS}}(r) = \frac{\sigma_v^2}{2\pi G r^2} \overset{3.16}{\Longrightarrow} \Sigma_{\mathrm{SIS}}(r) = \frac{\sigma_v^2}{2Gr}, \tag{3.21}$$

where σ_v is the one-dimensional isotropic velocity dispersion for stars. Besides being a simple model, this is motivated by the rotation curve of spiral galaxies being flat.

The singularity for $r \to 0$ as well as the divergence of the total mass must be dealt with by changing the inner mass profile and severing the extension for large r. With Equation 3.16 the relativistic deflection angle becomes

$$\alpha_{\text{rel}}^{\text{SIS}} = 4\pi \left(\frac{\sigma_v}{c}\right)^2 \left(\frac{D_{LS}}{D_{OS}}\right) \equiv \theta_{\text{E}}^{\text{SIS}}, \tag{3.22}$$

where the final step is the definition for the Einstein angle for singular isothermal spheres. For $\beta < \theta_{\text{E}}$ the two images are separated by $2\theta_{\text{E}}$.

Models and tools for gravitational lensing depend on a range of parameters for both source and lens. Obviously, the plane positions and redshifts, or — more precisely — the angular distance, of both has to be known. This finds D_{OL}, D_{OS} and D_{LS}. Depending on the type of surface profile of the source different parameters are used. Some examples of surface profiles are Gaussian, point source, and Sérsic profile (Schneider, 2006, equation 3.39),

$$I(r) = I_{\text{e}} \exp\left(b_n \left[\left(\frac{r}{r_{\text{e}}}\right)^{\frac{1}{n}} - 1\right]\right), \tag{3.23}$$

where $b_n \approx 1.999n - 0.327$, r_{e} and I_{e} are the effective radius and corresponding intensity, and n is a number called *index*. A Sérsic profile is therefore parametrised by n, I_{e} and r_{e}, as well as the ratio of the semi major and semi minor axes. A lens that is modelled as an SIE is parametrised by its ellipticity, position angle and mass, which — in the case of strong lensing — can be calculated from Equation 3.19. In some cases the magnitude and angle of the external shear, from e.g. the gravitational field of neighbouring galaxies, can be included in the model too.

3.6 Principles of Interferometric Imaging

General references: (Cortes et al., 2020, Chapter 3)(Condon and Ransom, 2018, section 3.7)
An interferometer is an interconnected configuration of antennas. It can be thought of as a very large non-parabolic antenna with empty space between patches of antenna surface. Just like the different parts of the wave front that strikes different area elements of the single dish antenna can interfere constructively or destructively, different wave front parts will hit different antennas in the configuration, at different times, which produces independent signals that can interfere constructively or destructively when they merge in the so-called correlator.

Thus, the collecting area plays an equivalent role as for the single dish antenna. The total, effective antenna surface area is proportional to the sensitivity: more collecting area allows for detection of fainter sources. The largest distance between two antennas in the configuration determines the angular resolution:

$$\theta_{\text{res}} \propto \frac{\lambda}{L_{\text{max}}}. \tag{3.24}$$

A way to specify this relation is by introducing the half power beam width (HPBW). Using this for the left hand side, the proportionality constant becomes 1.13 for ALMA (Cortes et al., 2020, figure 3.3).

The improved angular resolution is the central motivation for interferometry: $L_{\max}$ can be much larger than for a single dish antenna. The largest single dish antenna is the five hundred meter large, fixed FAST in China (Nan et al., 2011). ALMA has baselines, distances between antennas, up to 16.2 km.[10] More extreme, VLBI - a technique for connecting different observatories together - have produced baselines in the *European VLBI Network* that span more or less the diameter of the Earth (Booth, 1991). With the same technique used in space the baseline lengths can be even longer (see e.g (Lazio et al., 2020)).

An apparently similar relation holds for shorter baselines. The maximum recoverable scale is defined as

$$\theta_{\text{mrs}} \propto \frac{\lambda}{L_{\min}}. \tag{3.25}$$

A larger maximum recoverable scale produces contrasts for larger angular structures. To observe both small and large scale structures it is therefore desirable that the antennas constituting an interferometer are placed in way creating a combination of short and long baselines. This relation follows from the fact that the baseline L between two antennas determines what scale the detected emission of this baseline is sensitive to. The cross correlation can only produce constructive interference for signals with fixed phase differences. Thus, each projected relative distance corresponds to one spatial frequency.

To model this, the, by the wave front, projected plane of the interferometer is called the *uv*-plane[11] (see part a and b of Figure 3.3). In contrast, for the celestial sphere, or image plane, *xy*-coordinates are adopted. An interferometer with N antennas produces $N(N-1)/2$ baselines that are represented as $N(N-1)/2$ points in the *uv*-plane, called visibilities. The collection of such dots produce a *uv*-coverage, which can be improved by increasing the observation time since the rotation of Earth changes the projection of the baselines (see part c of Figure 3.3). This is known as Earth rotation synthesis. The *uv*-coverage is limited by the zero spacing problem: all distances smaller than an antenna diameter are unsampled.[12] This also limits the maximum recoverable scale. Mathematically, the momentary *uv*-coverage is the autocorrelation of the projected antenna configuration minus the zero sampling.

The visibilities contain information on the amplitude of a cross correlated signal, and the phase difference of its components. This interferometer response is known as a fringe, where the fringe spacing $1/u$ (in radians) is simply the inverse of the projected distance u (see Figure 3.4). Thus, the brightness and relative celestial position of a target source can be inferred from this. An image is produced from the visibilities by cross correlating all baselines. This is often called aperture synthesis, and the *uv*-plane is therefore sometimes referred to as the aperture plane.

Two antennas, separated by a distance d, that measure the same source, at some angle β over the horizon, will be separated by a geometric delay $d\cos\beta$ in their received signal, see Figure 3.4. This is compensated for by an artificial delay in the

[10] `https://www.almaobservatory.org/en/factsheet/`.

[11] The direction of propagation is then said to be in the negative w direction.

[12] The severity of the zero spacing problem is reduced by using an additional configuration of smaller telescopes, or observations with single-dish telescopes.

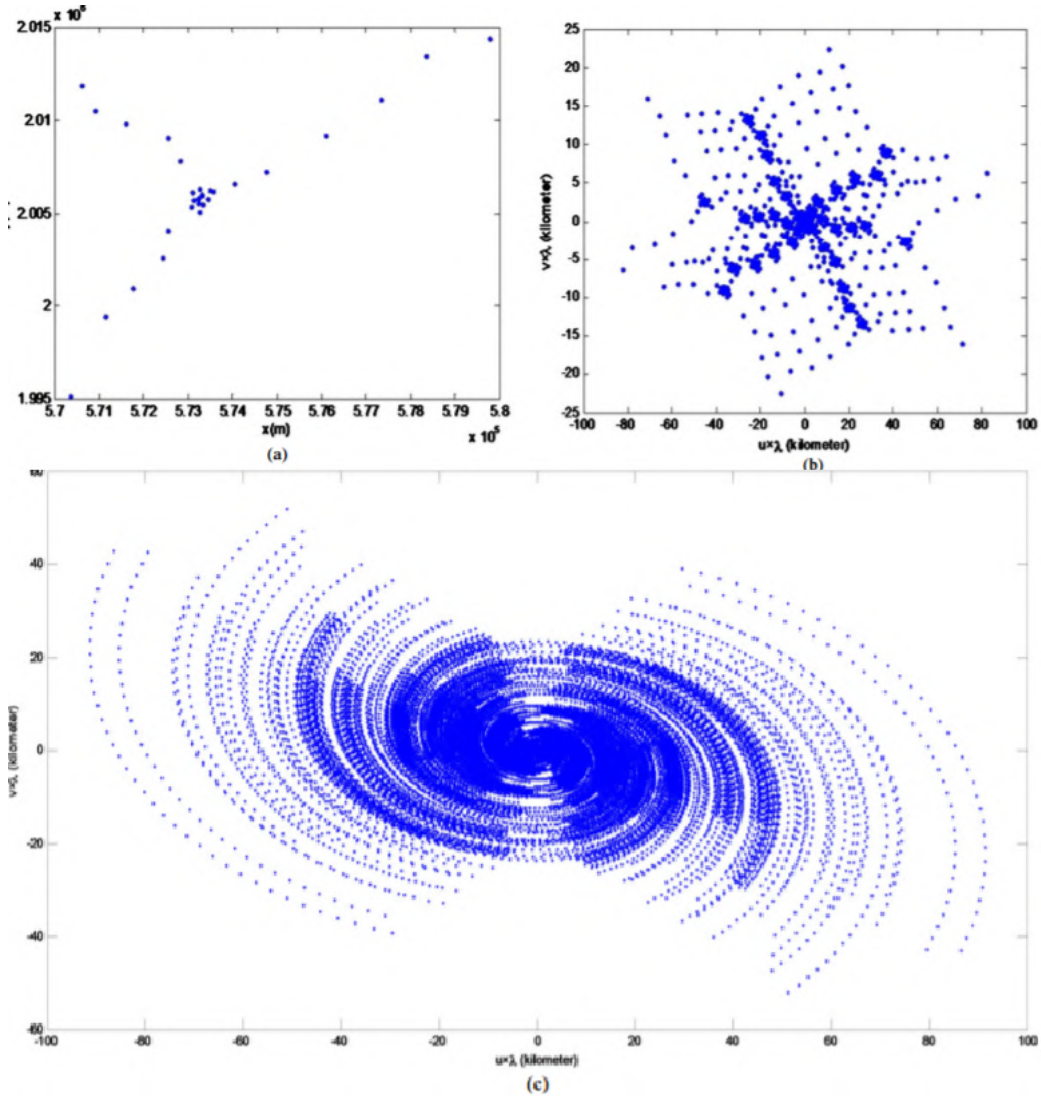

Figure 3.3: Process of obtaining *uv*-coverage. (a) Antenna configuration of the *Giant Metrewave Radio Telescope*, (b) *uv*-snapshot, (c) *uv*-coverage after one hour of tracking. Credit: (Kiehbadroudinezhad et al., 2014, edited).

receivers. If the telescope points slightly off source, an additional phase delay will be introduced. In the projected two dimensional *uv*-plane this can be modelled as $e^{2\pi i(ul+vk)}$ for projected distances l, k in the *uv*-plane. The phase center is defined as the location where $l = k = 0$.

The visibility for one antenna pair m, n depends on the source brightness I and the relative phase shift $e^{2\pi i(ul+vk)}$ of the antennas. A correlator is an imaging device that produces the complex visibility by multiplying and time-averaging the two signals of any antenna pair.

$$\mathcal{V}(u,v) = \int\int I(l,k)e^{2\pi i(ul+vk)}\mathrm{d}l\mathrm{d}k. \tag{3.26}$$

This is the van Cittert-Zernike theorem (see e.g. Thompson et al., 2017). Notice that the right hand side is the inverse Fourier transform of the brightness distribution.

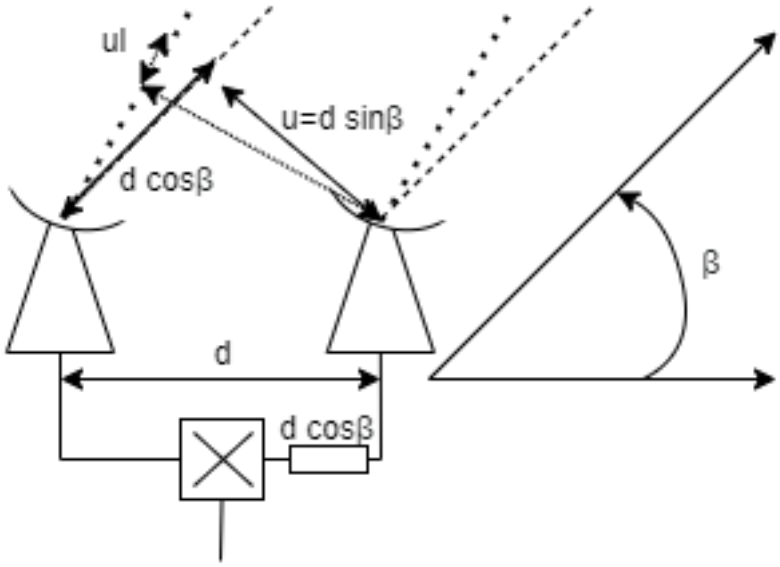

Figure 3.4: Schematic and one-dimensional illustration of phases and the *uv*-plane, given two antennas in an interferometer. One calculation of a u-coordinate in the *uv*-plane, a geometric delay and an off-source delay are symbolically included. The coordinate l can be calculated much like the geometric delay, given an off-source angle.

The complex visibility is a measurement of spatial coherence of the signal and is therefore also called the cross-spectrum.

Solving for the brightness distribution in Equation 3.26, an image is made by Fourier transforming the combined visibilities. Due to the discrete nature of computers, the visibilities must be placed in pixels and weighted against each other. Three common weightings are:[13]

- **Natural weighting** is inversely proportional to the noise variance. This emphasises shorter baselines for improved sensitivity
- **Uniform weighting** is inversely proportional to the sampling density. This emphasises longer baselines to obtain smaller side lobes of the beam
- **Briggs weighting** which uses a robust parameter to customise a mixture between the two above. This parameter spans values between -2, uniform weighting, and +2, for natural weighting.

There are, however, two meaningful corrections to the process of Fourier transforming the complex visibility to obtain an image. Firstly, since only some *uv* points are sampled, a sampling function $B(u, v)$, describing the *uv*-coverage, will contribute to the image. Adding this factor to the left hand side of Equation 3.26, it defines the dirty image instead of the brightness distribution. The Fourier transform of $B(u, v)$ is called the point spread function, or dirty beam. Secondly, the brightness distribution $I(l, k)$ in Equation 3.26 also depends (linearly) on the power response of the primary beam $\mathcal{A}(l, k)$. This sensitivity function is usually an Airy function. If the observed object is larger than the central Gaussian of the dirty beam, called the

[13] `https://lweb.cfa.harvard.edu/sma/miriad/manuals/SMAuguide/smauserhtml/node107.html`.

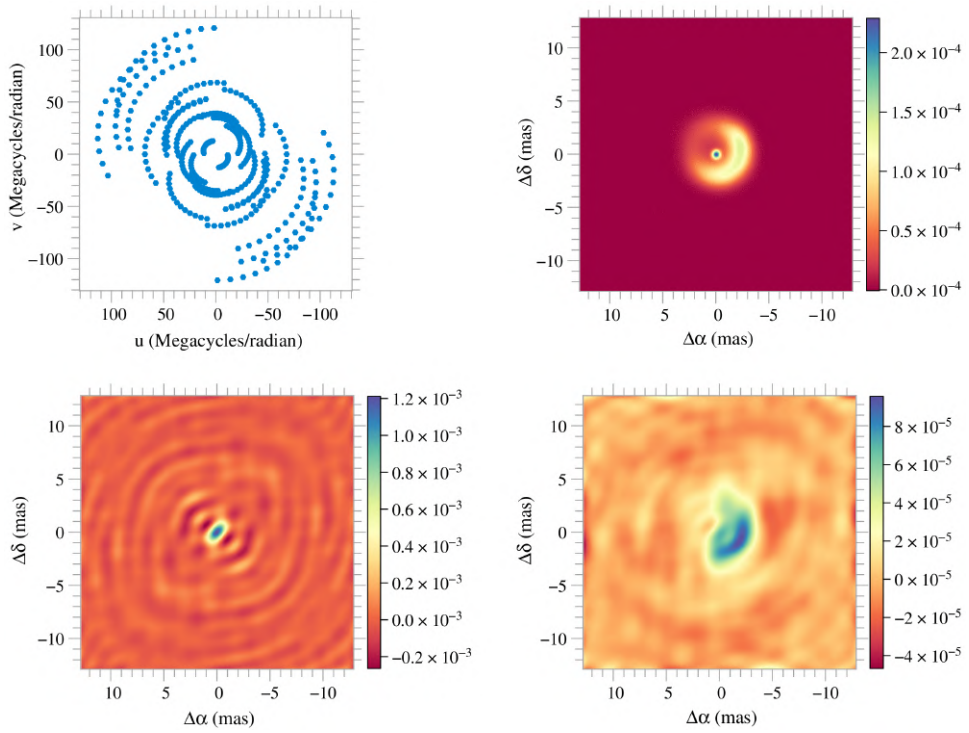

Figure 3.5: The interferometric process of imaging. Top left: *uv*-coverage from the *Navy Prototype Optical Interferometer*. Top right: representation of the true image, in this case a model of the LkHa-101 cluster. Bottom left: dirty beam or the Fourier transform of the *uv*-coverage. Bottom right: dirty image or the Fourier transform of the complex visibility. This is also obtained by convoluting the dirty beam with the true image (times the power response). Credit: (Thiébaut and Young, 2017, figure 2). The top two images are from (Monnier et al., 2014).

synthesised beam, an image must therefore be divided by this Airy function in the final so-called primary beam correction, to create the true brightness distribution. Correcting Equation 3.26, the dirty image I_d is the convolution of the dirty beam b_d and the brightness distribution times the power response of one antenna (see Figure 3.5):

$$I_d = b_d * I\mathcal{A}. \tag{3.27}$$

In order to find the true brightness distribution, the dirty beam of Equation 3.27 must be deconvolved. Unfortunately, deconvolution cannot produce any unique solution because the *uv*-coverage only measures some discrete spatial frequencies. The best procedure is then to simply guess some criteria of the true brightness distribution to enable inference of it. One widely used deconvolution algorithm is CLEAN. It assumes that the true brightness consists of a finite number of point sources producing Gaussians. The true image is then reconstructed by subtracting dirty beams with center in the peaks of the dirty image from this. This is done in many iterations, until the highest peak are close to the noise level. The fraction of the peak that is removed in each iteration is called the loop gain. The subtracted peaks are finally replaced with Gaussians. The region in which peaks are identified

is selected with a mask. One popular version of CLEAN is created by Högbom and models the sky as a collection of delta-functions.[14]

3.7 ALMA

There are many interferometers in the world, observing different sky positions at different frequencies and with different sensitivities. Some have been mentioned in Section 1.3. This thesis uses data from the Atacama Large Millimeter/submillimeter Array (ALMA) for which operating statistics are specified in Table 3.1. Situated on a 5100 m altitude plateau in the Atacama desert in Chile, ALMA saw first light in 2011, but obtained its full number of antennas three years later, see Figure 3.6. The ALMA project is a cooperation between North America, Europe, East Asia and Chile (Schneider, 2006, page 23).

ALMA consists of one large array with 54 12 m antennas, and one fixed, small array, called Atacama Compact Array, ARA, with twelve 7 m antennas to improve the maximum recoverable scale.[15] These produce baselines between 15 m and 16.2 km which gives an angular resolution down to 0.005" at 950 GHz (Cortes et al., 2020).[16] Two giant transporters move the antennas into different configurations.

One challenge for submillimeter antennas are that their surfaces must be very exact. ALMA's antenna surfaces are precise down to 25 µm[17] Furthermore, the position of the telescopes are measured with distant quasars to millimeter precision.

Table 3.1: Basic statistics of ALMA from `https://almascience.nrao.edu/about-alma/alma-basics`.

Frequencies	Channel width	Resolution	Field of view[18]	Typical PWV
84-950 GHz	3.8 kHz-15.6 MHz	0.02-0.5"	50"	1 mm

3.7.1 Science

General reference: (Testi, 2010)[19]
Since radio astronomy covers a wide range of phenomena the scientific applications of ALMA range from studies of atmospheres in the solar system to detection of the most distant ($z > 7$) objects. As of today, ALMA has eight receiver bands[20] that observe in frequencies from 85 to 950 GHz, and therefore are used for different purposes. Two more bands are planned, to extend the observable frequencies down to 35 GHz. For a detailed presentation of the science goals of ALMA, see (Bachiller and Cernicharo Quintanilla, 2008).

[14] `https://casa.nrao.edu/casadocs/casa-5.1.1/synthesis-imaging/deconvolution-algorithms`.
[15] `https://www.almaobservatory.org/en/factsheet/`.
[16] `https://public.nrao.edu/telescopes/alma/`.
[17] `https://www.eso.org/public/sweden/teles-instr/alma/antennas/`.
[19] And `https://public.nrao.edu/telescopes/alma/`.
[20] `https://www.eso.org/public/sweden/teles-instr/alma/receiver-bands/`.

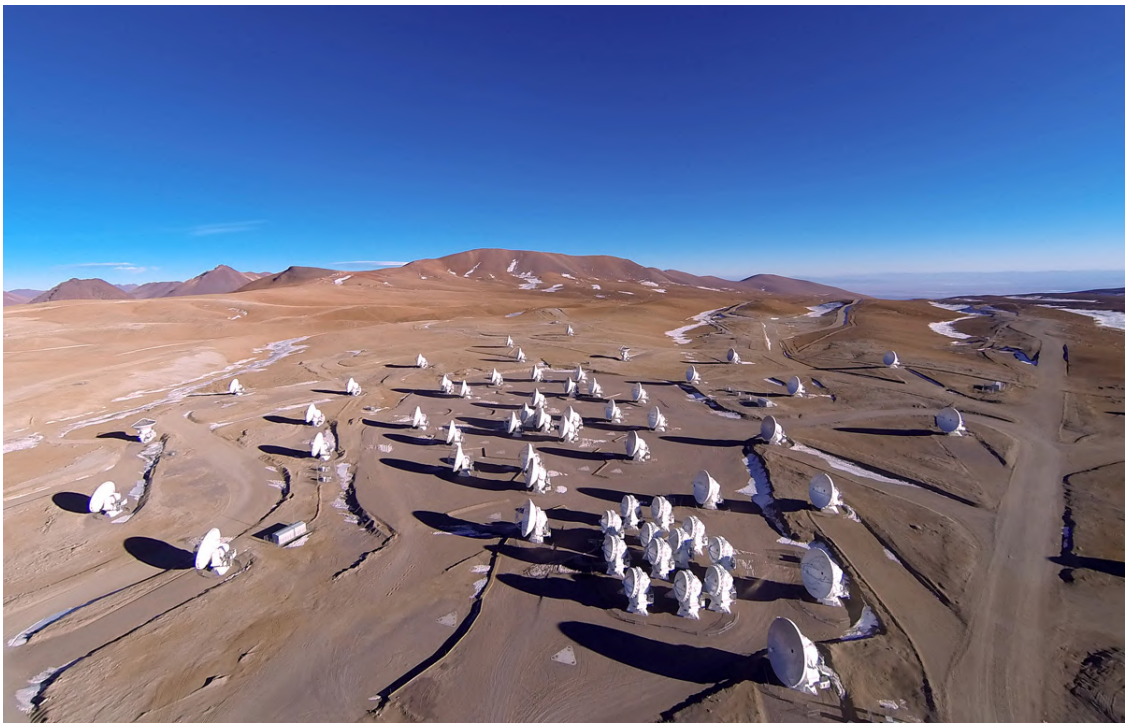

Figure 3.6: Atacama Large Millimeter/submillimeter Array in June 2014, closely after the arrival of the final antenna. Credit: Ariel Marinkovic / X-Cam.

In our solar system, the high angular resolution of ALMA enables detection of small or distant asteroids and comets. Atmospheres and even gas from volcanoes on celestial bodies can be observed too. In particular, the chromosphere of the sun and the solar wind are two ideal usages of ALMA.

Within the local Universe, ALMA can study stellar envelopes and planetary nebulae. Since radio emission is generally emitted thermally by gas and dust, ALMA can be used in the local Universe to map gas and dust with high resolution and study star and planet formation. Specific applications include astrochemistry, early stages in stellar formation, and evolved stars.

High-redshift objects, like the first galaxies and stars in the Universe can be resolved with ALMA's high angular resolution for the millimeter-sized wavelengths. Many distant galaxies have an AGN and some are classified as radio galaxies. These are especially easy to study with ALMA thanks to their high luminosity in radio frequencies. This thesis will make use of band 3 of ALMA to study the CO(3-2) line in two distant galaxies and map the molecular gas as an attempt to better understand star formation in high-redshift galaxies.

3.7.2 Calibration

General reference: (Cortes et al., 2020, Chapter 7)
The success of imaging with a telescope rests on considerations of the source, telescope and the path in between. Atmospheric attenuation and scattering, and antenna and receiver imperfections are adapted for in the process of calibration. ALMA differentiates between observatory calibrations and execution block calibrations.

Observatory calibrations are done outside the PI science observations. Some of these steps are done regularly on the observatory, and independently of any one project, to ensure that the collected data will be comprehensible and useful. Examples of such calibrations are the creation of the desired antenna primary beam pattern, measurement of antenna surface irregularities, and updating for new array configurations. Other steps are done for each measurement and include finding the peak sensitivity of the antenna beam and tilting and moving the subreflectors to direct reflected emission towards the feed.

Execution block calibrations are specific for each measurement and are only viewed in detail by the researchers who use the data. One step measures the system temperature by a 15 s scan of a hot load, ambient load and the sky. Another measures the water vapor, or the PWV, with water vapor radiometers because humidity causes phase delay variations. In the bandpass calibration, a very bright, stable point source (generally a quasar) is observed to measure the relative amplitude and phase in the frequency channel in each spectral window. The flux density scale produces the scale factor used in the conversion between antenna temperature and received flux. To do this, a source of known brightness (often the same as the bandpass calibrator) is observed. Differential heating of antennas could, during daylight hours produce amplitude variations up to 10 % for this scale factor. These temporal gain variations can be estimated with the amplitude solution of the phase referencing calibration, in which the phase correction for the elevation of the source is determined. This calibrator should be a point source close to the science target. The phase calibration is one of the most important calibrations for good imaging and is usually done last. It finds the phase correction for each antenna, spectral window and polarisation and interpolates this with help of previous execution block scans. Constellations with some baselines longer than 5 km (or ν >400 GHz) include a slightly less luminous but still nearby check source to estimate the image quality.

To satisfy these calibration demands the execution time for the telescope will be spent first on pointing calibration, then observing the bandpass calibrator followed by an alternation of the phase calibrator, check source (if necessary) and science target. Simultaneously a radiometer measures the precipitable water vapor. Measured data is ran through a pipeline in the python-based Common Astronomy Software Application (CASA) and presented in a weblog that is optimised the Firefox browser. This allows for a clear view of the calibration, which I will describe in Section 4.2.

4
Methodology

In this thesis, two distant, gravitationally lensed galaxies were studied in four steps. First, and long before my participation in this project, data were acquired using ALMA. Second, the data were calibrated using CASA and specifically designed scripts for this purpose. Third, imaging was done with an interactive CASA script. Fourth, a model for gravitational lensing was applied to the galaxies with another python-based program called `visilens`. Throughout this work, I assume a flat ΛCDM cosmology with $H_0 = 67.7\,\mathrm{km\,s^{-1}\,Mpc^{-1}}$, $\Omega_\mathrm{M} = 0.307$ and $\Omega_\Lambda = 0.693$ (Planck Collaboration and Ade, 2016).

4.1 ALMA Observations

The observations of this thesis were taken as a part of a project aimed at studying star-forming galaxies at $z = 2 - 3$ and to characterise their super-giant molecular clouds. The project PI is G. Drouart and the project code is 2016.1.01231.S. The IAU identity of the sources, which were found in millimeter surveys with the SPT (Carlstrom et al., 2011), are SPT-S J012506-4723.7 and SPT-S J213403-5013.4. For convenience, their short names that are presented in Table 4.1 will be used throughout this thesis.

Observations were carried out on the 21st and 25th of September 2017 with the ALMA 12-metre array. The science target was the CO(3-2) ($\nu_\mathrm{rest} = 345.795\,989\,90\,\mathrm{GHz}$) transition for SPT0125-47 and SPT2134-50. They were observed in band 3 (covering 84-116 GHz) and configuration C40-8/9 during cycle 4. During the observations, the time t_obs was spent alternating between calibrators for pointing and focus, flux and bandpass, phase, the check source, and the science target. During observations of calibrators the ALMA water vapor radiometer system collected data too. The observations are summarised in Table 4.2. Flux and bandpass calibrations were done with bright quasars: J2357-5311 for SPT0125-47 and J2056-4714 for SPT2134-50. Phase calibration was done using the calibrators J0124-5113 and J2125-4948, and

Table 4.1: Positional information of the observed SPT galaxies.

Short name	IAU name	R.A. (J2000)	Dec. (J2000)	z^a
SPT0125-47	SPT-S J012506-4723.7	01:25:07.03	-47.23.56.2	2.5148
SPT2134-50	SPT-S J213403-5013.4	21:34:03.34	-50:13:25.1	2.7799

[a] Redshifts for both sources are given in (Weiß, 2013). The redshift for SPT2134-50 was confirmed in Strandet et al. (2016).

Table 4.2: Observational information of the SPT galaxies. The nomenclature of the left column are for the observation time including calibration (t_{obs}), time spent on science target (t_{on}), precipitable water vapor (PWV), number of antennas (N_{ant}), longest and shortest baseline (L_{max} and L_{min}), expected line frequency of observation ($\nu_{\mathrm{CO(3-2)}}$), minimum recoverable scale (θ_{res}), maximum recoverable scale (θ_{mrs}), primary beam angular size (θ_{pb}), number of channels (N_{ch}), centre frequency (ν_{c}), and channel width ($\delta\nu_{\mathrm{ch}}$).

Source	SPT0125-47	SPT2134-50
Observing date (ISO 8601)	2017-09-21	2017-09-25
Time for observation (UT)	05:19:45-05:41:44	02:10:01-02:44:06
t_{obs} (min:s)	16:09	24:26
t_{on} (min:s)	5:08	10:17
PWV (mm)	2.32	0.56
N_{ant}	42	40
L_{max} (km)	12.1	14.9
L_{min} (m)	41.4	41.4
$\nu_{\mathrm{CO(3-2)}}$ (GHz)	98.51321	91.50110
θ_{res} (")	0.06	0.05
θ_{mrs} (")	9	10
θ_{pb} (")	53	57
Science spectral window		
Synthesized beam size[a] (mas×mas)	94×82	127×107
Position angle[a] (deg.)	23	66
N_{ch}	480	480
ν_{c} (GHz)	98.4727	91.4953
$\delta\nu_{\mathrm{ch}}$ (MHz)	3.9064	3.9064

[a] This is the result of using Briggs weighting with a robust parameter of 0.5.

the check sources were J0133-4430 and J2135-5006 for the respective science target.

4.2 Calibration

The data were calibrated with CASA version 4.7.2 (McMullin et al., 2007). The calibration was checked by comparing calculated values with catalogued values for the calibrator targets and noting data that was particularly deviant and not explainable by phenomena that had already been noticed and accepted in previous measurements.

The calibration review was done with the collection of webpages that is the pipeline weblog. In it 32 tasks are listed and assigned a specific quality assurance (QA) score between 0 and 1, to allow for a quick check of which steps of the calibration have gone smooth and which have not. The final fifteen steps of these concern imaging. I will not go through all steps here, but summarise their general structure. First, the data was imported. The first tasks summarises the flagging. Subsequent tasks summarise calibrations for antenna positions, system temperature, water vapor

and individual antenna gains. Summaries include a QA score, flagging notifications and graphs whenever applicable. The bandpass, phase, and check source calibration finalised the calibration task list by showing that the graphs depicting amplitude or phase versus frequency or time are stable and reasonable for all channels in each spectral window. Flagged or particularly deviant data were, for convenience, noted in a text file together with the calculated gain and important information that is presented in this chapter.

4.3 Imaging

After calibration by CASA's pipeline, an independent eight-step CASA (version 5.6.2-3) imaging script controlled the imaging. In the first step, specific antenna or spectral windows could be flagged and skipped. Neither source needed any flagging beyond what the pipeline already had done. Second, the script provided information about observational parameters, including focus for each antenna at different times and characteristics of four unique spectral windows. Third, splitting the data and regridding from topocentric to the conventional LSRK frame of reference was done. Only the target observation with the on-source intent and the relevant spectral windows were kept. For SPT0125-47 this included two spectral windows with 128 channels and channel width $\delta\nu_{\mathrm{ch}} = 15.625\,\mathrm{MHz}$ and central frequencies $\nu_{\mathrm{c}} = 96.5147\,\mathrm{GHz}$ and $\nu_{\mathrm{c}} = 108.5147\,\mathrm{GHz}$, and one science spectral window that is described in Table 4.2. For SPT2134-50 there were three 128 channel wide spectral windows included with central frequencies $\nu_{\mathrm{c}} = 93.4329\,\mathrm{GHz}$, $\nu_{\mathrm{c}} = 103.4961\,\mathrm{GHz}$ and $\nu_{\mathrm{c}} = 105.4963\,\mathrm{GHz}$, apart from the science spectral window. The corresponding channel widths for non-science spectral windows were $\delta\nu_{\mathrm{ch}} = 15.6261\,\mathrm{MHz}$.

With the relevant data organised, imaging proceeded by using the CLEAN algorithm. All cleaning steps required a mask - a region in which the cleaning was done. This mask was initially a circle around the phase centre. With the CASA viewer this was updated manually with slightly improved accuracy.

Spectral windows were cleaned first. In channel mode, all spectral windows were cleaned with Briggs' weighting using a robust parameter of 0.5, to best compromise between the SNR and angular resolution. Thresholds of the size of 3σ were applied, corresponding to 7.02 mJy for the spectrum with 480 channels of SPT0125-47, and 4.05 mJy for the same of SPT2134-50. Half of these values (3.51 mJy and 2.025 mJy) where used for the 128 channel wide spectral windows. The result was a data cube for each spectral window with estimates of the true intensity on a two dimensional map for different frequencies.

Next, the source continuum was cleaned. To do so, manual identification of the line emission was performed with the CASA viewer. All channels except those containing line emission were combined into just one channel - the continuum. This cleaning was done once with the same Briggs weighting with a robust factor of 0.5 and once using natural weighting. A 2σ threshold of $7 \times 10^{-2}\,\mathrm{mJy}$ for both weightings for SPT0125-47.[1] For SPT2134-50, the 2σ proved not deep enough by checking the residuals. Therefore a 1σ threshold of $2.46 \times 10^{-2}\,\mathrm{mJy}$ for the Briggs weight-

[1]This much smaller threshold comes from the continuum effectively being one very wide channel.

ing and 2.18×10^{-2} mJy for the natural weighting was applied. Cleaned continuum emission was subtracted from the visibilities to change the mean value for the detected non-target emission to zero, and thereby distinguishing the line emission.

Data from the final two steps were used as heuristic tools to estimate the spectral and spatial structure of the sources. This motivated the selection of linewidth and mask regions for the python scripts that produced the figures in Chapter 5. The first of these two steps started by changing the spectral resolution by combining channels into larger bins. These bins were specified in quantities of radio velocity. Therefore this step is said to operate in *velocity mode*. Several updated resolutions (4, 10, 20, 50 $\mathrm{km\,s^{-1}}$) were tested. For each resolution the cleaning was done for with 1σ thresholds found from the CASA viewer. This was done both with natural weighting and with Briggs weighting.

Lastly, moment-0 maps were created by integrating over all channels containing the line. Once again, a 1σ threshold of 5.7×10^{-4}, 5.0×10^{-4} and 0.27 $\mathrm{mJy\,beam^{-1}}$ for SPT0125-47, and 0.53, 0.37 and 0.24 $\mathrm{mJy\,beam^{-1}}$ for SPT2134-50, was used for velocity bins of size 10, 20 and 50 $\mathrm{km\,s^{-1}}$. Following the completion of these steps, the final moment-0 maps, created over the estimated full line, were compared to the used masks. To optimise the line intensity estimation used in these imaging steps, all steps were done again with a newer and more exact mask for SPT2134-50. No significant change resulted. Since the original mask proved to be more exact for SPT0125-47, no new mask was created for this source. I must clarify that the purpose of these eight steps was to clean the data and extract the source structure. The moment maps that are presented in this thesis were created from another method described below.

The emission line data presented in this thesis comes from Briggs-weighted images, with a robust parameter of 0.5, of the spectral window containing the CO line. For comparison, the spectra were extracted from natural-weighted data as well. The only clear change these spectra was a very slight decrease in the noise level. This indicates no loss of extended emission within the scales probed by the interferometric data.

For each source, line emission was extracted from an annulus-shaped region, because already obtained moment-0 maps in CASA had shown that both sources had a ring-like structure. The annulus was specified by its central coordinates (x_c, y_c) and inner and outer radii r_i, r_o. These are presented in Table 4.3. The values were obtained by comparing the extracted region with the structure of the source from the already obtained moment-0 maps. These annuli are visualised in the presentation of the moment-1 maps. The spectra are binned in velocity bins of $(1+z)10\,\mathrm{km\,s^{-1}}$ to easier distinguish the line from the noise. In the axis of abscissas a conversion between frequency and radio velocities were done with the formula $\Delta\lambda/\lambda = v/c$ or $\nu = \nu_{\mathrm{rest}}(1 - \frac{v}{c})$, where λ and ν are observed wavelengths and frequencies. Moment maps were created, using the FWHMs obtained from fitting a Gaussian profile to the obtained spectra.

The spectral line profiles were fitted using two different functions, a Gaussian profile and a skewed Gaussian profile. The Gaussian fit was done using a Levenberg-Marquardt algorithm (Moré, 1978) that was implemented through `astropy`. The

Table 4.3: Parameters for annuli masks when creating the spectra in Figure 5.3.

Source	(x_c, y_c) =(hourangle, deg) [ICRS]	r_i (mas)	r_o (mas)
SPT0125-47	(01:25:07.030,-47:23:56.26)	714	1377
SPT2134-50	(21:34:03.352,-50:13:24.93)	357	714

skewed Gaussian was defined near the central velocity as

$$\begin{cases} (x - v_{\text{start}}) a \exp[-\frac{(x-c)^2}{2d^2}] & \text{where } v_{\text{start}} < v < v_{\text{stop}} \\ 0 & \text{where } v < v_{\text{start}} \text{ or } v > v_{\text{stop}} \end{cases}, \tag{4.1}$$

where $v_{\text{start}} = -280\,\text{km}\,\text{s}^{-1}$ for SPT0125-47 and $-550\,\text{km}\,\text{s}^{-1}$ for SPT2134-50. The upper limit, v_{stop} ($600\,\text{km}\,\text{s}^{-1}$ and $700\,\text{km}\,\text{s}^{-1}$ respectively) was higher than half of the linewidth. Larger ranges resulted in skewed Gaussians that were nearly identical to the normal Gaussians, and smaller ranges resulted in the lines of the skewed Gaussians being jagged. The skewed Gaussians were fitted with the curve fit tool in `scipy` (Virtanen et al., 2020).

4.4 Lens Modelling

A python-based programmed called `visilens` was used to model the gravitational lensing (see Hezaveh et al., 2013; Spilker et al., 2016). `visilens` constructs models directly from the interferometric visibilities of ALMA instead of the resulting images. Therefore, no additional noise is added from the cleaning; interferometric images all points, and therefore also noise, are correlated. `visilens` can therefore account for, for example, residual calibration uncertainties and biases, and thus the resulting uncertainty estimates can be more accurate.

In essence, `visilens` models the *uv*-data with parameters describing the source and lens. Luminosity profiles for the sources are of one of three types: Sérsic profiles, two-dimensional Gaussians, and point sources. A Sérsic source is parametrised by its major axis a, Sérsic index n (see Equation 3.23), axis ratio a/b, position angle PA_S east of north (see Section B) for the major axis, observed average flux density over the line (for this thesis $S_{\text{CO(3-2)}}$), and sky coordinates relative to the lens x_{off} and y_{off}. The lenses can only be modelled as SIEs (see Equation 3.21) with sky coordinates x_L and y_L relative to the phase centre, mass M_L, ellipticity e_L, and position angle PA_L as free parameters. A shear can also be introduced and specified by its magnitude and position angle. Free parameters are fitted with a Markov Chain Monte Carlo (MCMC) method using Metropolis–Hastings sampling and applied with `emcee` code (Foreman-Mackey et al., 2013). Loose, flat priors are generally used. Drawbacks with `visilens` include not printing critical lines, and not being able to reconstruct the source, channel for channel.

In this thesis, the sources were assumed to have a surface brightness distribution well described by a Sérsic profile, specified by the previously mentioned parameters. As the introduction of a shear component did not create any visible improvement of the models, no shear was used when creating the results that are presented in this thesis. Images from `visilens` were obtained by ray-tracing the

flux from the source around the simulated lens. Good models for the source and lens could then be identified by comparing dirty images with `visilens` images including their relative noise levels.

The regions of the flat priors, as well as the number of walkers, steps, and other functional parameters varied depending on the source and what portion of the CO(3-2) was being inspected.[2] Values from Spilker et al. (2016) were used as initial guesses for both sources. The higher resolution ($\sim$0.05″) in the ALMA data used in this thesis allowed for and required refinement of these models. After acceptable models had been obtained for the entire lines, samplings were run with smaller frequency bins. The lines were divided once in two portions, with the the flux density peak as the dividing line, and once in five equally wide bins. In these simulations only the source parameters were allowed to vary. The one exception to this was the 98.30 GHz bin for SPT0125-47 for which no acceptable source model could recreate the line structure.

Noise levels were calculated in three ways. First, `visilens` allowed for estimations directly from the *uv*-data. Second, the standard deviation was taken of the northern-most 10 % of the dirty image. This is hereafter called *dirty image RMS* or *image* σ. Third, RMS of the residuals was calculated by taking the standard deviation of the entire residual image, where the residual image was the difference between the dirty image and the `visilens` model. Due to their separate importance (see Chapter 5) all of these values are presented in Appendix A.

[2]For entire emission lines 300 walkers, burn-ins and regular steps were used. For subregions, or bins, this number was reduced to 100 in the interest of time however the results converged to a good fit without needing an increased number of walkers, burn-ins, and regular steps. Resulting parameter values changed only after the first, often second, significant digit. Four cores were used for all samplings.

5
Results

This chapter presents the obtained results. First, in Section 5.1 the observational results for SPT0125-47 and SPT2134-50 are given. Second, Section 5.2 introduces source and lens models obtained from simulations of gravitational lensing.

5.1 Observational Results

In Figure 5.1 the moment-0 maps of SPT0125-47 and SPT2134-50 are shown. Both sources show partial Einstein rings that are characteristic of strong gravitational lensing. The Einstein ring-like structure of the first source has an observed angular radius of $\sim$1.0″, while it is $\sim$0.5″ for the second. Both of these value lie within the range of typical Einstein radii ($\sim 0.2 - 1.2''$; see e.g. Spilker et al., 2016). To show both sources clearly, SPT2134-50 is more zoomed in. This is communicated by showing the size of the synthesized beam in the bottom-left corner of each image.

Figure 5.2 presents moment-1 maps of both sources, with the same resolution and coordinates as in Figure 5.1. While normally the moment-1 shows the data for regions with intensity above some sigma threshold, I here show the moment-1 results using an annulus. The reason for this is the fact that the CO(3-2) emission is fairly resolved. The colour scale is chosen to represent the relative motion of the gas, such that red indicates redshifted motion, and blue indicates blueshifted motion compared to the systemic velocity. The clearest structures in the figure are the top-left and bottom-right parts of the circle for SPT0125-47. This is strong indication of a velocity gradient, which could be interpreted as a rotation — something that I will return to in Chapter 6. In contrast to SPT0125-47, SPT2134-50 is visible in the moment-1 map, without extreme noise, in almost the entire area in which it is visible in its moment-0 map. This area contains less sudden changes in integrated velocities and no larger regions of neither positive nor negative integrated velocities relative to the centre velocity of the source.

Figure 5.3 shows the CO(3-2) spectra for both sources. The spectra were extracted from the data cube with Briggs weighting and from the region of the annuli used in Figure 5.2, the spectra of both sources were obtained. Yellow steps show the average flux density obtained with robust weighting. The velocity axis is centred around the radio velocity that corresponds to the previously known redshifts. RMS noise was calculated from a large rectangular region of the data cube that did not contain the source. The results of a Gaussian profile, as well as a skewed Gaussian profile, fit to the spectra are shown in magenta and blue, respectively. Parameters of the fit are specified in Table 5.1. The assumed redshifts (of Table 4.2) and zero-

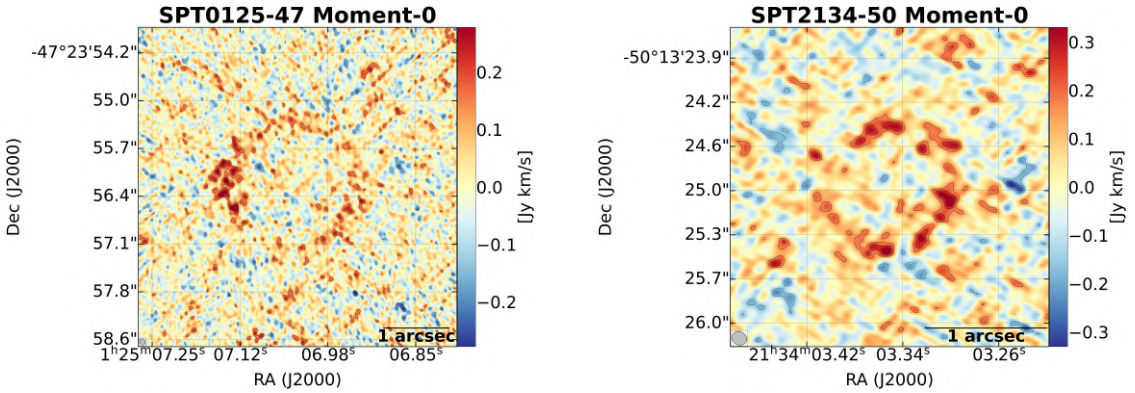

Figure 5.1: Moment-0 maps of SPT0125-47 (left) and SPT2134-50 (right) in ICRS coordinates. The bottom-left corner illustrates the beam size. Contour lines are drawn at $\pm 2\sigma, 3\sigma, 4\sigma$.

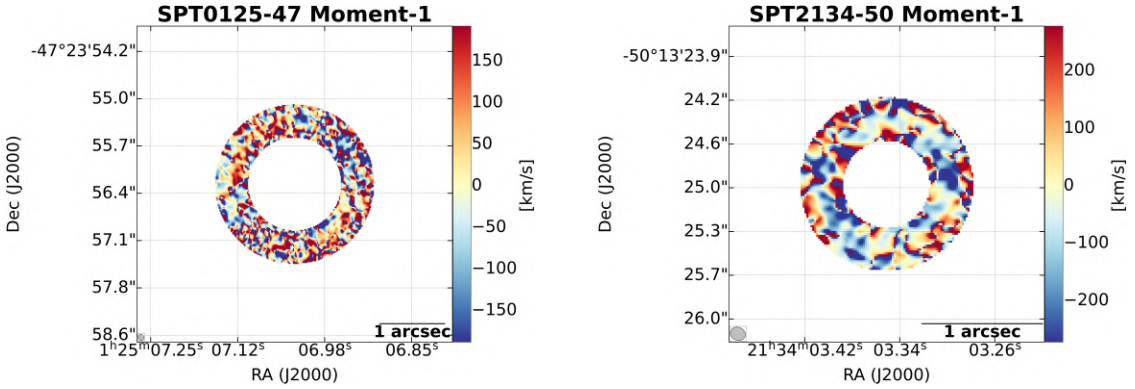

Figure 5.2: Moment-1 maps of SPT0125-47 (left) and SPT2134-50 (right) in ICRS coordinates. The bottom-left corner illustrates the beam size.

velocity point is aligned with the peak of the normal Gaussian.

The properties of the line could be derived from the Gaussian fit. The velocity-integrated line intensity was calculated from $I_{\mathrm{CO(3-2)}} = 1.065 S_{\mathrm{peak}} \Delta v_{\mathrm{FWHM}}$, where S_{peak} is the amplitude of the Gaussian in Jy and Δv_{FWHM} is the full width half maximum in $\mathrm{km\,s^{-1}}$, which applies to all Gaussian functions. The line luminosity is calculated from Equation (3.10) and (3.11) based on the estimated $I_{\mathrm{CO(3-2)}}$.

5.2 Gravitational Lens Models

For both sources, all emission belonging to the CO(3-2) line were summed to a single channel. The lens and source models were then fitted to this aggregated data using `visilens`. The results are presented in Figure 5.4 with coordinates relative to the phase centre in units of arcsecond. Each row contains five panels that demonstrate the models obtained for the specific source and frequency bin. The first panel shows the dirty image of the input visibility data using natural weighting. Specifically, the image is obtained by summing all visibilities after inverting them individually. The

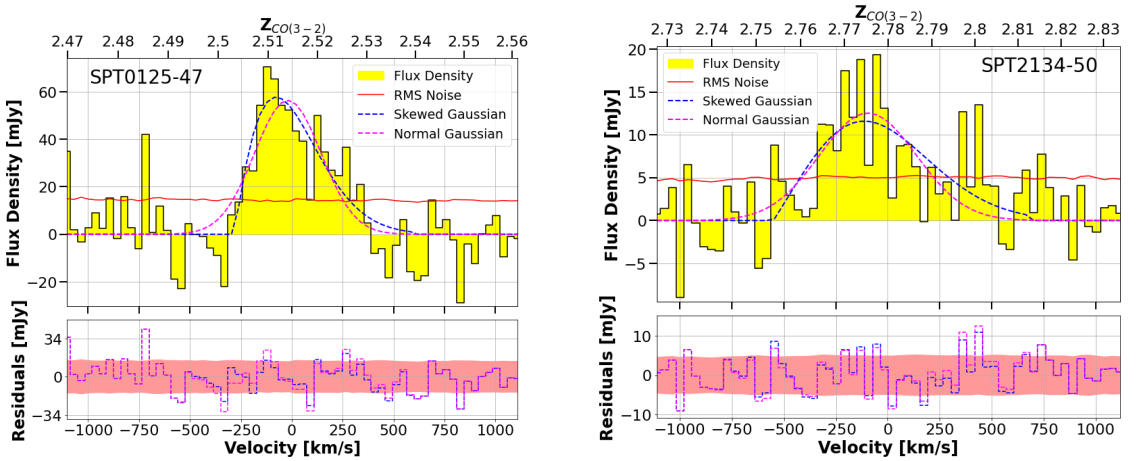

Figure 5.3: *Top row:* The CO(3-2) spectra of SPT0125−47 (left) and SPT2134−50 (right). The dashed lines show the resulting fitted Gaussian (magenta) and skewed Gaussian (blue) line profiles. The 1σ RMS noise is shown by the red line. *Bottom row:* The residuals from the two line profile fits. The pink coloured regions indicates the 1σ RMS. For both rows, the zero velocity corresponds to the assumed redshifts (of Table 4.2).

second panel is the dirty image that is calculated from the *uv*-distribution by ray tracing in `visilens` . Corresponding residuals are shown in the third panel. The final two panels model the emission in the image and source planes, with caustics.[1]

Two values for σ are attached to each row. For the dirty image, the RMS noise is calculated from the rectangular region that spans the northern-most 10 % of the image. It is this value that determines the contour lines. The σ value for the residuals are calculated from the entire 512 × 512-pixels image. Since the residual image is the difference between the dirty image and the `visilens` model, the noise value can actually be larger in the residuals than in the dirty image background. For instance, a peak in the background of the dirty image can be partly cancelled by a peak in the background of the `visilens` model and yield a value closer to zero in the residual image. Such a peak can be produced by the synthesised beam function. An alternative way to compare the noise level, which resolves this problem, is replacing the dirty image RMS with the `visilens` RMS that is calculated directly from the *uv*-data. Since the `visilens` RMS includes all of the data and not just the data that is commensurate with the northern-most 10 % of the image, the estimated dirty image RMS can still be smaller than the `visilens` RMS due to noise fluctuations. The `visilens` RMS is a more correct estimate of the actual noise, and is therefore included in Appendix A. However, the problem with this approach is that no equivalent method exists for the estimation of the noise of the residuals, and so the comparison with the latter would be less relevant.

Both SPT0125-47 and SPT2134-50 could be modeled with high accuracy using `visilens` . Residual RMS for both sources increased only 2.1 % and 1.6 % in

[1]Note that while caustic curves have their connotation in the source plane and critical lines lie in the image plane, `visilens` produces caustics only.

Table 5.1: Direct parameters of the fitted curves. The central velocity is the velocity corresponding to the peak of the fitted curves. The bottom three rows presents line properties that are calculated from the observed spectral features. Note that the luminosity is not intrinsic to the source, since the magnification factor μ is kept.

Source	SPT0125-47		SPT2134-50	
Gaussian	Normal	Skewed	Normal	Skewed
Amplitude (mJy)	56 ± 6.0	58 ± 16	13 ± 1.7	12 ± 2.5
Central[a] frequency (GHz)	98.39±0.054	98.41±0.015	91.51±0.071	91.52±0.085
Central[a] redshift	2.5146±0.0019	2.5138±0.0019	2.7787±0.0029	2.7783 ± 0.0035
FWHM ($\mathrm{km\,s^{-1}}$)	380 ± 47	390 ± 290	550 ± 87	650 ± 290
$I_{\mathrm{CO(3-2)}}$ ($\mathrm{Jy\,km\,s^{-1}}$)	23 ± 3.8	24 ± 19	7.3 ± 1.5	8.1 ± 4.0
$\mu L_{\mathrm{CO(3-2)}}$ ($10^8\,\mathrm{L_\odot}$)	10 ± 1.7	11 ± 8.7	3.9 ± 0.82	4.3 ± 2.1
$\mu L'_{\mathrm{CO(3-2)}}$ ($10^{11}\mathrm{K\,km\,s^{-1}\,pc^2}$)	7.9 ± 1.3	8.2 ± 6.5	3.0 ± 0.62	3.3 ± 1.6

[a] This is actually the frequency corresponding to the peak flux, a distinction that is important for the skewed Gaussian. The median frequencies were calculated as well, yielding 98.39±0.054 GHz for SPT0125-47 and 91.50±0.079 GHz for SPT2134-50. The corresponding redshifts are 2.5146±0.0019 and 2.7792 ± 0.0032, respectively.

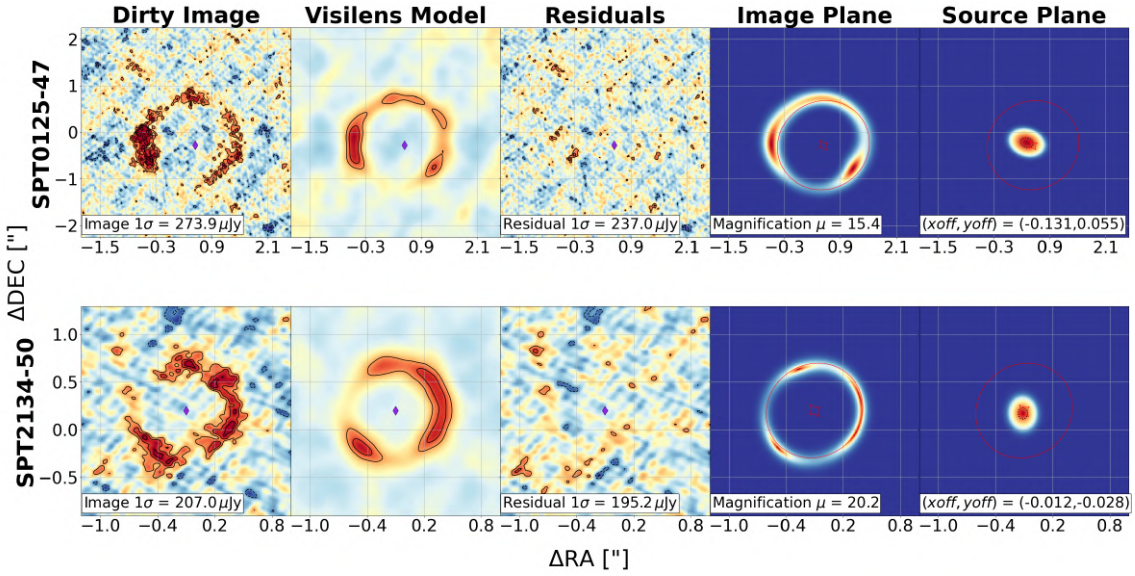

Figure 5.4: Lens models for both SPT sources. The first two columns show, respectively, a non-cleaned, approximately naturally weighted image, and the calculated version of this given the simulated properties of the lenses and sources. The third column is the difference between these two images. Recreated intensity distributions in the image and source plane are presented in the fourth and fifth columns. Critical lines and caustics are shown in red. Black contour lines are drawn at $\pm 2\sigma, 3\sigma, 4\sigma$. Purple diamonds show the position of the centre of the lens.

Table 5.2: Lens parameters.

Source	SPT0125-47	SPT2134-50
z^a	0.305	0.776
x_L (")	0.539 ± 0.012	-0.101 ± 0.009
y_L (")	-0.275 ± 0.013	0.202 ± 0.012
M ($10^{11}\,\mathrm{M}_\odot$)	1.415 ± 0.021	0.887 ± 0.023
e_L	0.166 ± 0.019	0.203 ± 0.039
PA_L (deg)	32 ± 3	37 ± 2

[a] Lens redshifts are given in K. M. Rotermund (et al., in preparation).

Table 5.3: Fitted source parameters. Note that the flux density $S_{\mathrm{CO(3-2)}}$ is the average across the included channels and not peak value of the line. Similarly, the magnification μ is the average over the total source emission.

Source	SPT0125-47	SPT2134-50
x_off (")	-0.131 ± 0.008	-0.012 ± 0.004
y_off (")	0.055 ± 0.007	-0.028 ± 0.007
$S_{\mathrm{CO(3-2)}}$ (mJy)	2.673 ± 0.243	0.583 ± 0.093
n_S	0.617 ± 0.155	0.928 ± 0.165
a_S (")	0.140 ± 0.010	0.059 ± 0.009
$b_\mathrm{S}/a_\mathrm{S}$	0.741 ± 0.045	0.837 ± 0.091
PA_S (deg)	162 ± 7	20 ± 3
μ	15.4 ± 0.9	20.2 ± 2.9

comparison to the `visilens` RMS, respectively. Both sources show clear Einstein ring-like structures indicating that the source lies almost directly behind the lens in both cases. SPT0125-47 shows a relatively high emission in the eastern parts of the ring. An important finding of this analysis was that a good lensing model for SPT0125-47 could be created using a single source rather than the three necessary in Spilker et al. (2016). The implications of this are discussed in Section 6.3.4.

Fitted parameters of the foreground galaxies that causes the gravitational lensing magnification are shown in Table 5.2. Fitted source parameters are presented in Table 5.3. To easier reproduce the model these parameters are specified with more significant digits than can be motivated from the certainty of the method.

One parameter to be skeptical about is the mass of the lens. From the fitted masses of Table 5.2, effective Einstein angles can be calculated with Equation (3.19). The corresponding angular radii are $0.98 \pm 0.014''$ and $0.50 \pm 0.013''$. These values are slightly smaller than the approximations based on obtained moment-0 maps. Effective Einstein angles from (Spilker et al., 2016) are, with the same equation, equivalent to $M_{\mathrm{SPT0125-47}} = 1.52 \pm 0.01 \times 10^{11}\,\mathrm{M}_\odot$ and $M_{\mathrm{SPT2134-50}} = 0.94 \pm 0.01 \times 10^{11}\,\mathrm{M}_\odot$. This is $\sim$7 % and $\sim$6 % higher than what has been obtained in this thesis, indicating a larger uncertainty than what has been presented in Table 5.2 and 5.3.

After the full line emission had been modelled with `visilens` , the same procedure was done for subsets of the emission line. The line was split into bins

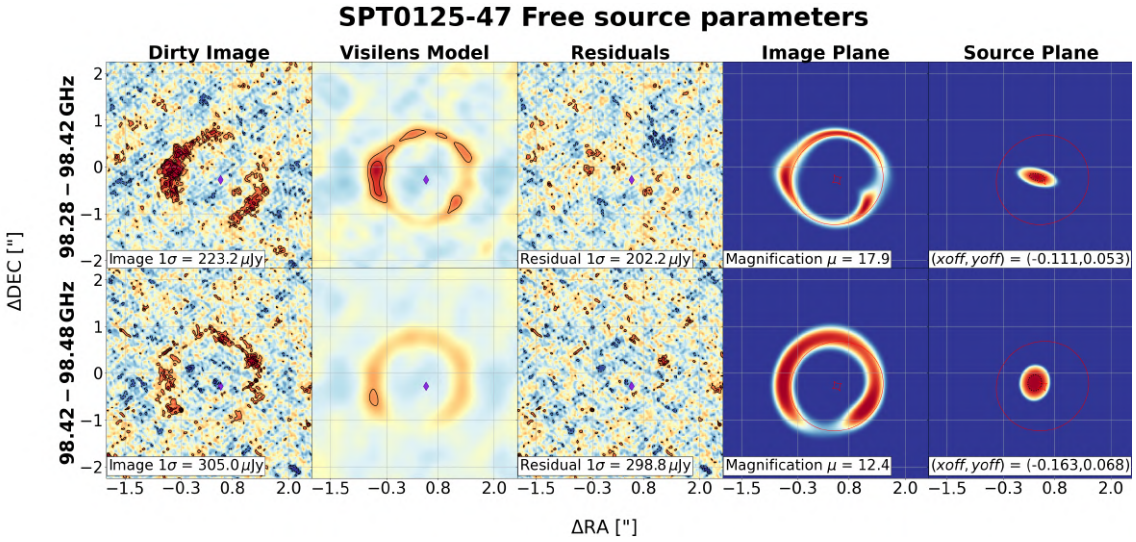

Figure 5.5: Gravitational lensing models for five bins of SPT0125-47. In each bin the source parameters are free to vary, and in the first row, also the lens was fitted.

for each source, to investigate possible velocity profiles. Since the mass distribution of the foreground galaxy, and therefore all of the lens parameters, are frequency independent only the source parameters were allowed to vary in these MCMC samplings. Figure 5.5 and 5.6 show in total seven frequency bins for which the source parameters were fitted to the already obtained lens parameters and the frequency-binned dirty images of SPT0125-47. Figure 5.7 and 5.8 serve the same function for SPT2134-50. By only varying the source position and flux, very similar results were obtained (see Appendix A.3). The frequency bins are centralised around the specified values with widths of 0.04 GHz for SPT0125-47 and 0.06 GHz for SPT2134-50, unless specified otherwise. This width was choosen to cover the entire line in five channels. The remaining two channels, for each source, covers each side of the peak flux. In this way, the two wider bins can display what parts of the Einstein ring-like structures moves away or towards the observer. Additionally, the five, smaller bins can estimate how much different parts are moving radially.

To recreate the image of the 98.30 GHz frequency bin of SPT0125-47 the lens parameters had to vary. In Appendix A.3 the result for a fixed lens in this frequency bin is presented. Similar problems are present to a lesser degree in the 98.34 GHz and 98.46 GHz frequency bins of the same source. This can partially be explained by the fact that the lens model was fitted over just $\sim 98.33 - 98.44$ GHz which means that parts of the data in these bins did not affect the estimated lens parameters.

In Table 5.4 and 5.5 the fitted source parameters for different frequency bins of SPT0125-47 and SPT2134-50, respectively, are presented.

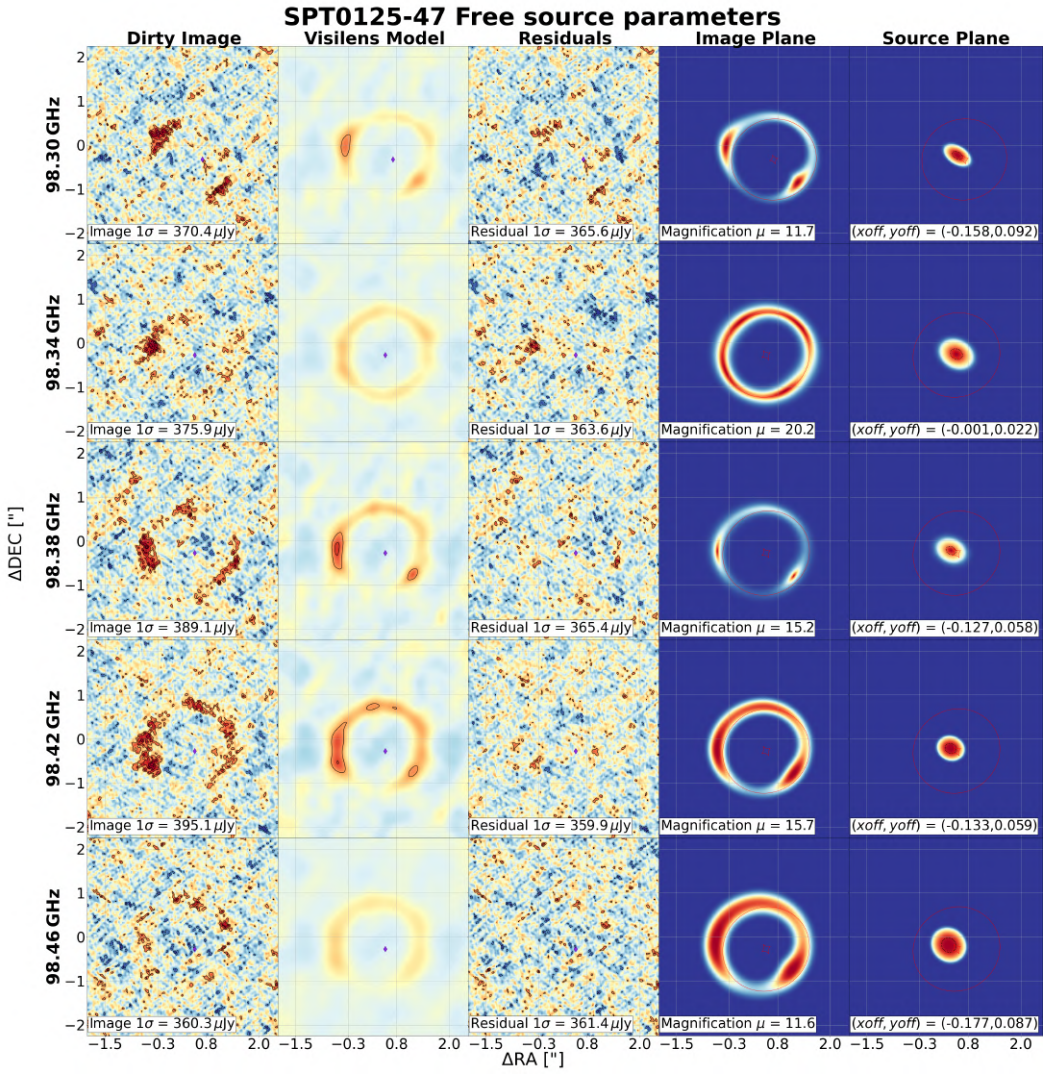

Figure 5.6: Gravitational lensing models for five bins of SPT0125-47.

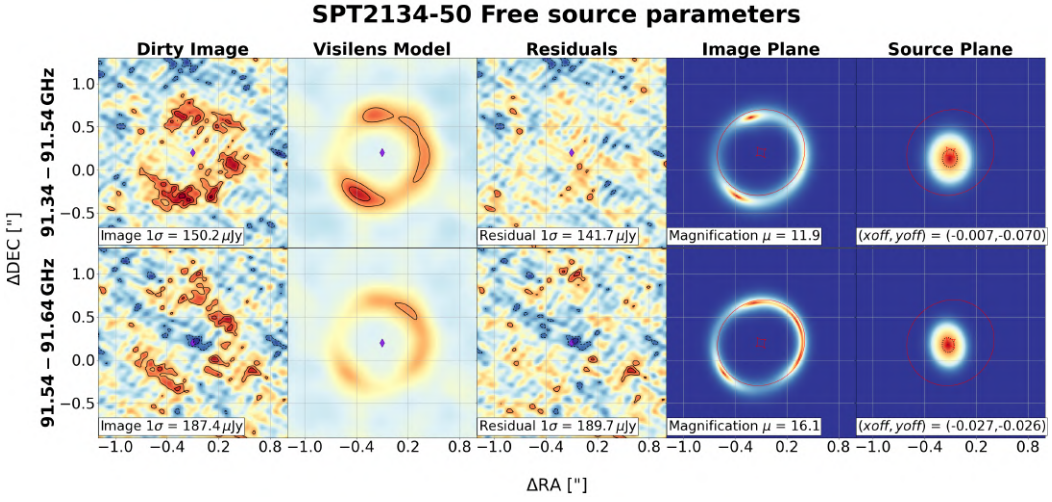

Figure 5.7: Gravitational lensing models for two bins of SPT2134-50.

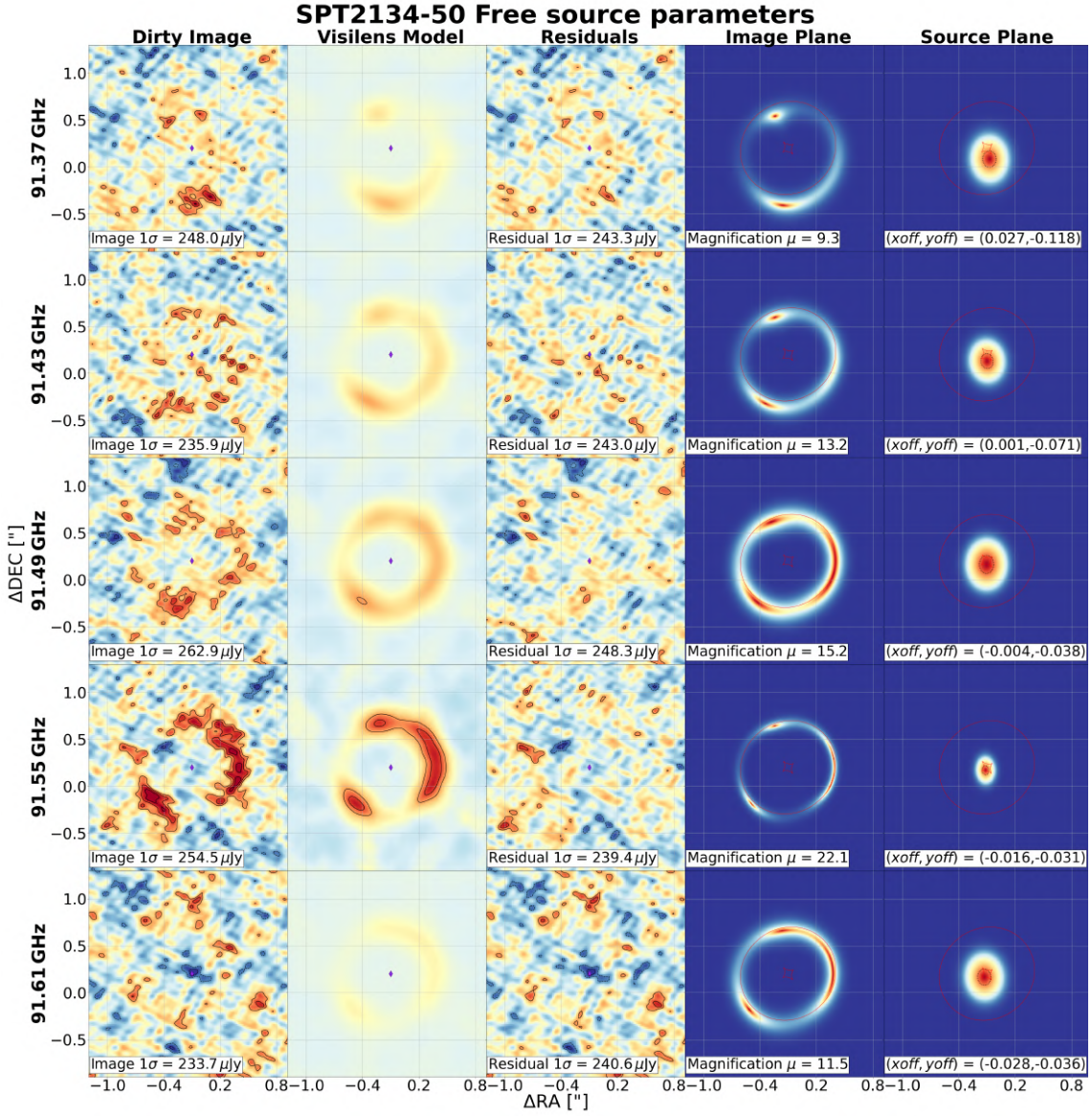

Figure 5.8: Gravitational lensing models for five bins of SPT2134-50.

Table 5.4: Fitted source parameters of different bins of SPT0125-47. The final five frequency bins are centralised around the specified values with widths of 0.04 GHz.

Bin	98.28-98.42 GHz	98.42-98.48 GHz	98.30 GHz[a]	98.34 GHz	98.38 GHz	98.42 GHz	98.46 GHz
$x_{\rm off}$ (")	-0.111 ± 0.012	-0.163 ± 0.020	-0.158 ± 0.032	-0.001 ± 0.028	-0.127 ± 0.010	-0.133 ± 0.010	-0.177 ± 0.022
$y_{\rm off}$ (")	0.053 ± 0.005	0.068 ± 0.018	0.092 ± 0.027	0.022 ± 0.016	0.058 ± 0.006	0.059 ± 0.008	0.087 ± 0.075
$S_{\rm CO(3-2)}$ (mJy)	1.715 ± 0.162	2.640 ± 0.345	1.810 ± 0.273	1.443 ± 0.289	2.381 ± 0.329	3.120 ± 0.397	2.233 ± 0.324
$n_{\rm S}$	0.461 ± 0.193	0.266 ± 0.091	0.508 ± 0.187	0.641 ± 0.393	0.907 ± 0.258	0.380 ± 0.144	0.346 ± 0.169
$a_{\rm S}$ (")	0.164 ± 0.014	0.172 ± 0.014	0.127 ± 0.024	0.144 ± 0.028	0.115 ± 0.016	0.130 ± 0.014	0.173 ± 0.016
$b_{\rm S}/a_{\rm S}$	0.433 ± 0.018	0.847 ± 0.135	0.594 ± 0.133	0.783 ± 0.091	0.767 ± 0.073	0.865 ± 0.083	0.910 ± 0.091
$\rm PA_S$ (deg)	165 ± 3	81 ± 22	148 ± 78	152 ± 14	156 ± 11	158 ± 13	137 ± 15
μ	17.9 ± 1.2	12.4 ± 0.9	11.7 ± 2.2	20.2 ± 3.1	15.2 ± 1.3	15.7 ± 1.1	11.6 ± 1.0

[a]This frequency bin was modelled with unfixed lens parameters. These were fitted to $x_{\rm L} = 0.716 \pm 0.056$, $y_{\rm L} = -0.328 \pm 0.033$, $M_{\rm L}/(10^{11} M_\odot) = 1.330 \pm 0.062$, $e_{\rm L} = 0.150 \pm 0.026$, $\rm PA_L = 16 \pm 17$.

Table 5.5: Fitted source parameters of different bins of SPT2134-50. The final five frequency bins are centralised around the specified values with widths of 0.06 GHz.

Bin	91.34-91.54 GHz	91.54-91.64 GHz	91.37 GHz	91.43 GHz	91.49 GHz	91.55 GHz	91.61 GHz
x_{off} (")	-0.007 ± 0.006	-0.027 ± 0.009	0.027 ± 0.020	0.001 ± 0.012	-0.004 ± 0.009	-0.016 ± 0.003	-0.028 ± 0.041
y_{off} (")	-0.070 ± 0.009	-0.026 ± 0.012	-0.118 ± 0.024	-0.071 ± 0.015	-0.038 ± 0.0172	-0.031 ± 0.005	-0.036 ± 0.075
$S_{\mathrm{CO(3-2)}}$ (mJy)	0.715 ± 0.116	0.410 ± 0.112	0.462 ± 0.132	0.455 ± 0.128	0.668 ± 0.152	0.568 ± 0.099	0.191 ± 0.098
n_{S}	1.153 ± 0.363	1.124 ± 0.511	1.110 ± 0.568	1.041 ± 0.491	0.864 ± 0.443	1.173 ± 0.491	1.033 ± 0.585
a_{S} (")	0.101 ± 0.015	0.086 ± 0.025	0.088 ± 0.021	0.080 ± 0.025	0.095 ± 0.019	0.051 ± 0.011	0.087 ± 0.029
$b_{\mathrm{S}}/a_{\mathrm{S}}$	0.856 ± 0.106	0.792 ± 0.165	0.800 ± 0.137	0.824 ± 0.132	0.801 ± 0.139	0.700 ± 0.146	0.814 ± 0.173
$\mathrm{PA_S}$ (deg)	91 ± 15	98 ± 15	93 ± 14	96 ± 16	90 ± 14	92 ± 13	94 ± 16
μ	11.9 ± 1.3	16.1 ± 3.4	9.3 ± 1.5	13.2 ± 2.6	15.2 ± 2.3	22.1 ± 2.5	11.5 ± 4.1

6
Discussion

Given the results in Chapter 5, more speculative explanations and hypotheses will be explored in this chapter. I begin in Section 6.1 by discussing general observational results from the moment maps and spectra of Section 5.1. This part includes comparison with other papers and derivation of intrinsic line properties for each source. From the results, mass and SFR estimates are given in Section 6.2. I build on this to explore hypothetical source characteristics in Section 6.3. One such key hypothesis is that SPT0125-47 is a rotating disc. This section is accompanied with a comparison of earlier lens and source models for the same sources.

6.1 Analysis of Line Data

Due to the large standard deviations from the fit with the skewed Gaussian, discussion and analysis in this section will centre around the fit with the regular Gaussian. This is not an obvious decision for SPT0125-47 since the skewed Gaussian appears to be a better fit. Evidence for this lie in the chi-square test yielding a value for the skewed Gaussian that is only 53 % that of the normal Gaussian, the residuals showing less systematic variations, and the FWHM being somewhat closer to values obtained in earlier works (see e.g. Béthermin et al., 2018). On the other hand, the mode frequency from the skewed Gaussian is actually a slightly worse match with the predicted value of $\nu = \nu_{\text{rest}}/(1+z) = 98.38\,\text{GHz}$, although the median frequency is identical with the normal Gaussian central frequency. For SPT2134-50 the skewed Gaussian has comparable residuals, and larger and more deviating FWHM and mode frequency. For this source the chi-square is only slightly smaller for the skewed Gaussian. More exactly, it is 73 % of that of the normal Gaussian. The mode frequency of the normal Gaussian (91.51 GHz) is larger than the predicted 91.48 GHz which could be due to the high levels of noise.

Obtained FWHMs (see Table 5.1) can be compared to earlier documented results for CO(3-2). For SPT0125-47 the obtained $380\,\text{km}\,\text{s}^{-1}$ is clearly smaller than the typical $500\,\text{km}\,\text{s}^{-1}$ presented in Béthermin et al. (2018, figure 8). When testing to decrease the spectral resolution, it was concluded that the value of $380\,\text{km}\,\text{s}^{-1}$ did not change decidedly. No such discrepancy is found for SPT2134-50. The obtained value of $550\,\text{km}\,\text{s}^{-1}$ is consistent with $522\,\text{km}\,\text{s}^{-1}$, from Weiß (2013). Furthermore, for both sources the $L'_{\text{CO(3-2)}}$ is similar to the $L'_{\text{CO(1-0)}}$ from Aravena et al. (2016).

Intrinsic luminosities are presented in Table 6.1. They have been obtained by first dividing the received intensity (see Table 5.1) with the estimated magnification factors (see Table 5.3) and then applying Equation 3.10 and 3.11 as before.

Table 6.1: Intrinsic line properties that are calculated from the observed spectral features: $L = \mu L/\mu$, where L is the intrinsic luminosity of the second and third column in this table, μL is the direct luminosity of the third and fourth column in Table 5.1, and μ is the magnification in Table 5.3.

Source	SPT0125-47		SPT2134-50	
Gaussian	Normal	Skewed	Normal	Skewed
$L_{\mathrm{CO(3-2)}}$ $(10^7\,\mathrm{L}_\odot)$	6.8 ± 1.2	7.0 ± 5.6	1.9 ± 0.49	2.1 ± 1.1
$L'_{\mathrm{CO(3-2)}}$ $(10^{10}\mathrm{K\,km\,s^{-1}\,pc^2})$	5.1 ± 0.89	5.3 ± 4.2	1.5 ± 0.37	1.6 ± 0.83

6.2 Mass Estimates

In this section considerably more speculative values will be extracted from the data. Each galaxy parameter that is calculated rests on several empirically derived relations and associated assumptions. For some values, error estimations will not be explicit because these would exceed the magnitude of the derived value. For the values where error propagation has been used it should be remembered that actual errors are likely several times the obtained value. This section concerns dynamical mass, molecular gas mass, SFR, depletion timescale and the Schmidt-Kennicutt law.

6.2.1 Dynamical Mass

The dynamical mass is $M_{\mathrm{dyn}} = v_{\mathrm{rot}}^2 R/G$, where v is the rotational velocity and R is the radius of the disc. There are two natural choices for the rotational velocity: half of the FWHM, and the velocity from the moment-1 map. If the source is a rotating disk, these values should coincide. There are also two choices for the galactic radius: the obtained model major axis (a in Table 5.3), and the difference in source position for maximally separate bins. Since the second choice is based on a smaller selection of frequency channels it is more susceptible to noise, but also a more logical choice for rotating disks. As the observations are of CO(3-2) the uncertainties of the actual shape, radius and inclination angle of the source dominates the difference between these choices of velocity and radius.

In order to use the dynamical mass definition, it can first be assumed that the disk is truly circular. That means that $b/a = \cos i$, where i is the inclination angle the line of sight makes with the normal to the disk plane. For both sources, this assumption agrees partly with Law et al. (2009) where $\langle \sin i \rangle \approx 0.79$ for randomly oriented disks. The observed radial velocity in the moment-1 map must then be $v_{\mathrm{obs}} = v_{\mathrm{rot}} \sin i$; if the axis ratio is zero the galaxy is seen edge on and $v_{\mathrm{obs}} = v_{\mathrm{rot}}$ because $i = 90\,\mathrm{deg}$. It follows that

$$M_{\mathrm{dyn}} = \frac{v_{\mathrm{obs}}^2 a}{\sin^2(\arccos b/a) G}. \tag{6.1}$$

Using $v = \mathrm{FWHM}/2$ and R as the difference in position of the source models, estimated values for SPT0125-47 and SPT2134-50 are $M_{\mathrm{dyn}} = (2.9 \pm 0.87)10^{10}\,\mathrm{M}_\odot$ and $M_{\mathrm{dyn}} = (3.1 \pm 1.6)10^{10}\,\mathrm{M}_\odot$, respectively. These values agree with typical SPT

DSFGs from Aravena et al. (2016). The same paper produces a dynamical mass of $M_{\rm dyn} = (1.6 \pm 1.2)10^{10}\,{\rm M}_\odot$ for SPT2134-50, which is about half the result in this thesis.

6.2.2 Molecular Gas Mass

As explained in Section 3.4.1, from $L'_{\rm CO(3-2)}$ the molecular gas mass can be approximated. To do this, a conversion factor between CO(1-0) line luminosity and total molecular gas mass is used. The conversion factor $\alpha_{\rm CO}$ is typically $\alpha_{\rm CO} \sim 4\,{\rm M}_\odot({\rm K\ km\ s^{-1}\,pc^2})^{-1}$ in nearby spiral galaxies (Bolatto et al., 2013) but only one fifth of this in ULIRGS (Downes and Solomon, 1998). This $\alpha_{\rm CO}$ is, however, the conversion factor between the molecular gas mass and $L'_{\rm CO(1-0)}$. Therefore, another factor, $r_{31} = L'_{\rm CO(3-2)}/L'_{\rm CO(1-0)}$, is needed. Bolatto et al. (2013) summarised this to be $r_{31} \sim 1$ for very compact starbursts surrounding QSOs, and $r_{31} \sim 0.5 - 0.7$ for SMGs. In conclusion,

$$M_{\rm gas} = \frac{L'_{\rm CO(3-2)}\alpha_{\rm CO}}{r_{31}}. \tag{6.2}$$

From Aravena et al. (2016), I use $\alpha_{\rm CO} = 0.7 \pm 0.2$ for SPT0125-47 and $\alpha_{\rm CO} = 1.1 \pm 0.3$ for SPT2134-50. The used line luminosity ratio is taken from what Mao et al. (2010) found for ULIRGs ($r_{31} = 0.96 \pm 0.14$). This use is supported by the observation that $L'_{\rm CO(3-2)}$ obtained in this thesis agreed with $L'_{\rm CO(1-0)}$ from Aravena et al. (2016). From these assumptions, obtained molecular gas masses, for regular Gaussian fits, are $M_{\rm gas} = (3.4 \pm 1.1)10^{10}\,{\rm M}_\odot$ for SPT0125-47 and $M_{\rm gas} = (1.6 \pm 0.49)10^{10}\,{\rm M}_\odot$ for SPT2134-50. Since the actual nature of the sources is still unknown, the assumptions behind $\alpha_{\rm CO}$ and r_{31} are very uncertain. Still, obtained gas masses are typical for ALMA starbursts (see e.g. Silverman et al., 2018; Aravena et al., 2016). Exact numbers obtained by Aravena et al. (2016) are $M_{\rm gas} = (11.5 \pm 1.0)10^{10}\,{\rm M}_\odot$ for SPT0125-47 and $M_{\rm gas} = (1.3 \pm 0.3)10^{10}\,{\rm M}_\odot$ for SPT2134-50. The fact that the molecular gas mass and the dynamical mass are similar in size indicates a large gas mass fraction, which is expected (see Chapter 2 and Tacconi et al. (2013)).

6.2.3 Star Formation Rate

If the SFRs were known, the Star Formation Efficiency (SFE = SFR/$M_{\rm gas}$) and the depletion timescale $t_{\rm dep} = 1/{\rm SFE}$ could be calculated. Since they are not, the IR luminosities obtained by SED fitting by Aravena et al. (2016) will be used. The SFR is obtained by correcting for the lens magnification μ and conversing from intrinsic IR luminosity to SFR with $C_{\rm IR} = 1.4 \times 10^{-10}\,{\rm M}_\odot\,{\rm yr}^{-1}\,{\rm L}_\odot^{-1}$ (Calzetti, 2013, Table 1.1):

$${\rm SFR} = \frac{C_{\rm IR}L_{\rm IR}}{\mu}. \tag{6.3}$$

When adapting $C_{\rm IR}$, I assumed an IMF mass range of $0.1 - 100\,{\rm M}_\odot$ and 10 Myr of constant star formation. This leads to ${\rm SFR} = (1100 \pm 790)\,{\rm M}_\odot\,{\rm yr}^{-1}$ for SPT0125-47 and ${\rm SFR} = (500 \pm 360)\,{\rm M}_\odot\,{\rm yr}^{-1}$ for SPT2134-50, indicating clear starburst episodes. Now, the depletion timescale, $t_{\rm dep} = M_{\rm gas}/{\rm SFR}$, can be estimated, yielding $t_{\rm dep}30 \pm$

23 Myr for SPT0125-47 and $t_{\rm dep}31 \pm 26$ Myr for SPT2134-50. These are be typical values for lensed DSFGs (Aravena et al., 2016, Figure 7).

It could be of interest to test the Schmidt-Kennicutt law on both of the SPT sources. As a first step for this, the observed galactic area is calculate by multiplying its radius with the angular diameter distance and squaring the results. The difference between choosing the obtained major axis and the frequency-dependent source position for the radius dwarfs in comparison to uncertainties in the conversion factors used for the molecular gas mass and, more importantly, the SFR. In approximation $\Sigma_{\rm SFR} = {\rm SFR}/R^2 \sim 5 \times 10^2\,{\rm M}_\odot\,{\rm kpc}^2\,{\rm yr}^{-1}$ and $\Sigma_{\rm gas} = M_{\rm gas}/R^2 \sim 10^4\,{\rm M}_\odot\,{\rm pc}^2$ for SPT0125-47 and twice these values for SPT2134-50. Like many highly star-forming galaxies, this places the sources on the upper edge of the typical line (e.g. Kennicutt, 1992; Krumholz et al., 2012; Kuhlen et al., 2012).

6.3 Gravitational Lensing

Strong gravitational lensing is present for both sources. The lensing magnification increases the spatial resolution of the observations, though with strong lensing there will be variation across the source as some regions are more magnified than others. In this section, the reliability of the mass models and the estimated magnification from gravitational lensing is discussed. Further, different scenarios explaining the velocity gradient and structure of SPT0125-47 is discussed. Particular focus is given to the scenario that SPT0125-47 could be a rotating disk.

6.3.1 Reliability of Lens and Source Models

As previously commented on in Chapter 5, the estimated Einstein radii are slightly smaller than indicated by the moment-0 maps. However, since the resulting `visilens` models appear to be of the same size as the ring-like structures in the dirty images and the residuals are, in fact, minimised by the obtained lens masses, this apparent error could be caused by the extension of the background source. If the obtained masses are correct, the Einstein angles would be $0.98''$ and $0.50''$ for SPT0125-47 and SPT2134-50, respectively. That is within the margin of error arising from the observed intensity not being perfectly circular, and thin.

Comparison of models obtained in this thesis with previously obtained models is largely a question of how angular resolution affects the simulations. For instance, the angular resolution used in this thesis is around five times superior to what was used by Spilker et al. (2016). In that work, this question was accentuated with the comment that the generally clumpy structures of DSFGs (see e.g. Swinbank et al., 2011; Dye et al., 2015) can cause uneven magnification and be poorly modelled as simple Sérsic sources. A tentative and partial answer to this issue resides in the simulations of this thesis. The exact effect of improved angular resolution can of course never be shown since many parameters and noise will inevitably differ between studies.

Compared to lens and source models from Spilker et al. (2016), the models obtained in this thesis are different for SPT0125-47 but similar for SPT2134-50. Source clumpiness would require even higher resolution to distinguish it from noise.

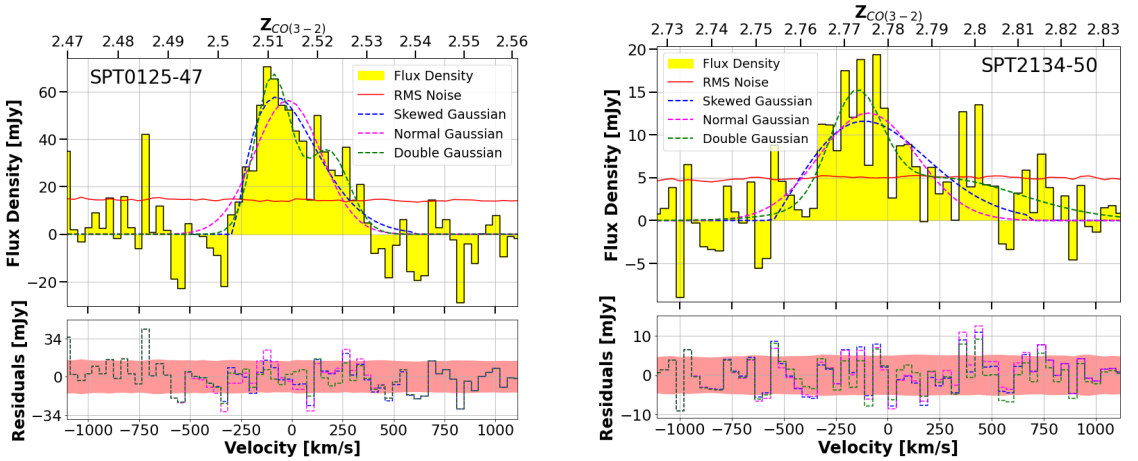

Figure 6.1: *Top row:* The CO(3-2) spectra of SPT0125−47 (left) and SPT2134−50 (right). The dashed lines show the resulting fitted Gaussian (magenta), skewed Gaussian (blue), and double Gaussian (green) line profiles. The 1σ RMS noise is shown by the red line. *Bottom row:* The residuals from the two line profile fits. The pink coloured regions indicates the 1σ RMS. For both rows, the zero velocity corresponds to the assumed redshifts (of Table 4.2).

Good fits of models for different intensity maps can also be a clue that fitted models have too many degrees of freedom. Thus, a dilemma arises between models that are too simple to be realistic and models that are too complex to ever give bad fits. `visilens` attempts to solve this issue with the deviance information criterion (Spiegelhalter et al., 2002), but this needs to work in tandem with a good understanding of which parameters can be restricted and near what values. For example, the deviance information criterion argued for my fixing the shear forces despite it most often being present and varying, at least to a small extent, in observations of the high-redshift Universe (see e.g. Kilbinger, 2015).

6.3.2 Double Gaussian Profile Fitting

As an alternative to the luminosity profile, a double Gaussian profile is included here (in addition to the Gaussian and skewed Gaussian profile fits of Chapter 5). The double Gaussian fit is shown in Figure 6.1. The increased flexibility that comes with the additional parameters produce smaller residuals, as expected. A stronger argument for using a double Gaussian profile for SPT0125-47 is the lower apparent systematic variations in the residuals. This is less clear for SPT2134-50. Adding Gaussian profiles to fit the spectra result in constituents with larger amplitude having smaller FWHMs. Specifically, the FWHM of SPT0125-47 are presented in Table 6.2, together with other observed line properties. These FWHMs are smaller than typical, which challenges the hypothesis of the sources being mergers, since mergers should have wider spectral profiles due to e.g. rotation or gas flow.

The chi-square tests made with `scipy` are presented in Table 6.3. It can easily be seen that the argument for a non-standard Gaussian is considerably stronger for SPT0125-47 than for SPT2134-50. In particular the double Gaussian is well fitted

Table 6.2: Parameters from the fit of a sum of two Gaussian functions for SPT0125-50 and SPT2134-50 each. This is the double Gaussian addendum to Table 5.1. The bottom two rows are calculated by fitting a linear curve to the four different obtained magnifications, neglecting 98.30 GHz for SPT0125-47 and 91.61 GHz for SPT2134-50 due to deviant numbers and being maladapted for the lens. From this curve fit, the magnification could be red, assuming errors of ±2.5. In the bottom five rows, the numbers of the total Gaussian is the sum of its two constituents.

Source	SPT0125-47			SPT2134-50		
Gaussian	First	Second	Total	First	Second	Total
Amplitude (mJy)	66 ± 8.2	35 ± 7.1	67 ± 8.2	12 ± 3.4	5.0 ± 1.7	15 ± 3.4
Central[a] frequency (GHz)	98.41 ±0.029	98.33 ±0.034	98.41 ±0.036	91.53 ±0.038	91.41 ±0.12	91.52 ±0.079
Central[a] redshift	2.5137 ±0.0010	2.5169 ±0.0012	2.5138 ±0.0013	2.7780 ±0.0016	2.7829 ±0.0050	2.7783 ±0.0032
FWHM[b] ($\mathrm{km\,s^{-1}}$)	200 ± 43	250 ± 98	260 ± 98	290 ± 94	930 ± 360	610 ± 360
$I_{CO(3-2)}$ ($\mathrm{Jy\,km\,s^{-1}}$)	14 ± 3.5	9.2 ± 4.1	23 ± 5.4	3.8 ± 1.6	4.9 ± 2.6	9.7 ± 3.1
$\mu L_{CO(3-2)}$ ($10^8\,\mathrm{L_\odot}$)	6.6 ± 1.6	4.2 ± 1.9	10.8 ± 2.5	2.0 ± 0.87	2.6 ± 1.4	4.0 ± 1.6
$\mu L'_{CO(3-2)}$ ($10^{11}\,\mathrm{K\,km\,s^{-1}\,pc^2}$)	5.0 ± 1.2	3.1 ± 1.4	8.1 ± 1.8	1.5 ± 0.66	2.0 ± 1.0	3.0 ± 1.2
$L_{CO(3-2)}$ ($10^6\,\mathrm{L_\odot}$)	44 ± 13	21 ± 11	65 ± 17	10 ± 4.6	22 ± 12	32 ± 13
$L'_{CO(3-2)}$ ($10^9\,\mathrm{K\,km\,s^{-1}\,pc^2}$)	33 ± 9.7	16 ± 7.3	49 ± 12	7.9 ± 3.4	16 ± 9.1	24 ± 10

[a] Like in Table 5.1, this is actually the mode frequency. The median frequencies were calculated as well, yielding 98.39 ± 0.036 GHz for SPT0125-47 and 91.50 ± 0.079 GHz for SPT2134-50. The corresponding redshifts are 2.5146 ± 0.0013 and 2.7792 ± 0.0032, respectively

[b] The double Gaussian crosses the half maximum point for times. For this function the FWHM is defined as the largest distance between these points.

to the previous. Also, the skewed Gaussian is much better fitted to this source than to SPT2134-50. This is not surprising because the magnification gradient of SPT2134-50 (see Table A.2) has the opposite direction to that of SPT0125-47. Therefore the physical motivation is to have the skewed Gaussian being skewed in the opposite direction. Doing this indeed improves the chi-square, but only if the data with $v > 300\,\mathrm{km\,s^{-1}}$ is ignored. The small number of analysed data points (19 for SPT0125-47 and 23 for SPT2134-50) decreases the certainty of the chi-square-based conclusions.

These double Gaussian profiles could have many reasons, two of which are galaxy mergers or interactions, and rotating disks with limited spectral and angular resolution. Galaxy-galaxy interactions and mergers are not needed explanations for either source since both produced good fits when modelled as single discs with a Sérsic profile. Moreover, the simulations did not produce any visible improvement when adding multiple sources. Still, faint companion galaxies or satellite galaxies, producing flux below the RMS noise level, cannot be dismissed. Any statistical prior using typical merger rates need to consider basic properties like velocity difference and stellar mass. For instance, Equation 2.22 is created for FWHM $\lesssim 200\,\mathrm{km\,s^{-1}}$, and $M_\star \gtrsim 10^{10}\,\mathrm{M_\odot}$ and requires a known merger fraction at $z = 0$. The highest merger fractions found by Conselice et al. (2003) is $40 - 50\,\%$ for Lyman break-galaxies with $M_\mathrm{B} < -21$ or $M_\star > 10^{10}\,\mathrm{M_\odot}$. If SPT0125-47 comprised two or more

Table 6.3: Chi-square results for the functions fitted in this thesis. The degree of freedom is defined as dof $= k - 1 - p$ where k is the number of observed frequencies and p is the number of fitted parameters. For both sources $p = 3$ for the normal and skewed Gaussian, and $p = 6$ for the double Gaussian. The number of frequencies for the fit is $k = 19$ for SPT0125-47 and $k = 23$ SPT2134-50.

Source	SPT0125-47			SPT2134-50		
Gaussian function	Normal	Skewed	Double	Normal	Skewed	Double
χ^2	138	73.9	43.5	111	81.0	52.0
χ/dof	9.20	4.92	3.63	5.82	4.26	3.25

mergers, the related gravitational interactions could explain its high luminosity.

6.3.3 Other Potential Source Characteristics

Gas flows produce extended emission with very high velocity. If this were present, it would be exposed in the corresponding spectrum as increased amplitudes near the line edges. For SPT0125-47, no form of Gaussian function fitted in this thesis systematically predict these edges as lower than they are. Nor is this clearly compensated by having a lower peak than the measured data. For SPT2134-50 on the other hand, large flux densities are observed far from the FWHMs. The not completely circular shape of this source especially could be signs of violent events but, like the spectrum, this could also be explained by the large levels of noise. If the sources were very irregular they would be difficult to model as Sérsic sources in the manner that is done in this thesis.

Both sources display clumpy moment-0 maps. The sizes of the clumps are roughly equal to the beam size ($\sim 0.1''$), which means that eventual underlying structures could be smaller. Physical sizes are per definition calculated as the product of the angular size and the angular diameter distance. Dividing by the magnification in the radially orthogonal direction, it follows that these clumps measure $\lesssim 50\,\mathrm{pc}$. In comparison, typical GMC diameters range from 5 pc to 200 pc. Observed amplitudes are often 2σ larger than the general source emission, suggesting they are not noise. If these clumps truly are resolved GMCs they would be more stretched in the circular direction than in the radial, something that can only vaguely be discerned for SPT2134-50. Under this same assumption, with less noisy data irregular clump shapes should remain due to projection effects.

6.3.4 SPT0125-47

The obtained magnification factor for the CO(3-2) line ($\mu_{\mathrm{CO(3-2)}} = 15.4 \pm 0.9$) is considerably larger than for the 870 µm continuum emission ($\mu_{870} = 5.5 \pm 0.1$). Aravena et al. (2016) estimates the CO magnification factor with the formula

$$\mu_{\mathrm{CO}} = 3\frac{L'_{\mathrm{CO}}}{10^{11}\,\mathrm{K\,km\,s^{-1}\,pc^2}}\left(\frac{\mathrm{FWHM}}{400\,\mathrm{km\,s^{-1}}}\right)^{-2.3} \tag{6.4}$$

to be 21 ± 4. Values obtained in this thesis (see Table 5.1 and 6.1) would not be applicable to this formula since it is fitted for low-J (2-1 and 1-0) CO-transitions.

Compared to previous source models by Spilker et al. (2016), the most important disparity in the models is that SPT0125-47 could be modelled as just one source in this thesis (instead of three). A first explanation for this is that Spilker et al. (2016) observed 870 µm continuum emission whilst this thesis used CO(3-2) line emission. Another reason is the higher resolution in the ALMA data used in this thesis ($\sim 0.1''$ compared to $\sim 0.5''$). This improved resolution confirmed the flux domination of the eastern region of the Einstein-ring, but also suggested that the flux on the opposite side is more evenly spread out, without a clear gap in the north-west region. This flux distribution could have been more difficult to model. The lens position had to move closer to the source position in this model.

Modelling the source as one disk galaxy and not including any shear forced the lens model to differ from the one obtained by Spilker et al. (2016). Perhaps the clearest parameter difference is the ellipticity which is less than half in this thesis: 0.166 ± 0.019 compared to 0.40 ± 0.01. Neither of these values are abnormal (see e.g. Spilker et al., 2016).

The CO(3-2) of SPT0125−47 has a clear velocity gradient. From the dirty image column of Figure 5.6 the most luminous region can be seen as moving counter-clockwise from the top left to the bottom left area of the ring-like structure, as frequency increases. Supporting this hypothesis, the source plane column illustrates a decreasingly elliptic source with a slowly increasing position angle. With the exception of the first row, the source offset increases in the south-west direction.

The credibility of this hypothesis is decreased by the fact that the observed intensity distribution of 98.30 GHz required another lens model than what was obtained from the full line. A complex intensity distribution and separate lens model is primarily a critique to the source and image plane visual models, but could also suggest miscellaneous spectral processes. The peak amplitude of the high-intensity region lie within four contour lines, which corresponds to 5σ, ruling out noise as an explanation.

Another feature of Figure 5.6 is that the estimated magnification decreases with frequency for all rows except the first row. Higher frequency is equivalent to smaller redshift or smaller velocity away from the observer, i.e. the left side of Figure 5.3. Thus, this finding validates the fit of the skewed Gaussian, which is monotonously scaled with increasing redshift, velocity, or decreasing frequency. However, this skewed appearance could also be explained by the presence of multiple sources, as shown in Figure 6.1.

These three observations about rotational source appearance, moment-1 map, and skewed magnification can be united from the understanding that the part of the source that rotates toward the observer would — under the specific lens-to-source offset — be magnified less than the part that rotates away. The moment-1 map of Figure 5.2 shows higher relative velocity in the inner region of the top left part of the ring, and the outer region of the bottom right part. Tracing light rays around the lens would therefore suggest a rotation along this diagonal with the top right region moving away from the observer.

It must be noted that the rotational source appearance, velocity patterns in the moment-1 map, and skewed magnification could be reproduced by a merger system as well. Mergers are discernable from rotational system in that a longer

sequence of smaller frequency bins containing fractions of a lens modelled emission line should result in bins where no good source model could be obtained due to the merger galaxies moving in ways a single disk cannot. Equivalently, as the flux from a merger fades out of the modelled frequency bin, the source should show sudden jumps in the source parameters. The feasibility of such a method is again dependent on the frequency shift of the mergers as well as the level of noise.

6.3.5 SPT2134-50

In contrast to SPT0125-47, the obtained magnification factor for the CO(3-2) line of SPT2134-50 matches the 870 µm continuum emission magnification very well; the respective values are $\mu_{\mathrm{CO}(3-2)} = 20.2 \pm 2.9$ and $\mu_{870} = 21.0 \pm 2.4$ (Spilker et al., 2016). The μ_{CO} predicted by Aravena et al. (2016) was $\mu = 7 \pm 6$. From gravitational lensing models of 3.6 µm continuum emission by Ma et al. (2015) the obtained magnification was $\mu 21.00 \pm 2.42$. The fact that different wavelengths produce different models is further motivated by Dong et al. (2019) where the authors were unable to find an acceptable lens model from observations of the CO(7-6), CO(3-2) and CO(1-0) lines.

Other explanations as to their inability to produce lens and source models for SPT2134-50, in contrast to this thesis, could be noise, increased resolution in this thesis, or different assumptions. Data used by Dong et al. (2019) had resolution $0.2 - 0.4''$ which is $2 - 4$ times the resolution used for SPT2134-50 in this thesis. Both I and Dong et al. (2019) used `visilens` where the lens was modelled as a SIE. Their conclusion that the SIE is an insufficient lens model for SPT2134-50 is thereby contradicted. Like this thesis, Dong et al. (2019) also assumed Sérsic profiles for the sources. Lens redshift is unspecified in their paper, but a different redshift is often compensated with a different mass.

Some rotational features are present for SPT2134-50 too. Ignoring the 91.61 GHz frequency bin, the magnification increases from $\mu_{91.37\,\mathrm{GHz}} = 9.3$ to $\mu_{91.55\,\mathrm{GHz}} = 22.1$ while offset positions move to the west with increasing frequency. To test this, the skewed Gaussian should have been fitted with the opposite chirality. This was actually done, although not presented, because the fit was significantly worse for the same reason that the weaker peak of the double Gaussian fit can be found to the right of the main peak. Especially the large radio velocities were poorly fitted with such a function.

7

Conclusions and Outlook

In this thesis two gravitationally lensed high-redshift starburst galaxies have been analysed in the background of early galaxy evolution. The study of galaxies is rapidly expanding thanks to new discoveries in fields like cosmology, hydrodynamics, and stellar evolution on which it depends, as well as new tools for simulation and observation. Two such tools that have been central for this thesis are ALMA and `visilens`. ALMA observed the CO(3-2) transition of SPT0125-47 and SPT2134-50 in the angular resolution $\sim 0.1''$. After calibration with CASA, this data was used by `visilens` for the modelling of visibility-based gravitational lensing of multiple line fractions for each source.

Both sources could be modelled as Sérsic sources behind a SIE, in a galaxy-galaxy strong gravitational lensing system. Improved angular resolution could explain why obtained models differ from some of the previously obtained models. However, this discrepancy could also be due to noise, especially in the case of SPT2134-50, which is observed at $< 3\sigma$ threshold. I have also discussed the problem of fitting multi-variable components to noisy or flexible data and how different models could produce similar images. On the whole, simulations of gravitational lensing is, like most techniques, a helpful tool that needs to be accompanied with an understanding of the environment that is measured and our current limits of that understanding.

Nevertheless, from the observations and simulations many feasible values could be retrieved. To begin, estimated magnifications are $\mu = 15.4 \pm 0.9$ for SPT0125-47, and 20.2 ± 2.9 for SPT2134-50. In combination with spectral characteristics, it follows that $L_{\mathrm{CO(3-2)}} = 6.8 \pm 1.1 \times 10^7\,\mathrm{L}_\odot$ and $L'_{\mathrm{CO(3-2)}} = 5.1 \pm 0.84 \times 10^{10}\,\mathrm{K\,km\,s^{-1}\,pc^2}$ for SPT0125-47, and $L_{\mathrm{CO(3-2)}} = 1.9 \pm 0.41 \times 10^7\,\mathrm{L}_\odot$ and $L'_{\mathrm{CO(3-2)}} = 1.5 \pm 0.31 \times 10^{10}\,\mathrm{K\,km\,s^{-1}\,pc^2}$ for SPT2134-50. With these values the gas mass fractions are indicated to be close to one. Additionally, both source, but SPT0125-47 in particular, show tendencies of very high SFRs ($\sim 10^3\,\mathrm{M}_\odot\,\mathrm{yr}^{-1}$) and follow the Schmidt-Kennicutt law for starbursts.

Several different galactic mechanisms could be present in both galaxies. The total luminosity, and skewed spectral distribution of SPT0125-47 could be explained by galactic mergers. The second aspect could also be due to rotation, a mechanism that likewise would explain the rotation in the moment-1 map as well as the very roughly linear dependency on frequency for the magnification. Both sources show $\lesssim 50\,\mathrm{pc}$ large clumps around a 2σ flux amplitude which could, with reservation for noise, be GMCs.

This thesis is concurrently a case for how far extragalactic astronomy has come, as for how much left there is to discover. To be able to speculate around the distribution of GMCs and galactic mechanisms for galaxies with $z > 2.5$ has

only become possible in the last decade thanks to the groundbreaking capabilities of ALMA, and implementations of gravitational lensing. To further investigate the sources additional observations and analysis of partial-line gravitational lensing could answer whether SPT0125-47 is a system of mergers or merely a rotational disk and, by comparing clump positions, if these blobs are clouds or noise. Observations in different frequencies, suggestively IR with the JWST, would significantly reduce the uncertainties for the galactic parameters. By employing the methodology of this thesis on other gravitationally lensed sources the demographics of characteristics other than line profiles and magnifications could be discriminated. Expansion of ALMA coverage to band 1 and 2 would be able to discern CO(2-1) of galaxies at similar redshift with even better resolution (Huang, 2019; Yagoubov et al., 2020).

Bibliography

Alves, J., Lombardi, M., and Lada, C. J. (2007). The mass function of dense molecular cores and the origin of the IMF. *Astronomy and Astrophysics*, 462(1):L17–L21.

Aravena, M., Spilker, J. S., Bethermin, M., Bothwell, M., Chapman, S. C., de Breuck, C., Furstenau, R. M., Gónzalez-López, J., Greve, T. R., Litke, K., Ma, J., Malkan, M., Marrone, D. P., Murphy, E. J., Stark, A., Strandet, M., Vieira, J. D., Weiss, A., Welikala, N., Wong, G. F., and Collier, J. D. (2016). A survey of the cold molecular gas in gravitationally lensed star-forming galaxies at z > 2. *Monthly Notices of the Royal Astronomical Society*, 457(4):4406–4420.

Bachiller, R. and Cernicharo Quintanilla, J. (2008). *Science with the Atacama Large Millimeter Array: A New Era for Astrophysics*. Springer, first edition.

Baldry, I. K., Balogh, M. L., Bower, R., Glazebrook, K., and Nichol, R. C. (2004a). Color bimodality: Implications for galaxy evolution. In Allen, R. E., Nanopoulos, D. V., and Pope, C. N., editors, *The New Cosmology: Conference on Strings and Cosmology*, volume 743 of *American Institute of Physics Conference Series*, pages 106–119.

Baldry, I. K., Glazebrook, K., Brinkmann, J., Ivezić, Ž., Lupton, R. H., Nichol, R. C., and Szalay, A. S. (2004b). Quantifying the Bimodal Color-Magnitude Distribution of Galaxies. *Astrophysical Journal*, 600(2):681–694.

Balick, B. and Brown, R. L. (1974). Intense sub-arcsecond structure in the galactic center. *Astrophysical Journal*, 194:265–270.

Barkana, R. and Loeb, A. (2001). In the beginning: the first sources of light and the reionization of the universe. *Physics Reports*, 349(2):125–238.

Barker, S., de Grijs, R., and Cerviño, M. (2008). Star cluster versus field star formation in the nucleus of the prototype starburst galaxy M 82. *Astronomy and Astrophysics*, 484(3):711–720.

Bars, I. and Terning, J. (2009). *Extra Dimensions in Space and Time*, pages 27–. Multiversal Journeys. Springer.

Baugh, C. M. (2006). A primer on hierarchical galaxy formation: the semi-analytical approach. *Reports on Progress in Physics*, 69(12):3101–3156.

Béthermin, M., Greve, T. R., De Breuck, C., Vieira, J. D., Aravena, M., Chapman, S. C., Chen, C.-C., Dong, C., Hayward, C. C., Hezaveh, Y., Marrone, D. P., Narayanan, D., Phadke, K. A., Reuter, C. A., Spilker, J. S., Stark, A. A., Strandet,

M. L., and Weiß, A. (2018). Dense-gas tracers and carbon isotopes in five 2.5 < z < 4 lensed dusty star-forming galaxies from the SPT SMG sample. *Astronomy & Astrophysics*, 620:A115.

Bolatto, A. D., Wolfire, M., and Leroy, A. K. (2013). The CO-to-H_2 Conversion Factor. *Annual Review of Astronomy and Astrophysics*, 51(1):207–268.

Bonnor, W. B. (1956). Boyle's Law and gravitational instability. *Monthly Notices in the Royal Astronomical Society*, 116:351.

Booth, R. S. (1991). The European VLBI network. *Advances in Space Research*, 11(2):397–401.

Boquien, M., Buat, V., and Perret, V. (2014). Impact of star formation history on the measurement of star formation rates. *Astronomy and Astrophysics*, 571:A72.

Bouché, N., Dekel, A., Genzel, R., Genel, S., Cresci, G., Förster Schreiber, N. M., Shapiro, K. L., Davies, R. I., and Tacconi, L. (2010). The Impact of Cold Gas Accretion Above a Mass Floor on Galaxy Scaling Relations. *Astrophysical Journal*, 718(2):1001–1018.

Boulanger, F. (1999). Dust Emission and ISM Components. In Taylor, A. R., Landecker, T. L., and Joncas, G., editors, *New Perspectives on the Interstellar Medium*, volume 168 of *Astronomical Society of the Pacific Conference Series*, page 173.

Bouwens, R. J., Illingworth, G. D., Oesch, P. A., Franx, M., Labbé, I., Trenti, M., van Dokkum, P., Carollo, C. M., González, V., Smit, R., and Magee, D. (2012). UV-continuum Slopes at z ∼4-7 from the HUDF09+ERS+CANDELS Observations: Discovery of a Well-defined UV Color-Magnitude Relationship for z >= 4 Star-forming Galaxies. *Astrophysical Journal*, 754(2):83.

Bouwens, R. J., Illingworth, G. D., Oesch, P. A., Labbé, I., Trenti, M., van Dokkum, P., Franx, M., Stiavelli, M., Carollo, C. M., Magee, D., and Gonzalez, V. (2011). Ultraviolet Luminosity Functions from 132 z ∼7 and z ∼8 Lyman-break Galaxies in the Ultra-deep HUDF09 and Wide-area Early Release Science WFC3/IR Observations. *Astrophysical Journal*, 737(2):90.

Cañameras, R., Nesvadba, N., Kneissl, R., Frye, B., Gavazzi, R., Koenig, S., Le Floc'h, E., Limousin, M., Oteo, I., and Scott, D. (2017). Planck's dusty GEMS. IV. Star formation and feedback in a maximum starburst at z = 3 seen at 60-pc resolution. *Astronomy & Astrophysics*, 604:A117.

Calzetti, D. (2013). Star Formation Rate Indicators. In Falcón-Barroso, J. and Knapen, J. H., editors, *Secular Evolution of Galaxies*, page 419. Cambridge University Press.

Cano-Díaz, M., Sánchez, S. F., Zibetti, S., Ascasibar, Y., Bland-Hawthorn, J., Ziegler, B., González Delgado, R. M., Walcher, C. J., García-Benito, R., Mast, D., Mendoza-Pérez, M. A., Falcón-Barroso, J., Galbany, L., Husemann, B., Kehrig, C., Marino, R. A., Sánchez-Blázquez, P., López-Cobá, C., López-Sánchez, Á. R.,

and Vilchez, J. M. (2016). Spatially Resolved Star Formation Main Sequence of Galaxies in the CALIFA Survey. *Astrophysical Journal Letters*, 821(2):L26.

Capak, P. L., Carilli, C., Jones, G., Casey, C. M., Riechers, D., Sheth, K., Carollo, C. M., Ilbert, O., Karim, A., Lefevre, O., Lilly, S., Scoville, N., Smolcic, V., and Yan, L. (2015). Galaxies at redshifts 5 to 6 with systematically low dust content and high [C II] emission. *Nature*, 522(7557):455–458.

Carilli, C. L. and Walter, F. (2013). Cool Gas in High-Redshift Galaxies. *Annual Review of Astron and Astrophysics*, 51(1):105–161.

Carlstrom, J. E., Ade, P. A. R., Aird, K. A., Benson, B. A., Bleem, L. E., Busetti, S., Chang, C. L., Chauvin, E., Cho, H. M., Crawford, T. M., Crites, A. T., Dobbs, M. A., Halverson, N. W., Heimsath, S., Holzapfel, W. L., Hrubes, J. D., Joy, M., Keisler, R., Lanting, T. M., Lee, A. T., Leitch, E. M., Leong, J., Lu, W., Lueker, M., Luong-Van, D., McMahon, J. J., Mehl, J., Meyer, S. S., Mohr, J. J., Montroy, T. E., Padin, S., Plagge, T., Pryke, C., Ruhl, J. E., Schaffer, K. K., Schwan, D., Shirokoff, E., Spieler, H. G., Staniszewski, Z., Stark, A. A., Tucker, C., Vanderlinde, K., Vieira, J. D., and Williamson, R. (2011). The 10 Meter South Pole Telescope. *Publications of the Astronomical Society of the Pacific*, 123(903):568.

Casey, C. M., Narayanan, D., and Cooray, A. (2014). Dusty star-forming galaxies at high redshift. *Physics Reports*, 541(2):45–161.

Cassata, P., Le Fèvre, O., Garilli, B., Maccagni, D., Le Brun, V., Scodeggio, M., Tresse, L., Ilbert, O., Zamorani, G., Cucciati, O., Contini, T., Bielby, R., Mellier, Y., McCracken, H. J., Pollo, A., Zanichelli, A., Bardelli, S., Cappi, A., Pozzetti, L., Vergani, D., and Zucca, E. (2011). The VIMOS VLT Deep Survey: star formation rate density of Lyα emitters from a sample of 217 galaxies with spectroscopic redshifts $2 \leq z \leq 6.6$. *Astronomy & Astrophysics*, 525:A143.

Catinella, B., Saintonge, A., Janowiecki, S., Cortese, L., Davé, R., Lemonias, J. J., Cooper, A. P., Schiminovich, D., Hummels, C. B., Fabello, S., Geréb, K., Kilborn, V., and Wang, J. (2018). xGASS: total cold gas scaling relations and molecular-to-atomic gas ratios of galaxies in the local Universe. *Monthly Notices in the Royal Astronomical Society*, 476(1):875–895.

Chabrier, G. (2003). Galactic Stellar and Substellar Initial Mass Function. *Publications of the Astronomical Society of the Pacific*, 115(809):763–795.

Chabrier, G. (2005). The Initial Mass Function: From Salpeter 1955 to 2005. In Corbelli, E., Palla, F., and Zinnecker, H., editors, *The Initial Mass Function 50 Years Later*, volume 327 of *Astrophysics and Space Science Library*, page 41.

Chester, T. (1988). The Infrared Astronomical Satellite survey of the sky. In Debarbat, S., editor, *Mapping the Sky: Past Heritage and Future Directions*, volume 133, pages 341–348.

Cimatti, A., Fraternali, F., and Nipoti, C. (2019). *Introduction to Galaxy Forma-*

tion and Evolution: From Primordial Gas to Present-Day Galaxies. Cambridge University Press.

Cirasuolo, M., McLure, R. J., Dunlop, J. S., Almaini, O., Foucaud, S., and Simpson, C. (2010). A new measurement of the evolving near-infrared galaxy luminosity function out to z $\sim=$ 4: a continuing challenge to theoretical models of galaxy formation. *Monthly Notices of the Royal Astronomical Society*, 401(2):1166–1176.

Condon, J. J. and Ransom, S. M. (2018). *Essential Radio Astronomy*. Princeton, NJ: Princeton University Press.

Conselice, C. J., Bershady, M. A., Dickinson, M., and Papovich, C. (2003). A Direct Measurement of Major Galaxy Mergers at z$<\sim$3. *Astronomical Journal*, 126(3):1183–1207.

Cortes, P. C., Remijan, A., Biggs, A., Dent, B., Carpenter, J., Fomalont, E., Hales, A., Kameno, S., Mason, B., Philips, N., Saini, K., Stoehr, F., Vila-Vilaro, B., and Villard, E. (2020). ALMA Technical Handbook. In *ALMA Doc. 8.4, ver. 1.0*.

Cox, A. N. (2000). *Allen's astrophysical quantities*. New York: AIP Press.

Crosby, B. D., O'Shea, B. W., Smith, B. D., Turk, M. J., and Hahn, O. (2013). Population III Star Formation in Large Cosmological Volumes. I. Halo Temporal and Physical Environment. *Astrophysical Journal*, 773(2):108.

Daddi, E., Cimatti, A., Renzini, A., Fontana, A., Mignoli, M., Pozzetti, L., Tozzi, P., and Zamorani, G. (2004). A New Photometric Technique for the Joint Selection of Star-forming and Passive Galaxies at 1.4 $<\sim$z $<\sim$2.5. *Astrophysical Journal*, 617(2):746–764.

Davé, R., Finlator, K., and Oppenheimer, B. D. (2012). An analytic model for the evolution of the stellar, gas and metal content of galaxies. *Monthly Notices in the Royal Astronomical Society*, 421(1):98–107.

Davies, L. J. M., Bremer, M. N., Stanway, E. R., and Lehnert, M. D. (2013). The detection of FIR emission from high-redshift star-forming galaxies in the ECDF-S. *Monthly Notices of Royal Astronomical Society*, 433(3):2588–2603.

De Looze, I., Cormier, D., Lebouteiller, V., Madden, S., Baes, M., Bendo, G. J., Boquien, M., Boselli, A., Clements, D. L., Cortese, L., Cooray, A., Galametz, M., Galliano, F., Graciá-Carpio, J., Isaak, K., Karczewski, O. Ł., Parkin, T. J., Pellegrini, E. W., Rémy-Ruyer, A., Spinoglio, L., Smith, M. W. L., and Sturm, E. (2014). The applicability of far-infrared fine-structure lines as star formation rate tracers over wide ranges of metallicities and galaxy types. *Astronomy & Astrophysics*, 568:A62.

Dekel, A., Sari, R., and Ceverino, D. (2009). Formation of Massive Galaxies at High Redshift: Cold Streams, Clumpy Disks, and Compact Spheroids. *Astrophysical Journal*, 703(1):785–801.

Dekel, A., Zolotov, A., Tweed, D., Cacciato, M., Ceverino, D., and Primack, J. R.

(2013). Toy models for galaxy formation versus simulations. *Monthly Notices of the Royal Astronomical Society*, 435(2):999–1019.

Dickey, J. M. and Lockman, F. J. (1990). H I in the galaxy. *Annual Review of Astronomy and Astrophysics*, 28:215–261.

Dokuchaev, V. I., Eroshenko, Y. N., and Rubin, S. G. (2007). Origin of supermassive black holes. *arXiv e-prints*, page arXiv:0709.0070.

Dong, C., Spilker, J. S., Gonzalez, A. H., Apostolovski, Y., Aravena, M., Béthermin, M., Chapman, S. C., Chen, C.-C., Hayward, C. C., Hezaveh, Y. D., Litke, K. C., Ma, J., Marrone, D. P., Morningstar, W. R., Phadke, K. A., Reuter, C. A., Sreevani, J., Stark, A. A., Vieira, J. D., and Weiß, A. (2019). Source Structure and Molecular Gas Properties from High-resolution CO Imaging of SPT-selected Dusty Star-forming Galaxies. *Astrophysical Journal*, 873(1):50.

Downes, D. and Solomon, P. M. (1998). Rotating Nuclear Rings and Extreme Starbursts in Ultraluminous Galaxies. *Astrophysical Journal*, 507(2):615–654.

Dressler, A. and Shectman, S. A. (1987). Systematics of the 4000 Angstrom Break in the Spectra of Galaxies. *Astronomy Journal*, 94:899.

Dreyer, J. L. E. (1888). A New General Catalogue of Nebulæ and Clusters of Stars, being the Catalogue of the late Sir John F. W. Herschel, Bart, revised, corrected, and enlarged. *Memoirs of the Royal Astronomical Society*, 49:1.

Dye, S., Furlanetto, C., Swinbank, A. M., Vlahakis, C., Nightingale, J. W., Dunne, L., Eales, S. A., Smail, I., Oteo, I., Hunter, T., Negrello, M., Dannerbauer, H., Ivison, R. J., Gavazzi, R., Cooray, A., and van der Werf, P. (2015). Revealing the complex nature of the strong gravitationally lensed system H-ATLAS J090311.6+003906 using ALMA. *Monthly Notices of the Royal Astronomical Society*, 452(3):2258–2268.

Ebert, R. (1955). Über die Verdichtung von H I-Gebieten. Mit 5 Textabbildungen. *Zeitschrift fur Astrophysik*, 37:217.

Emonts, B. H. C., Norris, R. P., Feain, I., Mao, M. Y., Ekers, R. D., Miley, G., Seymour, N., Röttgering, H. J. A., Villar-Martín, M., Sadler, E. M., Carilli, C. L., Mahony, E. K., de Breuck, C., Stroe, A., Pentericci, L., van Moorsel, G. A., Drouart, G., Ivison, R. J., Greve, T. R., Humphrey, A., Wylezalek, D., and Tadhunter, C. N. (2014). CO(1-0) survey of high-z radio galaxies: alignment of molecular halo gas with distant radio sources. *Monthly Notices of the RAS*, 438(4):2898–2915.

Event Horizon Telescope Collaboration and Akiyama, K. e. a. (2019). First M87 Event Horizon Telescope Results. I. The Shadow of the Supermassive Black Hole. *Astrophysical Journal, Letters*, 875(1):L1.

Faber, S. M. and Jackson, R. E. (1976). Velocity dispersions and mass-to-light ratios for elliptical galaxies. *Astrophysical Journal*, 204:668–683.

Fan, X., Strauss, M. A., Becker, R. H., White, R. L., Gunn, J. E., Knapp, G. R.,

Richards, G. T., Schneider, D. P., Brinkmann, J., and Fukugita, M. (2006). Constraining the Evolution of the Ionizing Background and the Epoch of Reionization with z∼6 Quasars. II. A Sample of 19 Quasars. *Astrophysical Journal*, 132(1):117–136.

Fensch, J., Renaud, F., Bournaud, F., Duc, P. A., Agertz, O., Amram, P., Combes, F., Di Matteo, P., Elmegreen, B., Emsellem, E., Jog, C. J., Perret, V., Struck, C., and Teyssier, R. (2017). High-redshift major mergers weakly enhance star formation. *Monthly Notices of the Royal Astronomical Society*, 465(2):1934–1949.

Finlator, K. (2017). Gas Accretion and Galactic Chemical Evolution: Theory and Observations. In Fox, A. and Davé, R., editors, *Gas Accretion onto Galaxies*, volume 430 of *Astrophysics and Space Science Library*, page 221.

Finlator, K. and Davé, R. (2008). The origin of the galaxy mass-metallicity relation and implications for galactic outflows. *Monthly Notices in the Royal Astronomical Society*, 385(4):2181–2204.

Fisher, D., Illingworth, G., and Franx, M. (1995). Kinematics of 13 Brightest Cluster Galaxies. *Astrophysical Journal*, 438:539.

Foreman-Mackey, D., Hogg, D. W., Lang, D., and Goodman, J. (2013). emcee: The MCMC Hammer. *Publications of the Astronomical Society of the Pacific*, 125(925):306.

Fujimoto, S., Silverman, J. D., Bethermin, M., Ginolfi, M., Jones, G. C., Le Fèvre, O., Dessauges-Zavadsky, M., Rujopakarn, W., Faisst, A. L., Fudamoto, Y., Cassata, P., Morselli, L., Maiolino, R., Schaerer, D., Capak, P., Yan, L., Vallini, L., Toft, S., Loiacono, F., Zamorani, G., Talia, M., Narayanan, D., Hathi, N. P., Lemaux, B. C., Boquien, M., Amorin, R., Ibar, E., Koekemoer, A. M., Méndez-Hernández, H., Bardelli, S., Vergani, D., Zucca, E., Romano, M., and Cimatti, A. (2020). The ALPINE-ALMA [C II] Survey: Size of Individual Star-forming Galaxies at z = 4-6 and Their Extended Halo Structure. *Astrophysical Journal*, 900(1):1.

Gabor, J. M., Davé, R., Finlator, K., and Oppenheimer, B. D. (2010). How is star formation quenched in massive galaxies? *Monthly Notices of the Royal Astronomical Society*, 407(2):749–771.

Galaxy formation (1998). *Galaxy formation*. Springer.

Galilei, G. (1610). *Sidereus Nuncius*. Thomas Baglioni.

Gardner, J. P., Mather, J. C., Clampin, M., Doyon, R., Greenhouse, M. A., Hammel, H. B., Hutchings, J. B., Jakobsen, P., Lilly, S. J., Long, K. S., Lunine, J. I., McCaughrean, M. J., Mountain, M., Nella, J., Rieke, G. H., Rieke, M. J., Rix, H.-W., Smith, E. P., Sonneborn, G., Stiavelli, M., Stockman, H. S., Windhorst, R. A., and Wright, G. S. (2006). The James Webb Space Telescope. *Space Science Reviews*, 123(4):485–606.

Genzel, R., Tacconi, L. J., Combes, F., Bolatto, A., Neri, R., Sternberg, A., Cooper, M. C., Bouché, N., Bournaud, F., Burkert, A., Comerford, J., Cox, P., Davis, M.,

Förster Schreiber, N. M., Garcia-Burillo, S., Gracia-Carpio, J., Lutz, D., Naab, T., Newman, S., Saintonge, A., Shapiro, K., Shapley, A., and Weiner, B. (2012). The Metallicity Dependence of the CO $\rightarrow$ H_2 Conversion Factor in z >= 1 Star-forming Galaxies. *Astrophysical Journal*, 746(1):69.

Genzel, R., Tacconi, L. J., Lutz, D., Saintonge, A., Berta, S., Magnelli, B., Combes, F., García-Burillo, S., Neri, R., Bolatto, A., Contini, T., Lilly, S., Boissier, J., Boone, F., Bouché, N., Bournaud, F., Burkert, A., Carollo, M., Colina, L., Cooper, M. C., Cox, P., Feruglio, C., Förster Schreiber, N. M., Freundlich, J., Gracia-Carpio, J., Juneau, S., Kovac, K., Lippa, M., Naab, T., Salome, P., Renzini, A., Sternberg, A., Walter, F., Weiner, B., Weiss, A., and Wuyts, S. (2015). Combined CO and Dust Scaling Relations of Depletion Time and Molecular Gas Fractions with Cosmic Time, Specific Star-formation Rate, and Stellar Mass. *Astrophysical Journal*, 800(1):20.

Gnedin, N. Y. (2000). Effect of Reionization on Structure Formation in the Universe. *Astrophysical Journal*, 542(2):535–541.

Gnedin, N. Y. and Ostriker, J. P. (1997). Reionization of the Universe and the Early Production of Metals. *Astrophysical Journal*, 486(2):581–598.

Graham, A. W. (2019). A galaxy classification grid that better recognizes early-type galaxy morphology. *Monthly Notices of the Royal Astronomical Society*, 487(4):4995–5009.

Greve, T. R., Leonidaki, I., Xilouris, E. M., Weiß, A., Zhang, Z. Y., van der Werf, P., Aalto, S., Armus, L., Díaz-Santos, T., Evans, A. S., Fischer, J., Gao, Y., González-Alfonso, E., Harris, A., Henkel, C., Meijerink, R., Naylor, D. A., Smith, H. A., Spaans, M., Stacey, G. J., Veilleux, S., and Walter, F. (2014). Star Formation Relations and CO Spectral Line Energy Distributions across the J-ladder and Redshift. *Astrophysical Journal*, 794(2):142.

Gruppioni, C. e. a. (2013). The Herschel PEP/HerMES luminosity function - I. Probing the evolution of PACS selected Galaxies to z $\simeq$ 4. *Monthly Notices of the Royal Astronomical Society*, 432(1):23–52.

Gunn, J. E. and Peterson, B. A. (1965). On the Density of Neutral Hydrogen in Intergalactic Space. *Astrophysical Journal*, 142:1633–1636.

Guth, A. H. (1981). Inflationary universe: A possible solution to the horizon and flatness problems. *Physical Review D*, 23(2):347–356.

Heckman, T. (2000). Starburst Galaxies. In Murdin, P., editor, *Encyclopedia of Astronomy and Astrophysics*, page 1583. Bristol: Institute of Physics Publishing.

Hezaveh, Y. D., Marrone, D. P., Fassnacht, C. D., Spilker, J. S., Vieira, J. D., Aguirre, J. E., Aird, K. A., Aravena, M., Ashby, M. L. N., Bayliss, M., Benson, B. A., Bleem, L. E., Bothwell, M., Brodwin, M., Carlstrom, J. E., Chang, C. L., Chapman, S. C., Crawford, T. M., Crites, A. T., De Breuck, C., de Haan, T., Dobbs, M. A., Fomalont, E. B., George, E. M., Gladders, M. D., Gonzalez, A. H., Greve, T. R., Halverson, N. W., High, F. W., Holder, G. P., Holzapfel, W. L.,

Hoover, S., Hrubes, J. D., Husband, K., Hunter, T. R., Keisler, R., Lee, A. T., Leitch, E. M., Lueker, M., Luong-Van, D., Malkan, M., McIntyre, V., McMahon, J. J., Mehl, J., Menten, K. M., Meyer, S. S., Mocanu, L. M., Murphy, E. J., Natoli, T., Padin, S., Plagge, T., Reichardt, C. L., Rest, A., Ruel, J., Ruhl, J. E., Sharon, K., Schaffer, K. K., Shaw, L., Shirokoff, E., Stalder, B., Staniszewski, Z., Stark, A. A., Story, K., Vanderlinde, K., Weiß, A., Welikala, N., and Williamson, R. (2013). ALMA Observations of SPT-discovered, Strongly Lensed, Dusty, Star-forming Galaxies. *Astrophysical Journal*, 767:132.

Högbom, J. A. (1974). Aperture Synthesis with a Non-Regular Distribution of Interferometer Baselines. *Astronomy and Astrophysics, Supplement*, 15:417.

Hopkins, P. F., Hernquist, L., Cox, T. J., Di Matteo, T., Robertson, B., and Springel, V. (2006). A Unified, Merger-driven Model of the Origin of Starbursts, Quasars, the Cosmic X-Ray Background, Supermassive Black Holes, and Galaxy Spheroids. *Astrophysical Journal Supplement*, 163(1):1–49.

Huang, Y. D. (2019). The ALMA Band 1 receiver. In *ALMA Development Workshop*, page 23.

Hubble, E. (1929). A Relation between Distance and Radial Velocity among Extra-Galactic Nebulae. *Contributions from the Mount Wilson Observatory*, 3:23–28.

Hughes, D. H., Serjeant, S., Dunlop, J., Rowan-Robinson, M., Blain, A., Mann, R. G., Ivison, R., Peacock, J., Efstathiou, A., Gear, W., Oliver, S., Lawrence, A., Longair, M., Goldschmidt, P., and Jenness, T. (1998). High-redshift star formation in the Hubble Deep Field revealed by a submillimetre-wavelength survey. *Nature*, 394(6690):241–247.

Ilbert, O., Arnouts, S., Le Floc'h, E., Aussel, H., Bethermin, M., Capak, P., Hsieh, B. C., Kajisawa, M., Karim, A., Le Fèvre, O., Lee, N., Lilly, S., McCracken, H. J., Michel-Dansac, L., Moutard, T., Renzini, M. A., Salvato, M., Sanders, D. B., Scoville, N., Sheth, K., Silverman, J. D., Smolčić, V., Taniguchi, Y., and Tresse, L. (2015). Evolution of the specific star formation rate function at z< 1.4 Dissecting the mass-SFR plane in COSMOS and GOODS. *Astronomy & Astrophysics*, 579:A2.

Iono, D., Wilson, C. D., Yun, M. S., Baker, A. J., Petitpas, G. R., Peck, A. B., Krips, M., Cox, T. J., Matsushita, S., Mihos, J. C., and Pihlstrom, Y. (2009). Luminous Infrared Galaxies with the Submillimeter Array. II. Comparing the CO (3-2) Sizes and Luminosities of Local and High-Redshift Luminous Infrared Galaxies. *Astrophysical Journal*, 695(2):1537–1549.

Jeans, J. H. (1902). The Stability of a Spherical Nebula. *Philosophical Transactions of the Royal Society of London Series A*, 199:1–53.

Kant, I. (1755). *Allgemeine Naturgeschichte und Theorie des Himmels*. Johann Friederich Petersen.

Karl, S. J., Naab, T., Johansson, P. H., Kotarba, H., Boily, C. M., Renaud, F.,

and Theis, C. (2010). One Moment in Time—Modeling Star Formation in the Antennae. *Astrophysical Journal, Letters*, 715(2):L88–L93.

Kaviraj, S., Devriendt, J., Dubois, Y., Slyz, A., Welker, C., Pichon, C., Peirani, S., and Le Borgne, D. (2015). Galaxy merger histories and the role of merging in driving star formation at z $>$ 1. *Monthly Notices of the Royal Astronomical Society*, 452(3):2845–2850.

Kennicutt, Robert C., J. (1992). The Integrated Spectra of Nearby Galaxies: General Properties and Emission-Line Spectra. *Astrophysical Journal*, 388:310.

Kennicutt, Robert C., J. (1998). Star Formation in Galaxies Along the Hubble Sequence. *Annual Review of Astronomy and Astrophysics*, 36:189–232.

Khochfar, S. and Burkert, A. (2001). Redshift Evolution of the Merger Fraction of Galaxies in Cold Dark Matter Cosmologies. *Astrophysical Journal*, 561(2):517–520.

Kiehbadroudinezhad, S., Noordin, N., Sali, A., and Abidin, Z. (2014). Optimization of an antenna array using genetic algorithms. *Astronomical Journal*, 147:147.

Kilbinger, M. (2015). Cosmology with cosmic shear observations: a review. *Reports on Progress in Physics*, 78(8):086901.

Kirby, E. N., Boylan-Kolchin, M., Cohen, J. G., Geha, M., Bullock, J. S., and Kaplinghat, M. (2013). Segue 2: The Least Massive Galaxy. *Astrophysical Journal*, 770(1):16.

Koopmans, L. V. E., Bolton, A., Treu, T., Czoske, O., Auger, M. W., Barnabè, M., Vegetti, S., Gavazzi, R., Moustakas, L. A., and Burles, S. (2009). The Structure and Dynamics of Massive Early-Type Galaxies: On Homology, Isothermality, and Isotropy Inside One Effective Radius. *Astrophysical Journal Letters*, 703(1):L51–L54.

Koopmans, L. V. E., Treu, T., Bolton, A. S., Burles, S., and Moustakas, L. A. (2006). The Sloan Lens ACS Survey. III. The Structure and Formation of Early-Type Galaxies and Their Evolution since z $\sim$1. *Astrophysical Journal*, 649(2):599–615.

Kormendy, J. and Ho, L. C. (2013). Coevolution (Or Not) of Supermassive Black Holes and Host Galaxies. *Annual Review of Astronomy & Astrophysics*, 51(1):511–653.

Kovács, A., Chapman, S. C., Dowell, C. D., Blain, A. W., Ivison, R. J., Smail, I., and Phillips, T. G. (2006). SHARC-2 350 μm Observations of Distant Submillimeter-selected Galaxies. *Astrophysical Journal*, 650(2):592–603.

Kroupa, P. (2002). The Initial Mass Function of Stars: Evidence for Uniformity in Variable Systems. *Science*, 295(5552):82–91.

Krumholz, M. R., Dekel, A., and McKee, C. F. (2012). A Universal, Local Star Formation Law in Galactic Clouds, nearby Galaxies, High-redshift Disks, and Starbursts. *Astrophysical Journal*, 745(1):69.

Kuhlen, M., Krumholz, M., Madau, P., Smith, B., and Wise, J. (2012). Dwarf galaxy formation with h2-regulated star formation. *The Astrophysical Journal*, 749:36.

Larson, R. B. (1981). Turbulence and star formation in molecular clouds. *Monthly Notices in the Royal Astronomical Society*, 194:809–826.

Larson, R. B. (1998). Early star formation and the evolution of the stellar initial mass function in galaxies. *Monthly Notices of the Royal Astronomical Society*, 301(2):569–581.

Law, D. R., Steidel, C. C., Erb, D. K., Larkin, J. E., Pettini, M., Shapley, A. E., and Wright, S. A. (2009). The Kiloparsec-scale Kinematics of High-redshift Star-forming Galaxies. *Astrophysical Journal*, 697(2):2057–2082.

Lazio, T. J. W., Brisken, W., Bouman, K., Doeleman, S., Falcke, H., Iguchi, S., Kovalev, Y. Y., Lonsdale, C. J., Shen, Z., Zensus, A., and Beasley, A. J. (2020). Space VLBI 2020: Science and Technology Futures Conference Summary. *arXiv e-prints*, page arXiv:2005.12767.

Lilly, S. J., Tresse, L., Hammer, F., Crampton, D., and Le Fevre, O. (1995). The Canada-France Redshift Survey. VI. Evolution of the Galaxy Luminosity Function to Z approximately 1. *Astrophysical Journal*, 455:108.

Lin, C. C. and Shu, F. H. (1964). On the Spiral Structure of Disk Galaxies. *Astrophysical Journal*, 140:646.

Linde, A. D. (1982). A new inflationary universe scenario: A possible solution of the horizon, flatness, homogeneity, isotropy and primordial monopole problems. *Physics Letters B*, 108(6):389–393.

Lintott, C. J., Schawinski, K., Slosar, A., Land, K., Bamford, S., Thomas, D., Raddick, M. J., Nichol, R. C., Szalay, A., Andreescu, D., Murray, P., and Vandenberg, J. (2008). Galaxy Zoo: morphologies derived from visual inspection of galaxies from the Sloan Digital Sky Survey. *Monthly Notices of the Royal Astronomical Society*, 389(3):1179–1189.

Lofthouse, E. K., Kaviraj, S., Conselice, C. J., Mortlock, A., and Hartley, W. (2017). Major mergers are not significant drivers of star formation or morphological transformation around the epoch of peak cosmic star formation. *Monthly Notices of the Royal Astronomical Society*, 465(3):2895–2900.

Lu, L., Sargent, W. L. W., Barlow, T. A., and Rauch, M. (1998). The Metal Contents of Very Low Column Density Lyman-alpha Clouds: Implications for the Origin of Heavy Elements in the Intergalactic Medium. *arXiv e-prints*, pages astro–ph/9802189.

Ma, J., Gonzalez, A. H., Spilker, J. S., Strandet, M., Ashby, M. L. N., Aravena, M., Béthermin, M., Bothwell, M. S., de Breuck, C., Brodwin, M., Chapman, S. C., Fassnacht, C. D., Greve, T. R., Gullberg, B., Hezaveh, Y., Malkan, M., Marrone, D. P., Saliwanchik, B. R., Vieira, J. D., Weiss, A., and Welikala, N. (2015). Stellar

Masses and Star Formation Rates of Lensed, Dusty, Star-forming Galaxies from the SPT Survey. *Astrophysical Journal*, 812(1):88.

Madau, P. and Dickinson, M. (2014). Cosmic Star-Formation History. *Annual Review of Astronomy and Astrophysics*, 52:415–486.

Madau, P., Ferguson, H. C., Dickinson, M. E., Giavalisco, M., Steidel, C. C., and Fruchter, A. (1996). High-redshift galaxies in the Hubble Deep Field: colour selection and star formation history to z∼4. *Monthly Notices in the Royal Astronomical Society*, 283(4):1388–1404.

Magnelli, B., Lutz, D., Berta, S., Altieri, B., Andreani, P., Aussel, H., Castañeda, H., Cava, A., Cepa, J., Cimatti, A., Daddi, E., Dannerbauer, H., Dominguez, H., Elbaz, D., Förster Schreiber, N., Genzel, R., Grazian, A., Gruppioni, C., Magdis, G., Maiolino, R., Nordon, R., Pérez Fournon, I., Pérez García, I., Poglitsch, A., Popesso, P., Pozzi, F., Riguccini, L., Rodighiero, G., Saintonge, A., Santini, P., Sanchez-Portal, M., Shao, L., Sturm, E., Tacconi, L., Valtchanov, I., Wieprecht, E., and Wiezorrek, E. (2010). Far-infrared properties of submillimeter and optically faint radio galaxies. *Astronomy & Astrophysics*, 518:L28.

Man, A. W. S., Zirm, A. W., and Toft, S. (2016). Resolving the Discrepancy of Galaxy Merger Fraction Measurements at z $\sim$ 0-3. *Astrophysical Journal*, 830(2):89.

Mancuso, C., Lapi, A., Shi, J., Cai, Z. Y., Gonzalez-Nuevo, J., Béthermin, M., and Danese, L. (2016). The Main Sequences of Star-forming Galaxies and Active Galactic Nuclei at High Redshift. *Astrophysical Journal*, 833(2):152.

Manning, C. and Spinrad, H. (2001). The Dust Temperature of the "Dusty" Radio Galaxy MG 1019+0535: Evidence for an Outflow. *Astronomical Journal*, 122(1):113–120.

Mao, R.-Q., Schulz, A., Henkel, C., Mauersberger, R., Muders, D., and Dinh-V-Trung (2010). An Extragalactic ^{12}CO J = 3-2 Survey with the Heinrich Hertz Telescope. *Astrophysical Journal*, 724(2):1336–1356.

Mashian, N., Sturm, E., Sternberg, A., Janssen, A., Hailey-Dunsheath, S., Fischer, J., Contursi, A., González-Alfonso, E., Graciá-Carpio, J., Poglitsch, A., Veilleux, S., Davies, R., Genzel, R., Lutz, D., Tacconi, L., Verma, A., Weiß, A., Polisensky, E., and Nikola, T. (2015). High-J CO Sleds in Nearby Infrared Bright Galaxies Observed By Herschel/PACS. *Astrophysical Journal*, 802(2):81.

McCarthy, D. D. and Seidelmann, P. K. (2018). *Time and Cosmology*, page 123–130. Cambridge University Press, 2 edition.

McMullin, J. P., Waters, B., Schiebel, D., Young, W., and Golap, K. (2007). CASA Architecture and Applications. In Shaw, R. A., Hill, F., and Bell, D. J., editors, *Astronomical Data Analysis Software and Systems XVI*, volume 376 of *Astronomical Society of the Pacific Conference Series*, page 127.

Messias, H., Afonso, J. M., Salvato, M., Mobasher, B., and Hopkins, A. M. (2014). The dependency of AGN infrared colour-selection on source luminosity and ob-

scuration. An observational perspective in CDFS and COSMOS. *Astronomy & Astrophysics*, 562:A144.

Messier, C. (1781). Catalogue des Nébuleuses et des Amas d'Étoiles (Catalog of Nebulae and Star Clusters). Connoissance des Temps ou des Mouvements Célestes.

Minchev, I. and Famaey, B. (2010). A New Mechanism for Radial Migration in Galactic Disks: Spiral-Bar Resonance Overlap. *Astrophysical Journal*, 722(1):112–121.

Minissale, M., Dulieu, F., Cazaux, S., and Hocuk, S. (2016). Dust as interstellar catalyst. I. Quantifying the chemical desorption process. *Astronomy and Astrophysics*, 585:A24.

Mo, H., van den Bosch, F. C., and White, S. (2010). *Galaxy Formation and Evolution*. Cambridge University Press.

Monnier, J. D., Berger, J.-P., Le Bouquin, J.-B., Tuthill, P. G., Wittkowski, M., Grellmann, R., Müller, A., Renganswany, S., Hummel, C., Hofmann, K.-H., Schertl, D., Weigelt, G., Young, J., Buscher, D., Sanchez-Bermudez, J., Alberdi, A., Schoedel, R., Köhler, R., Soulez, F., Thiébaut, É., Kluska, J., Malbet, F., Duvert, G., Kraus, S., Kloppenborg, B. K., Baron, F., de Wit, W.-J., Rivinius, T., and Merand, A. (2014). The 2014 interferometric imaging beauty contest. In Rajagopal, J. K., Creech-Eakman, M. J., and Malbet, F., editors, *Optical and Infrared Interferometry IV*, volume 9146 of *Society of Photo-Optical Instrumentation Engineers (SPIE) Conference Series*, page 91461Q.

Moré, J. J. (1978). The Levenberg-Marquardt algorithm: Implementation and theory. In *Lecture Notes in Mathematics*, volume 630, pages 105–116. Springer Verlag.

Mundy, C. J., Conselice, C. J., Duncan, K. J., Almaini, O., Häußler, B., and Hartley, W. G. (2017). A consistent measure of the merger histories of massive galaxies using close-pair statistics - I. Major mergers at $z < 3.5$. *Monthly Notices of the Royal Astronomical Society*, 470(3):3507–3531.

Murray, N. (2011). Star Formation Efficiencies and Lifetimes of Giant Molecular Clouds in the Milky Way. *Astrophysical Journal*, 729(2):133.

Mutch, S. J., Croton, D. J., and Poole, G. B. (2011). The Mid-life Crisis of the Milky Way and M31. *Astrophysical Journal*, 736(2):84.

Nan, R., Li, D., Jin, C., Wang, Q., Zhu, L., Zhu, W., Zhang, H., Yue, Y., and Qian, L. (2011). The Five-Hundred Aperture Spherical Radio Telescope (fast) Project. *International Journal of Modern Physics D*, 20(6):989–1024.

National Radio Astronomy Observatory (2012). Very Large Array.

Nersesian, A., Dobbels, W., Xilouris, E. M., Baes, M., Bianchi, S., Casasola, V., Clark, C. J. R., De Looze, I., Galliano, F., Madden, S. C., Mosenkov, A. V., Paspaliaris, E.-D., and Trčka, A. (2021). Probing the spectral shape of dust emission with the DustPedia galaxy sample. *Monthly Notices of the Royal Astronomical Society*, 506(3):3986–3995.

Omont, A. (2007). Molecules in galaxies. *Reports on Progress in Physics*, 70(7):1099–1176.

Patris, J. (2010). Preparing astronomical observations and observing with ohp facilities. *EPJ Web of Conferences*, 9:217.

Pearson, W. J., Wang, L., Alpaslan, M., Baldry, I., Bilicki, M., Brown, M. J. I., Grootes, M. W., Holwerda, B. W., Kitching, T. D., Kruk, S., and van der Tak, F. F. S. (2019). Effect of galaxy mergers on star-formation rates. *Astronomy and Astrophysics*, 631:A51.

Penzias, A. A. and Wilson, R. W. (1965). A Measurement of Excess Antenna Temperature at 4080 Mc/s. *Astrophysical Journal*, 142:419–421.

Planck Collaboration and Ade, P. A. R. e. a. (2016). Planck 2015 results. XIII. Cosmological parameters. *Astronomy and Astrophysics*, 594:A13.

Plutarch (2006). *The Complete Works Volume 3: Essays and Miscellanies*. Echo Library.

Rybak, M., Hodge, J. A., Vegetti, S., van der Werf, P., Andreani, P., Graziani, L., and McKean, J. P. (2020). Full of Orions: a 200-pc mapping of the interstellar medium in the redshift-3 lensed dusty star-forming galaxy SDP.81. *Monthly Notices of the Royal Astronomical Society*, 494(4):5542–5567.

Salpeter, E. E. (1955). The Luminosity Function and Stellar Evolution. *Astrophysical Journal*, 121:161.

Sancisi, R., Fraternali, F., Oosterloo, T., and van der Hulst, T. (2008). Cold gas accretion in galaxies. *Astronomy & Astrophysics Reviews*, 15(3):189–223.

Sanders, D. B. (1997). Luminous Infrared Galaxies. In Franco, J., Terlevich, R., and Serrano, A., editors, *Revista Mexicana de Astronomia y Astrofisica Conference Series*, volume 6 of *Revista Mexicana de Astronomia y Astrofisica Conference Series*, page 42.

Scalo, J. M. (1986). The Stellar Initial Mass Function. *Fundamentals of Cosmic Physics*, 11:1–278.

Schaerer, D. (2003). The transition from Population III to normal galaxies: Lyalpha and He II emission and the ionising properties of high redshift starburst galaxies. *Astronomy and Astrophysics*, 397:527–538.

Schechter, P. (1976). An analytic expression for the luminosity function for galaxies. *Astrophysical Journal*, 203:297–306.

Schmidt, M. (1959). The Rate of Star Formation. *Astrophysical Journal*, 129:243.

Schneider, P. (2006). *Extragalactic Astronomy and Cosmology*. Springer-Verlag.

Scoville, N., Lee, N., Vanden Bout, P., Diaz-Santos, T., Sanders, D., Darvish, B., Bongiorno, A., Casey, C. M., Murchikova, L., Koda, J., Capak, P., Vlahakis, C., Ilbert, O., Sheth, K., Morokuma-Matsui, K., Ivison, R. J., Aussel, H., Laigle, C., McCracken, H. J., Armus, L., Pope, A., Toft, S., and Masters, D. (2017).

Evolution of Interstellar Medium, Star Formation, and Accretion at High Redshift. *Astrophysical Journal*, 837(2):150.

Sellwood, J. A. and Wilkinson, A. (1993). Dynamics of barred galaxies. *Reports on Progress in Physics*, 56(2):173–256.

Shapley, H. and Curtis, H. D. (1921). The Scale of the Universe. *Bulletin of the National Research Council*, 2(11):171–217.

Shen, S., Mo, H. J., White, S. D. M., Blanton, M. R., Kauffmann, G., Voges, W., Brinkmann, J., and Csabai, I. (2003). The size distribution of galaxies in the Sloan Digital Sky Survey. *Monthly Notices of the Royal Astronomical Society*, 343(3):978–994.

Sherman, S., Jogee, S., Florez, J., Finkelstein, S. L., Ciardullo, R., Wold, I., Stevans, M. L., Kawinwanichakij, L., Papovich, C., and Gronwall, C. (2021). The shape and scatter of the galaxy main sequence for massive galaxies at cosmic noon. *Monthly Notices of the RAS*, 505(1):947–962.

Shu, F. H. (1992). *The physics of astrophysics. Volume II: Gas dynamics.* University Science Books.

Silverman, J. D., Rujopakarn, W., Daddi, E., Renzini, A., Rodighiero, G., Liu, D., Puglisi, A., Sargent, M., Mancini, C., Kartaltepe, J., Kashino, D., Koekemoer, A., Arimoto, N., Béthermin, M., Jin, S., Magdis, G., Nagao, T., Onodera, M., Sanders, D., and Valentino, F. (2018). The Molecular Gas Content and Fuel Efficiency of Starbursts at z $\sim$ 1.6 with ALMA. *Astrophysical Journal*, 867(2):92.

Smail, I., Owen, F. N., Morrison, G. E., Keel, W. C., Ivison, R. J., and Ledlow, M. J. (2002). The Diversity of Extremely Red Objects. *Astrophysical Journal*, 581(2):844–864.

Smith, R. W. (1982). Book-Review - the Expanding Universe - Astronomy's Great Debate 1900-1931. *Journal for the History of Astronomy*, 13:145.

Soifer, B. T., Rowan-Robinson, M., Houck, J. R., de Jong, T., Neugebauer, G., Aumann, H. H., Beichman, C. A., Boggess, N., Clegg, P. E., Emerson, J. P., Gillett, F. C., Habing, H. J., Hauser, M. G., Low, F. J., Miley, G., and Young, E. (1984). Infrared galaxies in the IRAS minisurvey. *Astrophysical Journal Letters*, 278:L71–L74.

Solimano, M., González-López, J., Barrientos, L. F., Aravena, M., López, S., Tejos, N., Sharon, K., Dahle, H., Bayliss, M., Ledoux, C., Rigby, J. R., and Gladders, M. (2021). Molecular gas budget and characterization of intermediate-mass star-forming galaxies at z $\approx$ 2-3. *Astronomy and Astrophysics*, 655:A42.

Solomon, P. M., Downes, D., and Radford, S. J. E. (1992). Warm Molecular Gas in the Primeval Galaxy IRAS 10214+4724. *Astrophysical Journal, Letters*, 398:L29.

Soltan, A. (1982). Masses of quasars. *Monthly Notices of the Royal Astronomical Society*, 200:115–122.

Somerville, R. S., Hopkins, P. F., Cox, T. J., Robertson, B. E., and Hernquist, L. (2008). A semi-analytic model for the co-evolution of galaxies, black holes and active galactic nuclei. *Monthly Notices of the Royal Astronomical Society*, 391(2):481–506.

Sparke, L. S. and Gallagher, John S., I. (2007). *Galaxies in the Universe: An Introduction*. Cambridge University Press, 2 edition.

Spiegelhalter, D. J., Best, N. G., Carlin, B. P., and van der Linde, A. (2002). Bayesian measures of model complexity and fit. *Journal of the Royal Statistical Society. Series B (Statistical Methodology)*, 64(4):583–639.

Spilker, J. S., Marrone, D. P., Aravena, M., Béthermin, M., Bothwell, M. S., Carlstrom, J. E., Chapman, S. C., Crawford, T. M., de Breuck, C., Fassnacht, C. D., Gonzalez, A. H., Greve, T. R., Hezaveh, Y., Litke, K., Ma, J., Malkan, M., Rotermund, K. M., Strandet, M., Vieira, J. D., Weiss, A., and Welikala, N. (2016). ALMA Imaging and Gravitational Lens Models of South Pole Telescope—Selected Dusty, Star-Forming Galaxies at High Redshifts. *Astrophysical Journal*, 826:112.

Springel, V., White, S. D. M., Jenkins, A., Frenk, C. S., Yoshida, N., Gao, L., Navarro, J., Thacker, R., Croton, D., Helly, J., Peacock, J. A., Cole, S., Thomas, P., Couchman, H., Evrard, A., Colberg, J., and Pearce, F. (2005). Simulations of the formation, evolution and clustering of galaxies and quasars. *Nature*, 435(7042):629–636.

Stahler, S. W. and Palla, F. (2004). *The Formation of Stars*. Wiley-VCH.

Starobinsky, A. A. (1980). A new type of isotropic cosmological models without singularity. *Physics Letters B*, 91(1):99–102.

Strandet, M. L., Weiss, A., Vieira, J. D., de Breuck, C., Aguirre, J. E., Aravena, M., Ashby, M. L. N., Béthermin, M., Bradford, C. M., Carlstrom, J. E., Chapman, S. C., Crawford, T. M., Everett, W., Fassnacht, C. D., Furstenau, R. M., Gonzalez, A. H., Greve, T. R., Gullberg, B., Hezaveh, Y., Kamenetzky, J. R., Litke, K., Ma, J., Malkan, M., Marrone, D. P., Menten, K. M., Murphy, E. J., Nadolski, A., Rotermund, K. M., Spilker, J. S., Stark, A. A., and Welikala, N. (2016). The Redshift Distribution of Dusty Star-forming Galaxies from the SPT Survey. *Astrophysical Journal*, 822(2):80.

Strateva, I., Ivezić, Ž., Knapp, G. R., Narayanan, V. K., Strauss, M. A., Gunn, J. E., Lupton, R. H., Schlegel, D., Bahcall, N. A., Brinkmann, J., Brunner, R. J., Budavári, T., Csabai, I., Castander, F. J., Doi, M., Fukugita, M., Győry, Z., Hamabe, M., Hennessy, G., Ichikawa, T., Kunszt, P. Z., Lamb, D. Q., McKay, T. A., Okamura, S., Racusin, J., Sekiguchi, M., Schneider, D. P., Shimasaku, K., and York, D. (2001). Color Separation of Galaxy Types in the Sloan Digital Sky Survey Imaging Data. *Astronomical Journal*, 122(4):1861–1874.

Sutherland, R. S. and Dopita, M. A. (1993). Cooling Functions for Low-Density Astrophysical Plasmas. *Astrophysical Journal Supplement*, 88:253.

Suzuki, N. and Fukugita, M. (2018). Blackbody Stars. *Astronomy Journal*, 156(5):219.

Swinbank, A. M., Papadopoulos, P. P., Cox, P., Krips, M., Ivison, R. J., Smail, I., Thomson, A. P., Neri, R., Richard, J., and Ebeling, H. (2011). The Interstellar Medium in Distant Star-forming Galaxies: Turbulent Pressure, Fragmentation, and Cloud Scaling Relations in a Dense Gas Disk at z = 2.3. *Astrophysical Journal*, 742(1):11.

Tacconi, L. J., Genzel, R., Saintonge, A., Combes, F., García-Burillo, S., Neri, R., Bolatto, A., Contini, T., Förster Schreiber, N. M., Lilly, S., Lutz, D., Wuyts, S., Accurso, G., Boissier, J., Boone, F., Bouché, N., Bournaud, F., Burkert, A., Carollo, M., Cooper, M., Cox, P., Feruglio, C., Freundlich, J., Herrera-Camus, R., Juneau, S., Lippa, M., Naab, T., Renzini, A., Salome, P., Sternberg, A., Tadaki, K., Übler, H., Walter, F., Weiner, B., and Weiss, A. (2018). PHIBSS: Unified Scaling Relations of Gas Depletion Time and Molecular Gas Fractions. *Astrophysical Journal*, 853(2):179.

Tacconi, L. J., Neri, R., Genzel, R., Combes, F., Bolatto, A., Cooper, M. C., Wuyts, S., Bournaud, F., Burkert, A., Comerford, J., Cox, P., Davis, M., Förster Schreiber, N. M., García-Burillo, S., Gracia-Carpio, J., Lutz, D., Naab, T., Newman, S., Omont, A., Saintonge, A., Shapiro Griffin, K., Shapley, A., Sternberg, A., and Weiner, B. (2013). Phibss: Molecular Gas Content and Scaling Relations in z ∼1-3 Massive, Main-sequence Star-forming Galaxies. *Astrophysical Journal*, 768(1):74.

Talia, M., Cimatti, A., Mignoli, M., Pozzetti, L., Renzini, A., Kurk, J., and Halliday, C. (2014). Listening to galaxies tuning at z ∼2.5-3.0: The first strikes of the Hubble fork. *Astronomy & Astrophysics*, 562:A113.

Testi, L. (2010). Science with ALMA. *Memorie della Societa Astronomica Italiana Supplementi*, 14:90.

The American Heritage (2022). Telescope.

Thiébaut, É. and Young, J. (2017). Principles of image reconstruction in optical interferometry: tutorial. *Journal of the Optical Society of America A*, 34(6):904.

Thompson, A. R., Moran, J. M., and Swenson, G. W. (2017). *Van Cittert–Zernike Theorem, Spatial Coherence, and Scattering*, pages 767–786. Springer International Publishing, Cham.

Toomre, A. (1964). On the gravitational stability of a disk of stars. *Astrophysical Journal*, 139:1217–1238.

Tully, R. B. and Fisher, J. R. (1977). Reprint of 1977A&A....54..661T. A new method of determining distance to galaxies. *Astronomy and Astrophysics*, 500:105–117.

Virtanen, P., Gommers, R., Oliphant, T. E., Haberland, M., Reddy, T., Cournapeau, D., Burovski, E., Peterson, P., Weckesser, W., Bright, J., van der Walt, S. J., Brett, M., Wilson, J., Millman, K. J., Mayorov, N., Nelson, A. R. J., Jones,

E., Kern, R., Larson, E., Carey, C. J., Polat, İ., Feng, Y., Moore, E. W., VanderPlas, J., Laxalde, D., Perktold, J., Cimrman, R., Henriksen, I., Quintero, E. A., Harris, C. R., Archibald, A. M., Ribeiro, A. H., Pedregosa, F., van Mulbregt, P., and SciPy 1. 0 Contributors (2020). SciPy 1.0: fundamental algorithms for scientific computing in Python. *Nature Methods*, 17:261–272.

Vogelsberger, M., Genel, S., Sijacki, D., Torrey, P., Springel, V., and Hernquist, L. (2013). A model for cosmological simulations of galaxy formation physics. *Monthly Notices of the Royal Astronomical Society*, 436(4):3031–3067.

Walter, F., Carilli, C., Decarli, R., Riechers, D., Aravena, M., Bauer, F. E., Bertoldi, F., Bolatto, A., Boogaard, L., Bouwens, R., Burgarella, D., Casey, C., Cooray, A., Cortes, P., Cox, P., Daddi, E., Darling, J., Emonts, B., Gonzalez Lopez, J., Hodge, J., Inami, H., Ivison, R., Kovetz, E., Le Fèvre, O., Magnelli, B., Marrone, D., Murphy, E., Narayanan, D., Novak, M., Oesch, P., Pavesi, R., Diaz Santos, T., Sargent, M., Scott, D., Scoville, N., Stacey, G., Wagg, J., van der Werf, P., Uzgil, B., Weiss, A., and Yun, M. (2019). The evolution of the cosmic molecular gas density. *Bulletin of the American Astronomical Society*, 51(3):442.

Weiß, A. e. a. (2013). ALMA Redshifts of Millimeter-selected Galaxies from the SPT Survey: The Redshift Distribution of Dusty Star-forming Galaxies. *Astrophysical Journal*, 767(1):88.

Williams, J. P., Blitz, L., and McKee, C. F. (2000). The Structure and Evolution of Molecular Clouds: from Clumps to Cores to the IMF. In Mannings, V., Boss, A. P., and Russell, S. S., editors, *Protostars and Planets IV*, page 97.

Williams, R. E., Blacker, B., Dickinson, M., Dixon, W. V. D., Ferguson, H. C., Fruchter, A. S., Giavalisco, M., Gilliland, R. L., Heyer, I., Katsanis, R., Levay, Z., Lucas, R. A., McElroy, D. B., Petro, L., Postman, M., Adorf, H.-M., and Hook, R. (1996). The Hubble Deep Field: Observations, Data Reduction, and Galaxy Photometry. *Astronomical Journal*, 112:1335.

Wilson, T. L., Rohlfs, K., and Hüttemeister, S. (2013). *Tools of Radio Astronomy*. Springer-Verlag.

Wise, J. H., Turk, M. J., Norman, M. L., and Abel, T. (2012). The Birth of a Galaxy: Primordial Metal Enrichment and Stellar Populations. *Astrophysical Journal*, 745(1):50.

Wright, T. (1750). *An Original Theory or New Hypothesis of the Universe*. H. Chapelle.

Yagoubov, P., Mroczkowski, T., Belitsky, V., Cuadrado-Calle, D., Cuttaia, F., Fuller, G. A., Gallego, J. D., Gonzalez, A., Kaneko, K., Mena, P., Molina, R., Nesti, R., Tapia, V., Villa, F., Beltrán, M., Cavaliere, F., Ceru, J., Chesmore, G. E., Coughlin, K., De Breuck, C., Fredrixon, M., George, D., Gibson, H., Golec, J., Josaitis, A., Kemper, F., Kotiranta, M., Lapkin, I., López-Fernández, I., Marconi, G., Mariotti, S., McGenn, W., McMahon, J., Murk, A., Pezzotta, F., Phillips, N., Reyes, N., Ricciardi, S., Sandri, M., Strandberg, M., Terenzi, L., Testi, L., Thomas, B., Uzawa, Y., Viganò, D., and Wadefalk, N. (2020). Wideband

67-116 GHz receiver development for ALMA Band 2. *Astronomy & Astrophysics*, 634:A46.

Zavala, J. A., Casey, C. M., Manning, S. M., Aravena, M., Bethermin, M., Caputi, K. I., Clements, D. L., Cunha, E. d., Drew, P., Finkelstein, S. L., Fujimoto, S., Hayward, C., Hodge, J., Kartaltepe, J. S., Knudsen, K., Koekemoer, A. M., Long, A. S., Magdis, G. E., Man, A. W. S., Popping, G., Sanders, D., Scoville, N., Sheth, K., Staguhn, J., Toft, S., Treister, E., Vieira, J. D., and Yun, M. S. (2021). The Evolution of the IR Luminosity Function and Dust-obscured Star Formation over the Past 13 Billion Years. *Astrophysical Journal*, 909(2):165.

A

Models for Gravitational Lensing

This appendix contains more information on the lens and source models obtained from the gravitational lensing simulations. It is divided into three sections, one for the complete line modelling (Section A.1), one for the fractional line modelling with free source parameters (Section A.2) and one where only the source positions are allowed to vary (Section A.3). All sections contain tables for the dirty image, `visilens` and residual RMS. To save space, triangle plots are only plotted for the full line samplings in section A.1.

A.1 Full Line Triangle Plots

Figure A.1 and A.2 shows the triangle plot for the total line CO(3-2) line emission of SPT0125-47 and SPT2134-50, respectively. The long list of parameters has made these plots hopelessly large to include on one page. They are here at all to illustrate the independence for each variable. Fitted values and errors are presented in associated tables.

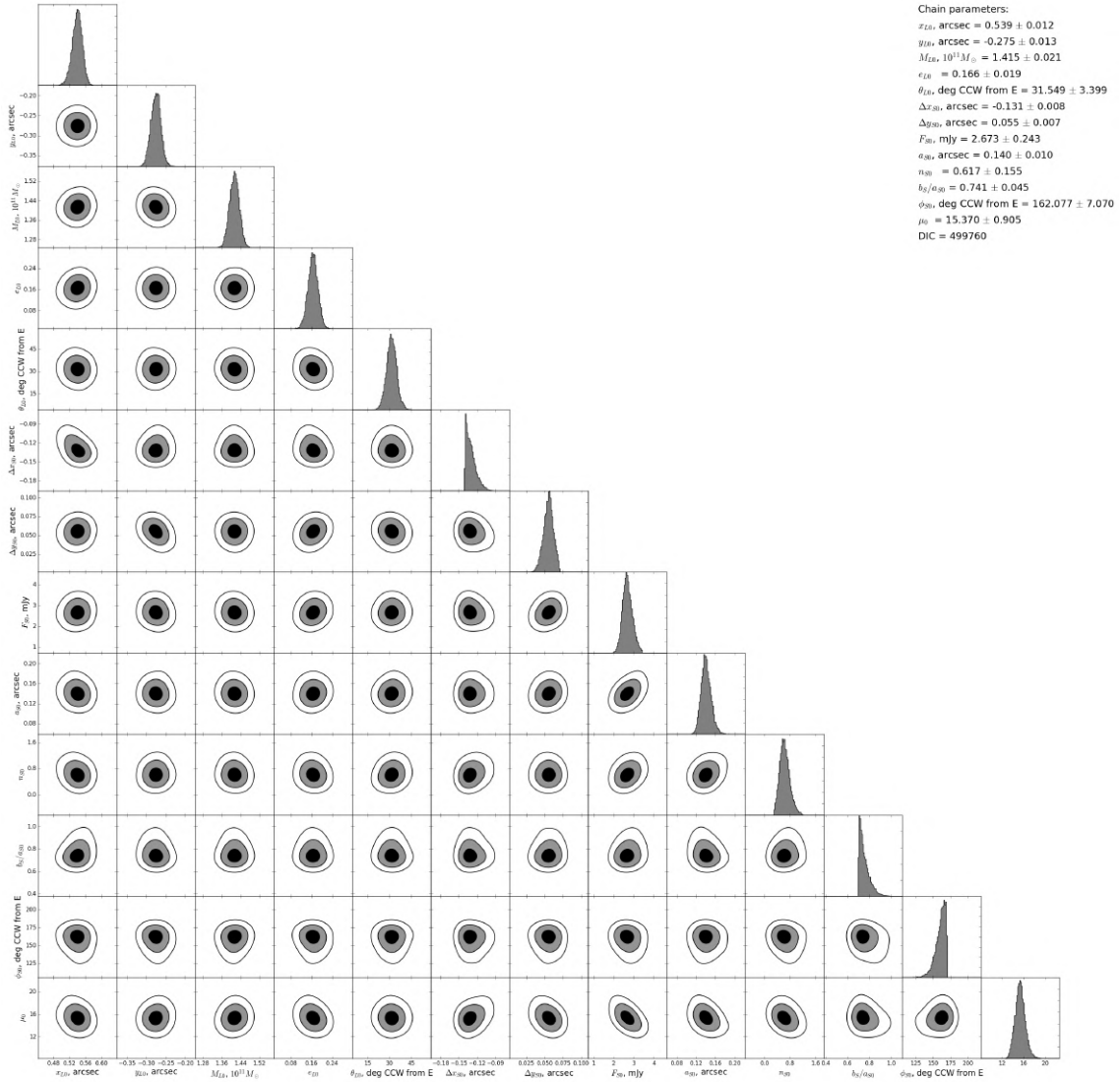

Figure A.1: Triangle plot for full line model of SPT0125-47.

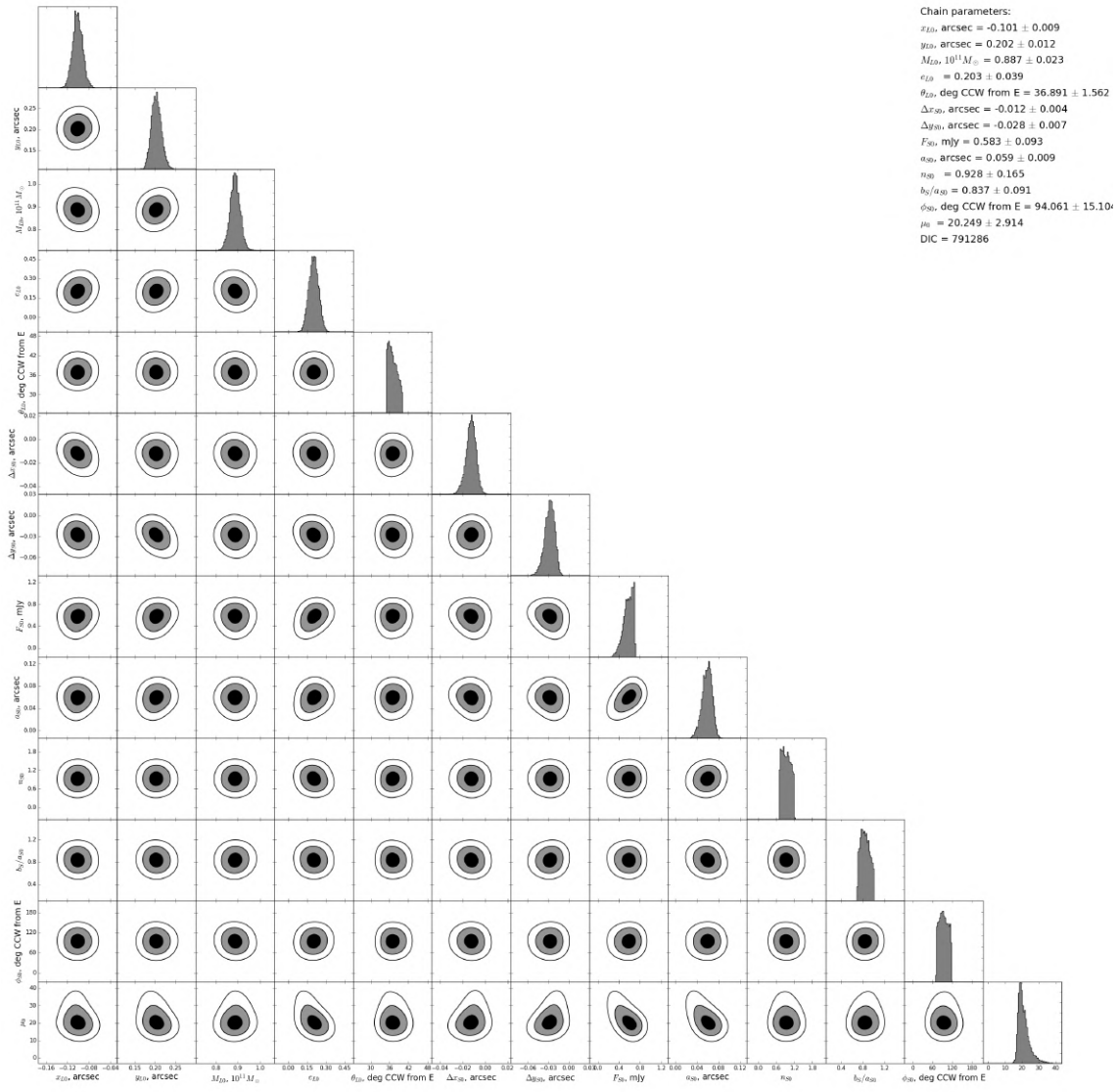

Figure A.2: Triangle plot for full line model of SPT2134-50.

Table A.1: RMS noise for Figure 5.5 and 5.6 in units of µJy.

Frequency bin	`visilens`	Dirty image	Residuals
98.28-98.42 GHz	197	223	202
98.42-98.48 GHz	297	305	299
98.30 GHz	355	370	366
98.34 GHz	354	376	364
98.38 GHz	357	389	365
98.42 GHz	357	395	360
98.46 GHz	359	360	361

Table A.2: RMS noise for Figure 5.7 and 5.8 in units of µJy.

Frequency bin	`visilens`	Dirty image	Residuals
91.34-91.54 GHz	140	150	142
91.54-91.64 GHz	189	187	190
91.37 GHz	244	248	243
91.43 GHz	247	236	243
91.49 GHz	244	263	248
91.55 GHz	243	254	239
91.61 GHz	238	234	241

A.2 Samplings with Free Source Parameters

The figure and tables in this section are created by running the algorithm with fixed lens parameters and free source parameters. Most of these results are presented in Chapter 5. Figure A.3 differs to Figure 5.6 only in that the first row has fixed lens positions. As is clear from its third column, the source emission is poorly reproduced in this bin. One reason for that could be that the lens is created with the effect of this particular frequency range. Notice also that the magnification for the 98.30 GHz bin is significantly higher than in Figure 5.6.

Table A.1 and A.2 presents the RMS noise for the simulations with free source parameters.

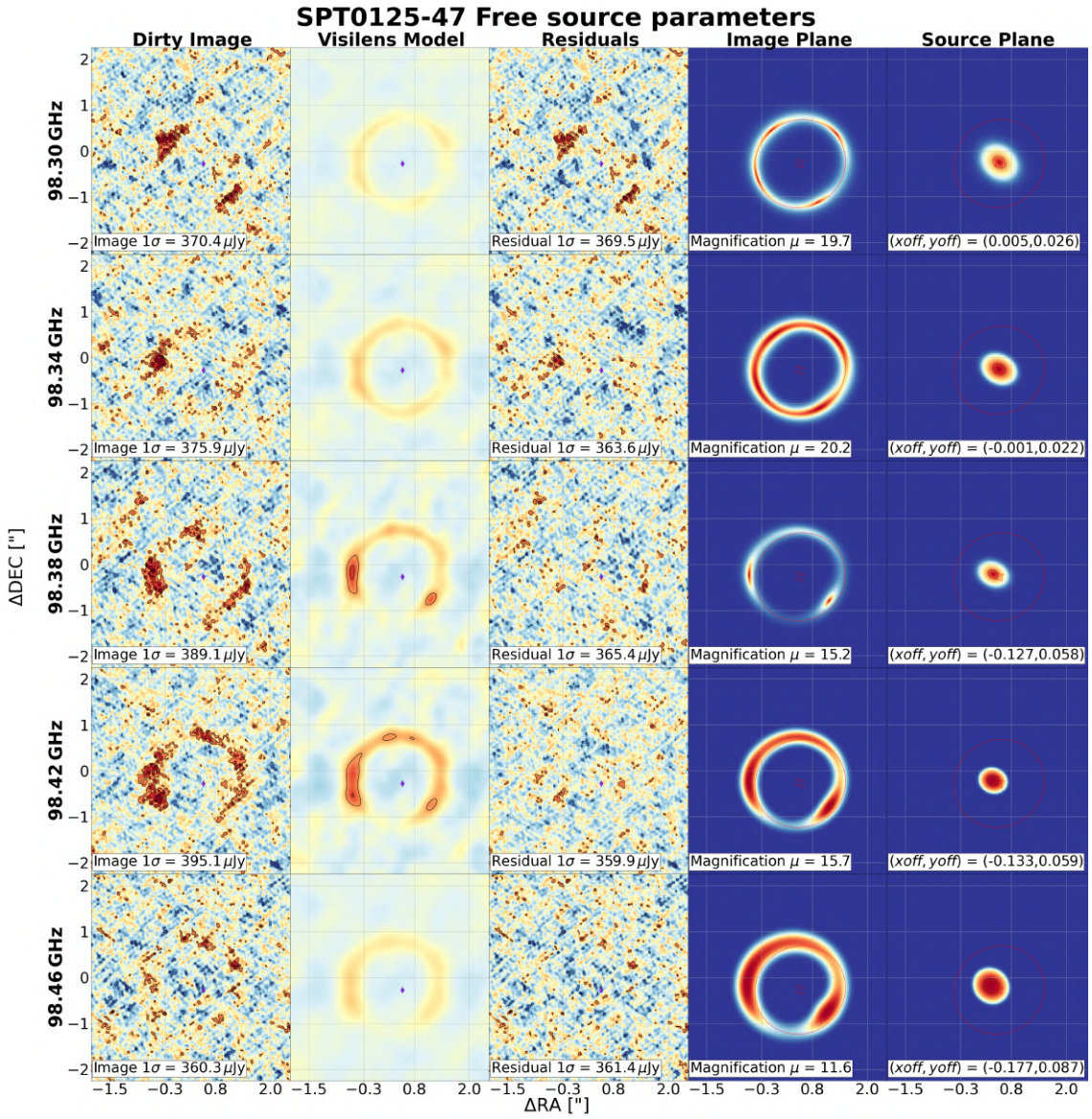

Figure A.3: Gravitational lensing models for five frequency bins where only the source parameters are allowed to vary. In contrast to Figure 5.6 the lens is fixed for the 98.30 GHz frequency bin. The dirty image, `visilens` and residual RMS for this new first row is 355 µJy, 370 µJy and 370 µJy, respectively.

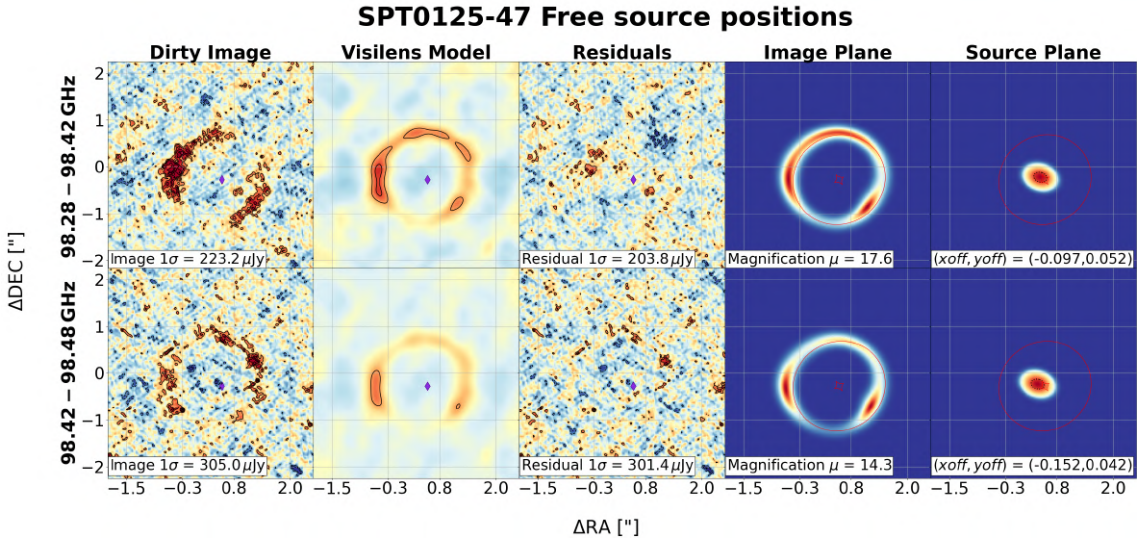

Figure A.4: Gravitational lensing models for two frequency bins where only the source positions are allowed to vary.

Table A.3: RMS noise for Figure A.4 in units of µJy.

Frequency bin	`visilens`	Dirty image	Residuals
98.28-98.42 GHz	197	223	204
98.42-98.48 GHz	297	305	301

A.3 Samplings with Free Source Position Samplings

In this section results of MCMC-samplings where only the source position and flux was allowed to vary.

Table A.4: RMS noise for Figure A.5 in units of µJy.

Frequency bin	`visilens`	Dirty image	Residuals
98.30 GHz	355	370	370
98.34 GHz	354	376	363
98.38 GHz	357	389	366
98.42 GHz	357	395	360
98.46 GHz	359	360	363

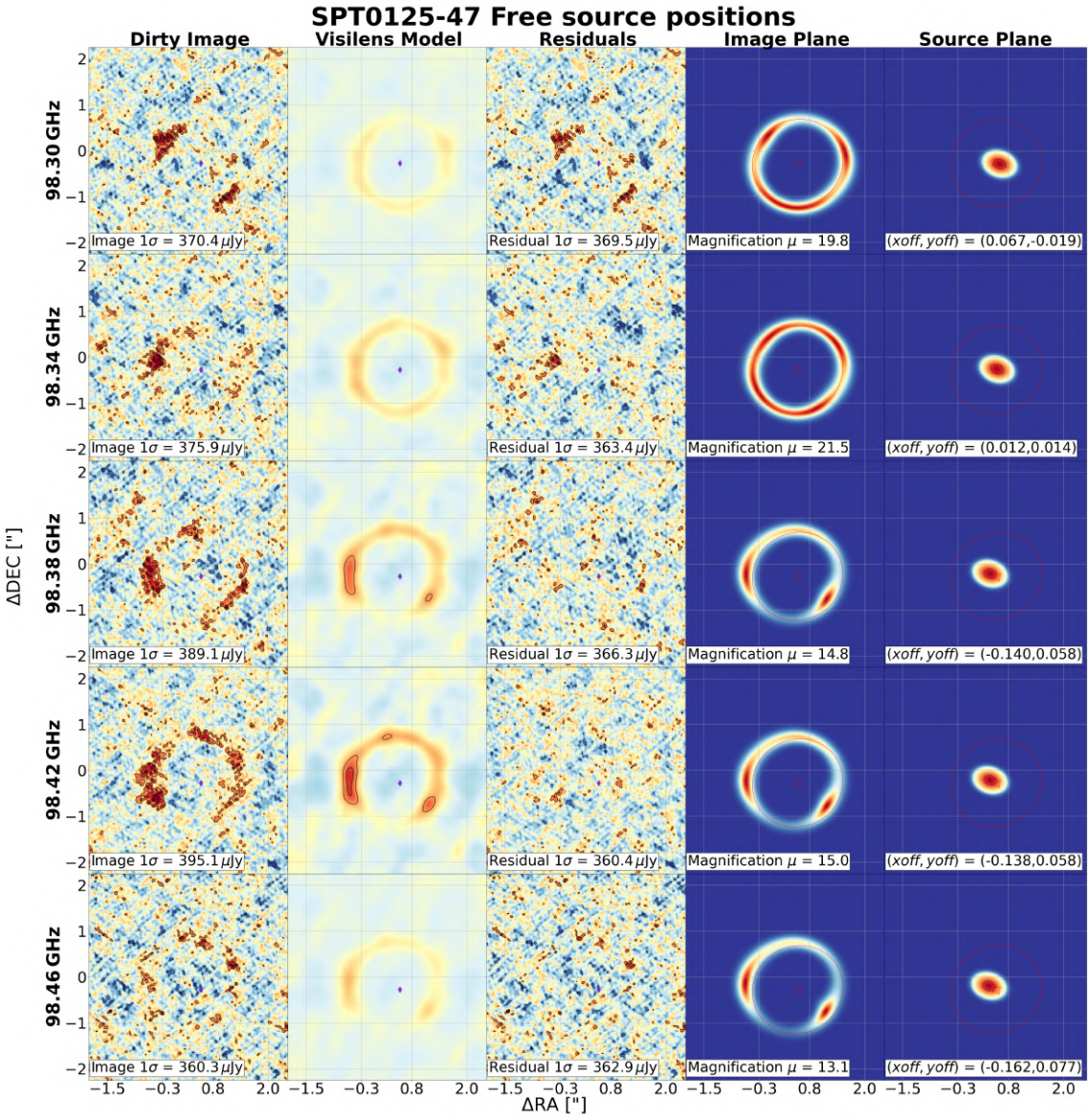

Figure A.5: Gravitational lensing models for five frequency bins where only the source positions are allowed to vary.

Table A.5: RMS noise for Figure A.6 in units of µJy.

Frequency bin	`visilens`	Dirty image	Residuals
91.34-91.54 GHz	140	150	142
91.54-91.64 GHz	189	187	189

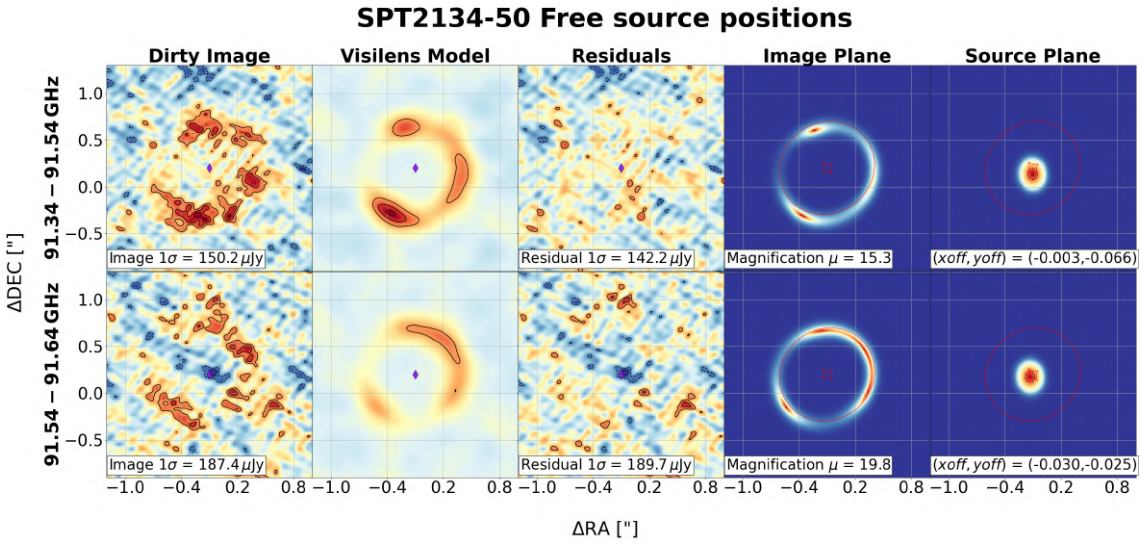

Figure A.6: Gravitational lensing models for two frequency bins where only the source positions are allowed to vary.

Table A.6: RMS noise for Figure A.7 in units of µJy.

Frequency bin	`visilens`	Dirty image	Residuals
91.37 GHz	244	248	243
91.43 GHz	247	236	243
91.49 GHz	244	263	249
91.55 GHz	243	254	239
91.61 GHz	238	234	240

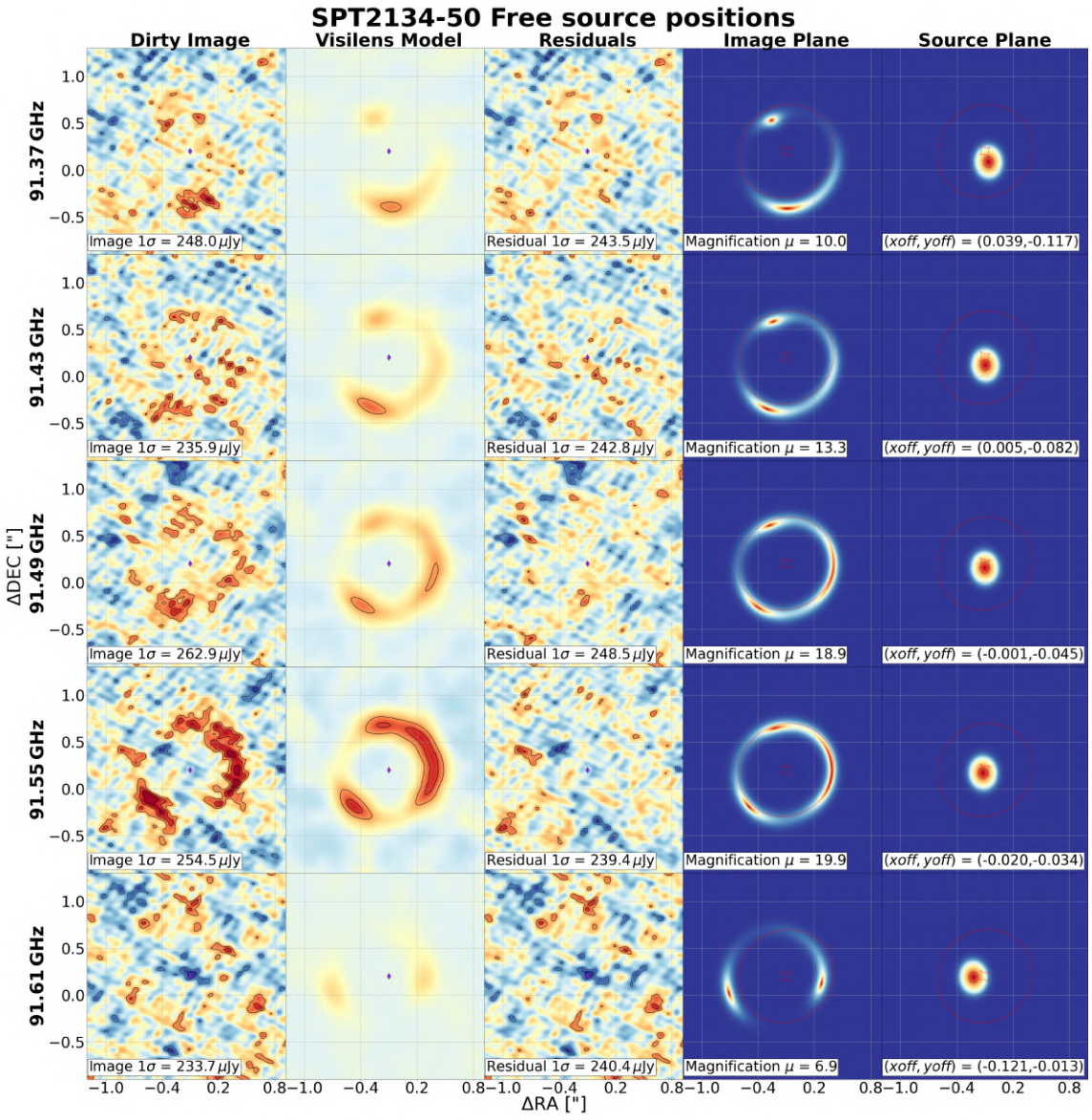

Figure A.7: Gravitational lensing models for five frequency bins where only the source positions are allowed to vary.

B

Coordinate Systems

Astronomical coordinate systems are important both for finding a source and for calculating its relative speed. In the often used equatorial coordinates, which are illustrated in Figure B.1, astronomical sources are viewed as positioned on a large sphere. The celestial north pole is directly above Earth's north pole. Due to the tilt of Earth's axis of rotation, the celestial equator intersects with the ecliptic at $23.5\,^{\circ}$. Equatorial coordinates include the declination δ as the angle above the celestial equator, and the right ascension α as the eastward angle from the point of intersection of the celestial and the plane of orbital motion, called ecliptic, at vernal equinox (Sparke and Gallagher, 2007, section 1.2.2). Right ascension is usually measured in sidereal hours, or one 24th of 360°, minutes and seconds, which are one 60th of the previous. Declination uses degrees followed by minutes, and seconds (see eg. (Cox, 2000)).

Equatorial coordinates change with time due to the motion of the sources and precession: Earth's elliptical orbit rotates with a period of 25 770 years[1]. Astronomical coordinates therefore include a reference epoch. The J2000 epoch uses the celestial coordinates of 12 noon at January the 1st, year 2000. The 'J' refers to the Julian calendar, i.e. 365.25 days per year. When specifying positions of astronomical sources the epoch need not be the same as the equinox. The latter is merely the precessed coordinates. For these, other factors, e.g. nutation, are not accounted for.[2]

Alternatively, extended objects and binaries can be characterised with the position angle (PA) and separation (SEP). For a system of two binary stars, an 'effective north' is introduced as the direction between the reference star and the north celestial pole (see the dotted line between the star and the north celestial pole in Figure B.1). Then, east, west and south are similarly 'elevated' from the surface of Earth to the celestial sphere. Now, the projection angle is the angle between the stars, starting moving to the east. The separation is simply the angular distance between the binaries. For galaxies and other extended objects, the centre of the object serves as the reference and the PA becomes the angle between this new 'effective north' and the major axis of the object.

The *International Astronomical Union* (IAU) has decided on an International Celestial Reference System (ICRS), which is about a hundred milliarcsecond off from the J2000 equatorial coordinate system. A reference system becomes a reference frame when it is used to calculate actual numbers. When measuring with antennas,

[1] `https://quantumredpill.wordpress.com/2013/01/16/equatorial-coordinate-system/`.
[2] `https://cosmicreflections.skythisweek.info/2017/01/19/epoch-and-equinox/`.

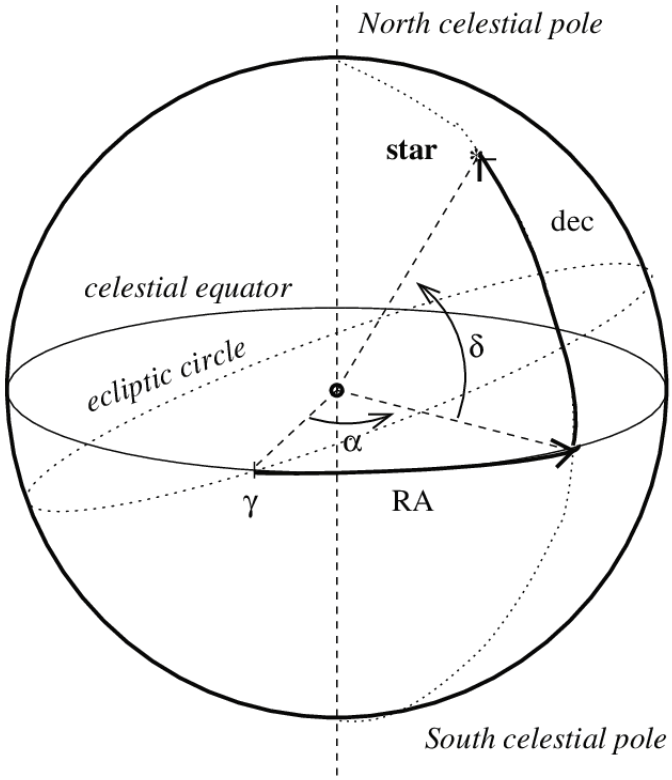

Figure B.1: The equatorial coordinate system. Credit: (Patris, 2010, figure 1).

the topocentric reference frame, i.e. the set of East, North and up for the observer, is usually converted to a frame of Local Standard of Rest (LSR). This velocity frame accounts for the 255 km/s orbital motion of the Sun around the galactic center as well as its 16.5 km/s peculiar motion. There is an inconvenient multitude of additional coordinate systems and frames, including the bary- and heliocentric standard of rest that do not account for the peculiar motion of the sun,[3] but none of them will be used in this thesis.

[3] `https://public.nrao.edu/ask/velocity-reference-used-in-radio-astronomy/`.

DEPARTMENT OF SOME SUBJECT OR TECHNOLOGY
CHALMERS UNIVERSITY OF TECHNOLOGY
Gothenburg, Sweden
www.chalmers.se

CHALMERS
UNIVERSITY OF TECHNOLOGY